Accurate and efficient orbit prediction through improved drag force modelling of GRACE and PROBA-V satellites.

Pugazhenthi Sivasankar - 4414764

TU Delft

Accurate and efficient orbit prediction through improved drag force modelling of GRACE and PROBA-V satellites.

AE5810 - Final Thesis
(Cover image: PROBA-V (Source: Qinetiq Space))

Pugazhenthi Sivasankar - 4414764

Supervisors:
Dr. E.N. (Eelco) Doornbos, KNMI
Dr. J.A.A. (Jose) van den Ijssel, TUDelft
Dr. Joris Naudet, Qinetiq Space

Thesis committee:
Prof. dr. P.N.A.M. (Pieter) Visser, TUDelft
Dr. J.A.A. (Jose) van den Ijssel, TUDelft
Dr. Joris Naudet, Qinetiq Space
Dr. B.V.S. Jyoti, TUDelft

A thesis presented for the degree of
M.Sc. Spaceflight
Public defence: September 26, 2019 from 13:30 to 14:30 hrs

Astrodynamics & Space Missions
Delft University of Technology
The Netherlands

Electronic version at: `https://repository.tudelft.nl/`

Preface

This is a thesis report submitted in partial fulfillment of M.Sc.Space Exploration, TUDelft. It describes the outcomes of the work conducted by the author in Qinetiq Space, Belgium and TUDelft towards improving the orbit prediction of SAOCOM-CS satellite based on the navigation data from GRACE and PROBA-V satellite missions. PROBA-V was selected due to the prior internship experience of the author in Qinetiq Space with its navigation data and GRACE was selected due to the availability of highly precise ephemeris. This report is targeted towards executives and specialists who work in the field of LEO satellite orbit predictions. This report assumes knowledge of astrodynamics of two-body systems and orbit determination process on the part of the reader. Readers who are particularly interested in the computational efficiency can find it in Chapter 6. The author would like to express his gratitude to Qinetiq Space for sponsoring this project and to Dr. Dominic Dirkx for providing software assistance regarding TUDAT throughout the project.

Abstract

In recent years, with the increasing number of man made objects in space the need for accurate satellite orbit prediction has increased tremendously. Prediction of satellite trajectories is important to plan collision avoidance manoeuvres between space assets and debris, to autonomously maintain formation flying missions and to plan manoeuvres for ground-track maintenance of Earth-observation missions. For satellites in very low LEO, aerodynamic drag is the largest and the most difficult force to model because of the changing nature of atmospheric density. This report describes the efforts made towards improving the orbit prediction of SAOCOM-CS with a focus on drag force modelling. This is accomplished by orbit determination using GPS state vector measurements and precise deterministic force models, during periods of high and low solar activity. Drag scale factors are estimated with different resolutions. Different methods are used to choose the estimated drag scale factors for orbit prediction. GRACE-A and PROBA-V satellites are used as test cases. For a prediction arc length of one day, the best prediction strategy results in maximum position errors (3D) of 243.5 m and 24.1 m for GRACE-A & PROBA-V, respectively during high solar activity. Based on the prediction results of GRACE-A & PROBA-V, a rule of thumb analysis is used to derive the maximum position error in the orbit prediction of SAOCOM-CS, which lies between 40 and 75 m. Changes in the mean estimated drag scale factors of the satellites are observed between high and low solar activity which might indicate deficiencies in the NRLMSISE-00 density model. The report also provides the effect of the space weather forecast errors on the best prediction strategy. Introducing a 10 % error in the solar activity index resulted in mean maximum along-track prediction errors of 393 m and 16 m for GRACE-A & PROBA-V, respectively during high solar activity. Similarly, including random errors in the geomagnetic activity index resulted in mean maximum along-track prediction errors of 443 m and 15 m for GRACE-A & PROBA-V, respectively during high solar activity. Finally, the optimization of the estimation and prediction methods for the computational efficiency of PROBA-V is presented. A six hour estimation arc length with the force model comprising Earth gravity field of degree and order 30 of the model ITU_GRACE 16 with luni-solar perturbations and devoid of atmospheric drag, solar radiation pressure and tidal forces is the most computationally efficient combination for a prediction arc length of one day.

Contents

Chapter 1

Introduction

Ever since the launch of Sputnik 1 into the very low Low-Earth Orbit (LEO) in 1957, the number, size and complexity of Earth orbiting satellites have increased tremendously. Earth observation missions, both civil and military, make extensive use of the very low LEO region where the International Space Station (ISS) also operates with its crew. The region of space between the altitudes of 200 - 1500 km is getting crowded faster with the advent of cost effective and easy to launch micro and nano satellites.

With the increase in space assets (satellites, ISS), the problem of in-orbit collision escalates. Collisions can occur between the space assets and space debris (defunct satellites and upper stages of launch vehicles) and among the assets and debris themselves. For example, the hypervelocity collision in February 2009 between the satellites Iridium 33 and Kosmos-2251 [Pastel, 2011] at 789 km altitude resulted in approximately 1000 pieces of debris larger than 10 cm. This can lead to a cascade of debris generation which further increases the risk of collision. To prevent such events from happening, it is essential to predict the orbits of satellites in the very low LEO (till 800 km altitude) region with a reasonable degree of accuracy. This is the focus of this thesis work.

This introductory chapter provides recent advances in orbit prediction capabilities for LEO satellites in Section 1.1. This is followed by the relevant background information on the satellites considered and the motivation for this thesis work in Section 1.2 which leads to the formulation of the research objectives in Section 1.3. The chapter concludes with an outline for the rest of the report in Section 1.4.

1.1 Satellite orbit prediction in LEO

Newton's laws of gravitation and equations of motion were used in earlier days to predict the orbit of a satellite. This resulted in a deterministic approach. Modern methods in digital computing and satellite tracking enabled a stochastic approach to orbit determination and prediction of satellites. Compared to satellites in the Medium Earth Orbit (MEO) and the Geostationary Earth Orbit (GEO), satellites in the LEO experience greater perturbing forces resulting in larger deviations from the standard Kepler orbit. These perturbations are due to higher order spherical harmonics in Earth's gravitational field, tidal forces and non-gravitational forces. Geodetic missions such as GRACE, GOCE and CHAMP contributed to the precise modelling of Earth's gravitational field.

Among the non-gravitational forces, solar radiation pressure and atmospheric drag predominantly affect the evolution of a satellite's orbit in the very low LEO. Compared to drag force, the effect of solar radiation pressure on a satellite's orbit in the very low LEO is of low magnitude and has been modelled to a reasonable degree of accuracy. The drag force, however, is highly variable and difficult to predict. Hence, improvement in drag force modelling enhances the orbit prediction accuracy for satellites in the very low LEO.

Earlier researchers [Jacchia and Slowey, 1963, Jacchia, 1970] worked on establishing and developing empirical models of the upper atmosphere from which density values were used in the orbit computations of satellites. However, there were limitations such as inaccurate modelling of the drag coefficient (C_d) of satellites and ignorance of long-term trends in thermosphere [Doornbos, 2012]. In general, for a reliable satellite orbit prediction, there are also other challenges besides accurate modelling of thermosphere density. These include challenges in numerical computing and establishing realistic uncertainties in the measurement and force models [Vallado, 2001].

Considering the collision avoidance between space assets and space debris, many satellite operators have to screen their assets against all other space objects. Prediction assessments based on Two-Line Elements (TLE) of these objects using the associated analytic propagator (SGP4) are not very suitable to execute potential collision avoidance manoeuvres. These assessments result in an unacceptably large number of potential collisions per space object, each with a very low probability. This problem was addressed by Levit and Marshall [2011] in which a high precision numerical propagator and batch least-squares differential correction were applied to fit an orbit to the state vectors derived from successive TLEs. The orbit fit was then propagated forward in time and the propagated (i.e.predicted) orbit was validated against the precision ephemeris data derived from the International Laser Ranging Service (ILRS) for several satellites. This method led to a 10-fold improvement compared to propagating individual TLEs using the SGP4 propagator.

From the space industry point of view, improved orbit prediction can help in determining the fuel required for orbit maintenance and manoeuvring for formation flying missions in the very low LEO. Drag force causes overall formation decay and if left uncompensated for long-term missions can result in premature re-entry. Besides, drag force can affect each satellite in the formation differently such that small perturbations can lead to large separations over the course of many orbits. This requires both in-track and cross-track stationkeeping. Elaborate discussion on these techniques is provided in Wertz [2001].

1.2 SAOCOM-CS, PROBA-V & GRACE-A missions

The driving requirement for this thesis work comes from the planned SAOCOM-CS (SAtellites for Observations and COMmunications-Companion Satellite) mission. Since the data required for the orbit prediction of SAOCOM-CS is not available, GRACE and PROBA-V satellites are chosen for the thesis work. PROBA-V is chosen due to the availability of GPS (Global Positioning System) state vector data from Qinetiq Space. The GRACE satellite is chosen to be used as a reference for a more precise assessment of the software algorithms of this thesis work. This is due to the highly accurate navigation data

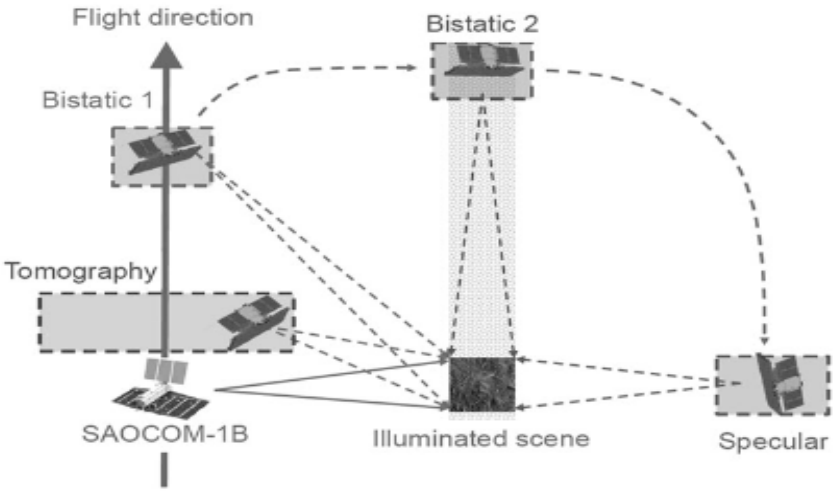

Figure 1.1: Mission observation geometry of SAOCOM-CS and SAOCOM-1B [Montenbruck et al., 2018]

of GRACE. Hence, using two different satellites with one below and the other above the altitude of the planned SAOCOM-CS mission, this thesis also studies the behaviour of thermosphere at two different regions. The relevant parameters of the satellites are summarized in the Table 1.1.

1.2.1 SAOCOM-CS

SAOCOM-CS was a planned receive-only companion satellite mission which was proposed to formation fly with SAOCOM-1B, the master satellite. The SAOCOM-1B is an L-band polarimetric SAR satellite with a mass of roughly 3 tons and is expected to be launched into a frozen Sun-synchronous, dawn-dusk orbit with an inclination of 97.88° and a reference altitude of 619.60 km in early 2020. The main mission of SAOCOM-1B is hydrology and land observation with substantial contribution to surveillance and emergency management [Montenbruck et al., 2018]. The planned objective of the SAOCOM-CS mission was to use a low-cost receive-only companion SAR (Synthetic Aperture Radar) on a separate platform in tandem with active SAR master satellite. With this set up, the surface heights and displacements across a wide variety of terrestrial environments could be accurately measured using cross-track and along-track interferometry [Davidson et al., 2014]. A schematic of the mission observation geometry is given in the Figure 1.1. This data was supposed to be used for agriculture, forestry and hydrology. ESA (European Space Agency) was responsible for SAOCOM-CS and CONAE (Comisin Nacional de Actividades Espaciales), the space agency of Argentina is responsible for SAOCOM-1B. Qinetiq Space was the company in charge of the satellite bus of SAOCOM-CS as well as its onboard navigation operations. The reference orbit of SAOCOM-CS was planned to be the same as that of SAOCOM-1B. However, SAOCOM-CS was cancelled during the thesis due to political decisions (Personal communication: Dr. Joris Naudet). A perspective of SAOCOM-CS is shown in the Figure 1.7a.

The receiver chosen for the navigation of SAOCOM-CS was PODRIX, the RUAG Space dual-frequency GNSS (Global Navigation Satellite Systems) Precise Orbit Deter-

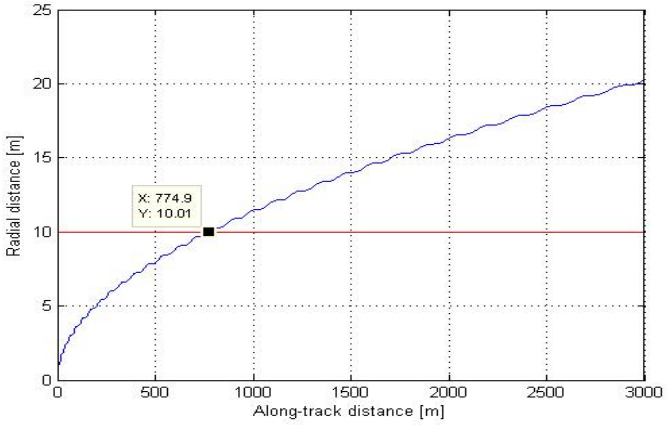

Figure 1.2: Radial distance as a function of the along-track distance (Source: Qinetiq Space).

mination receiver. It would use signals from both GPS and Galileo systems to provide on-board real-time navigation solution accuracy of below one meter. The following would be some of its main features [Montenbruck et al., 2018]:

- Navigation solution accuracy (3D RMS) for position would be 1 m and for velocity would be 2 mm/s.
- Advanced Kalman filtering would enable high on-board navigation performance.

SAOCOM-CS was estimated to have a dry mass of 377 kg and a propellant mass of 23 kg to maintain the SAOCOM-CS and SAOCOM-1B configuration. The maximum reference area for aerodynamic drag would be 3.7700 m^2 and the drag scale factor/drag coefficient (C_d) would be 2.20 (Personal communication: Dr. Joris Naudet, Qinetiq Space).

The following paragraphs deal with the along-track maintenance of SAOCOM configuration which would be essential to accomplish the main objective of the mission. SAOCOM-CS, the leading satellite would experience a higher drag than SAOCOM-1B, due to the difference in ballistic coefficients. This would decrease the altitude, causing a forward shift with respect to SAOCOM-1B, thereby breaking the formation. Assuming the same initial orbital elements for both satellites and atmospheric drag as the only perturbing force, a preliminary analysis was performed by Qinetiq Space to study the effect of drag on the difference in semi-major axis (radial distance) and the along-track distance between the two satellites. From Figure 1.2 it can be seen that for a radial distance (altitude difference) of 10 m, the along-track distance, which shows a quadratic variation, reaches a value of 775 m. When the along-track distance between the two satellites is too high, it would result in low quality payload operations and when the along-track distance is too low, it would pose a risk of collision of the two satellites. Hence, correction manoeuvres should be performed when the maximum and minimum allowable along-track distance are reached. The difference between the maximum and minimum along-track distance would be called as the **along-track deadband**. Since SAOCOM-CS would move up and down with respect to SAOCOM-1B, the difference between the maximum and minimum radial distance between the two satellites would be called as the **altitude deadband**.

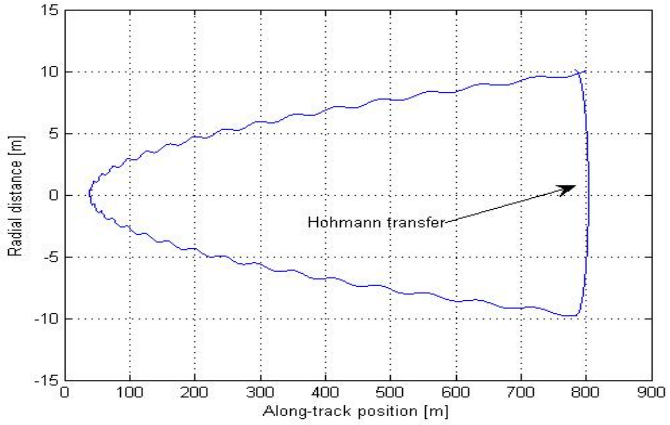

Figure 1.3: Resulting D-pattern from the differential drag correction manoeuvres of SAOCOM-CS (Source: Qinetiq Space).

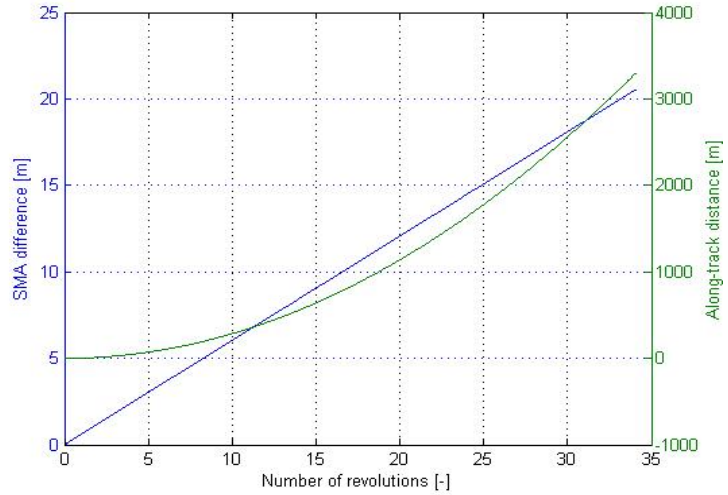

Figure 1.4: Difference in semi-major axis and along-track distance as a function of the number of orbits (Source: Qinetiq Space).

The goal of the differential drag compensation manoeuvre would be to raise the orbit of SAOCOM-CS to an altitude above SAOCOM-1B to cause a backward shift with respect to SAOCOM-1B. The strategy would be to use a single Hohmann transfer to raise the altitude of SAOCOM-CS by a magnitude equal to twice the altitude deadband. Figure 1.3 shows the effect of such a Hohmann manoeuvre on the along-track and radial distance. Figure 1.4 shows that a semi-major axis (SMA) decrease of 20 m is obtained after approximately 33 orbits or 2.24 days. This determines the frequency of the manoeuvres.

The analysis by Qinetiq Space used an atmospheric density of $5 * 10^{-13}$ kg/m^3, which resulted in conservative values for the orbit maintenance manoeuvers. Figure 1.5 shows the effect of changing the density on the evolution of radial distance with along-track distance and number of orbit revolutions. For an along-track deadband of 800 m, it can be seen that the higher the density, the larger is the radial distance and lesser is the number of revolutions for a given radial distance. This would require frequent large altitude raise manoeuvres. On the other hand, lower and more realistic density values would drive the resolution of the on-board propulsion subsystem. ESA set the maximum

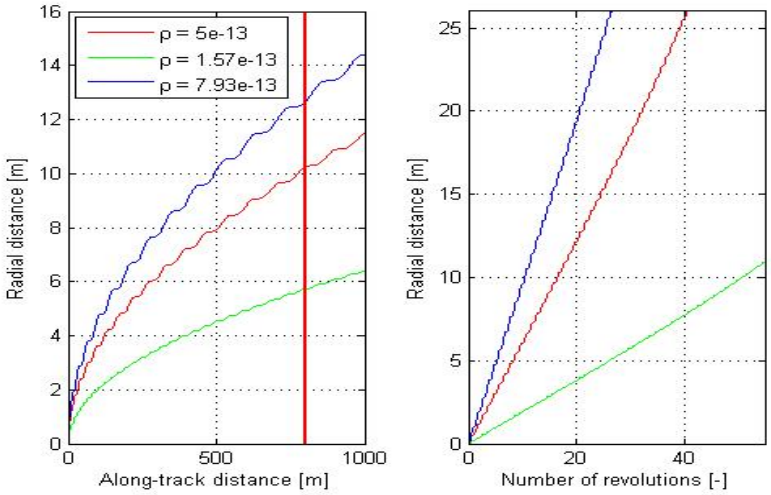

Figure 1.5: Effect of changing density on the radial distance (Source: Qinetiq Space).

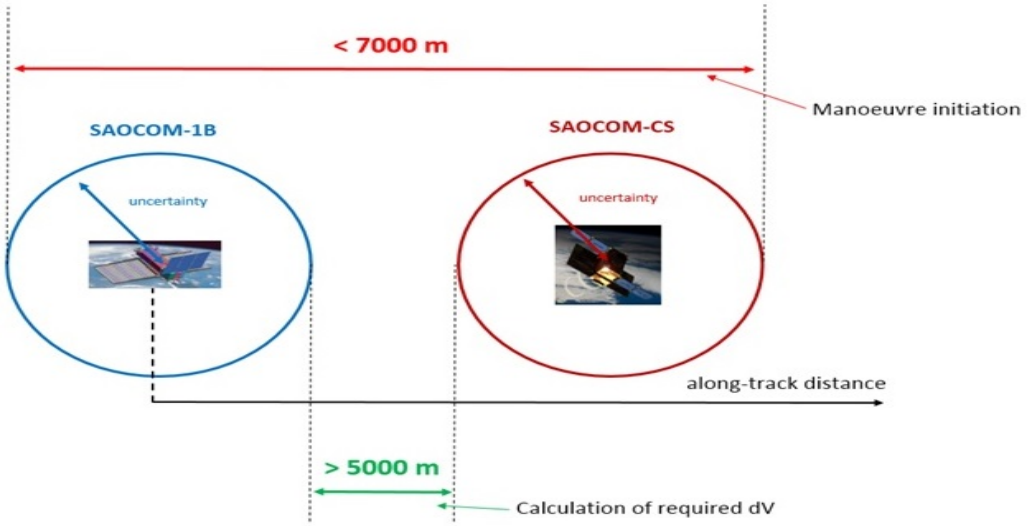

Figure 1.6: Along-track control of SAOCOM configuration (Source: Qinetiq Space).

along-track distance to 7 km and the minimum along-track distance to 5 km, thereby making the along-track deadband as 2 km. This is depicted in Figure 1.6.

A preliminary orbit propagation of SAOCOM-CS was performed in Qinetiq Space using Monte-Carlo method to know when the along-track limit would be reached (Personal communication: Dr. Joris Naudet, Qinetiq Space). A few hundred simulations were done with different errors on ballistic coefficient, atmospheric density, initial state vector knowledge and thruster performance. They resulted in the requirement that **the norm of the maximum position error in the orbit propagation of SAOCOM-CS should be less than** 125 **m after one day of propagation** (Personal communication: Dr. Joris Naudet, Qinetiq Space). This would optimize the frequency of propulsive manoeuvres and minimize the operational load in terms of telecommand on both partners (Qinetiq Space and CONAE). The plan is to meet this requirement using the GPS state vector data of SAOCOM-CS. This requirement serves as a motivation for the orbit estimation and prediction schemes of this thesis work described in Chapter 2.

1.2.2 PROBA-V

PROBA-V (PRoject for On-Board Autonomy - Vegetation) is a mission to observe the vegetation of the Earth. ESA launched the satellite into space on May 7, 2013 using a Vega launcher into a Sun-synchronous orbit of 820 km altitude and 98.80° inclination. The orbit insertion was done under special conditions so as to allow the imaging of vegetation under sufficient illumination for most of the mission lifetime [Francois et al., 2014]. A perspective of PROBA-V is shown in Figure 1.7b

The satellite has a set of redundant Phoenix GPS receivers manufactured by the DLR (Deutsches Zentrum fr Luft- und Raumfahrt). This single frequency GPS receiver is suitable for satellites with limited on board resources. The receiver has an attitude interface to account for non-zenith pointing antennas in the channel allocation process, optimized tracking loops for high accuracy code and carrier tracking, and precision timing and integer ambiguities for carrier phase based relative navigation [Gantois et al., 2006]. The following are some of its specifications [Montenbruck et al., 2004]:

- Position accuracy of the single-point solution: 10 m.
- Velocity accuracy of the single-point solution: 0.1 m/s.
- Accuracy of the filtered solution: $1 - 2$ m.

The raw GPS observations of PROBA-V are not available for the thesis work due to the limitations in telemetry. Instead the GPS state vector data from on-board navigation is used. Further details on the GPS state vector data obtained from PROBA-V are provided in Section 2.1. The PROBA-V spacecraft has a mass of 138 kg with a volume of 80 cm by 80 cm by 100 cm. The shape of the satellite can be approximated by a square cuboid with 6 panels. Besides, the spacecraft has a three-axis stabilized platform [Vrancken et al., 2012] which results in a maximum cross sectional area of 1.1314 m^2 in the along-track direction. There is no necessity for orbit correction manoeuvres on PROBA-V and hence it does not carry a propulsion system on-board (Personal communication: Dr. Joris Naudet, Qinetiq Space).

1.2.3 GRACE-A

GRACE (Gravity Recovery And Climate Experiment) was a mission to map the global gravity field with a spatial resolution of 400 km to 40,000 km every thirty days. It was a joint project between NASA (National Aeronautics and Space Administration), DLR and GFZ (Geo Forschungs Zentrum)-Potsdam. The mission had two identical satellites linked by a highly accurate inter-satellite K-Band microwave ranging system [Tapley et al., 2004b]. The inter-satellite KBR system accurately measured the variation of the along-track separation between the two GRACE satellites, which indicated the temporal and spatial variations in the gravity field of the Earth. Both satellites were launched on an Eurockot vehicle on March 17, 2002 (dual-launch) into a circular polar co-planar orbit that had an initial altitude of 485 km at launch and an inclination of 89°. During the course of the mission, the two tandem satellites were separated by in-orbit distances ranging between 170 to 270 km. The external geometry of one of the satellites is shown in Figure 1.7c.

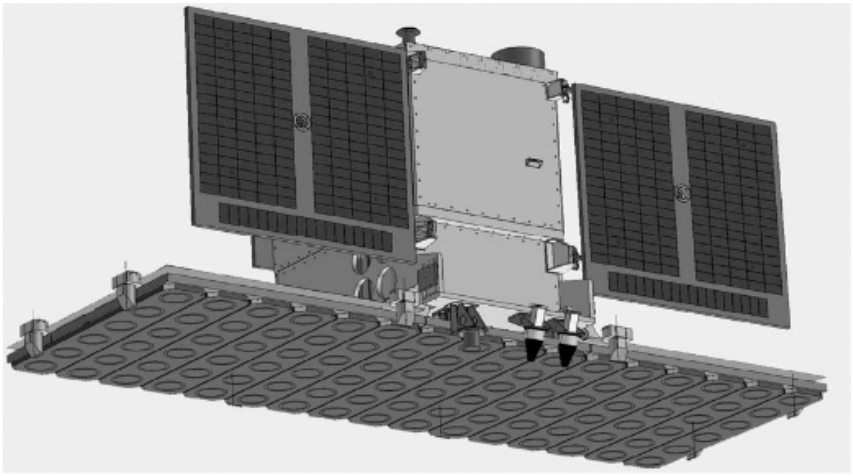

(a) SAOCOM-CS (Source: Qinetiq Space)

(b) Proba-V in orbit (Source: Qinetiq Space).

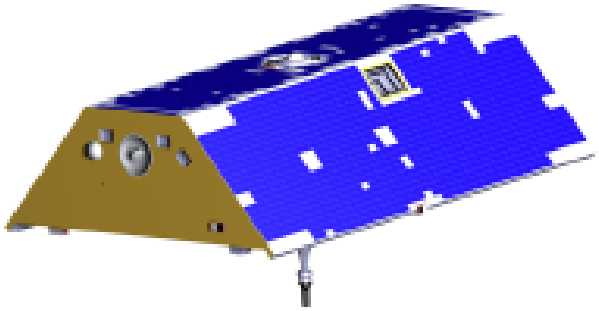

(c) Satellite geometry of GRACE-A [March et al., 2019].

Figure 1.7: Satellites considered for this thesis work

Satellite name	Orbit type	Initial orbit altitude (km)	Initial Orbit inclination (degrees)	Wet mass (kg)	Frontal area (m^2)
SAOCOM-CS	Frozen, sun-synchronous and dawn-dusk	619.60	97.88	400.00	3.7700
GRACE	Polar circular	485.00	89.00	487.20	1.0013
PROBA-V	Polar, sun-synchronous and circular	820.00	98.80	138.00	1.1314

Table 1.1: Summary of the relevant parameters of satellites considered for this thesis work.(Sources: Sections 1.2.1, 1.2.2 and 1.2.3.)

GRACE satellites made use of the BlackJack, a dual frequency GPS receiver developed by the NASA's Jet Propulsion Laboratory (JPL). It enabled precise time-tagging of the measurements used in extracting the inter-satellite range change and provided absolute positions of the satellites over the Earth. The following were some of its specifications [Montenbruck and Kroes, 2003]:

- a 48-channel receiver with a capability of tracking 16 GPS satellites on one antenna, with navigation, timing, and precise orbit determination capabilities,
- Noise in the computed position in telemetry (navigation solution) was less than 60 m,
- The observation noise in phase (ionosphere-free) was less than 0.2 cm and the observation noise in range (ionosphere-free) was less than 30 cm.

Though raw GPS observations are available for GRACE satellites, this thesis work only uses the GPS state vector data. Further details on the GPS state vector data obtained from GRACE are provided in Section 2.1. Each GRACE satellite had a wet mass of 487.20 kg and can be approximated by a 9 panel model. The exterior dimensions of the macro model and the properties of the surfaces can be found in product specification document of GRACE [Bettadpur, 2012], which also gives a maximum cross sectional area of 1.0013 m^2 in the along-track direction. During the GRACE mission, manoeuvring was done for orbit acquisition, formation keeping, attitude correction for relative pointing and switching the position of the satellites [Herman, 2012]. It was a requirement that the two GRACE satellites must be aligned with an accuracy of 0.5 mrad. To meet this requirement manoeuvres were performed from time to time. The equations of these manoeuvres can be found in Kirschner et al. [2001]. For this thesis work, only the manoeuvre-free days were selected for data processing, the details of which are provided in Section 2.5.

1.3 Research questions and research objective

It is clear from the analysis presented in Section 1.2.1 that it is required to predict the time when the along-track limit of the SAOCOM configuration will be reached and the magnitude of altitude increase that will be required. Since this deals with the time before the execution of the orbit maintenance manoeuvre, the scope of the thesis work is limited

to processing the navigation data of satellites which does not include the manoeuvring periods. It should be noted that there are constraints on navigation data such as the non-availability of raw GPS observations for PROBA-V satellite. After a comprehensive literature review, the following main research question is formulated to guide the thesis work:

How to develop an orbit prediction algorithm for SAOCOM-CS satellite that can result in a reliable orbit prediction for one day with a maximum position error norm of 125 *m?*

This can be divided into the following sub-questions:

1. What are the relevant factors to be considered to improve the drag force modelling for better orbit prediction?
2. How to adapt the prediction schemes for different drag conditions, which are assessed by using satellites at different altitudes and during different solar activity conditions?
3. How to optimize the estimation and prediction procedures for computational efficiency?

Besides these sub-questions the following is another relevant question for this thesis work: Can the results of the orbit estimation and prediction be used to assess the atmosphere model? Thus, the main research objective of the thesis work is formulated as:

To develop an orbit prediction algorithm for SAOCOM-CS satellite that results in a reliable orbit prediction for one day with a maximum position error norm of 125 *m, by tuning the relevant factors to improve the drag force modelling of the satellite.*

It should be noted that the data from PROBA-V and GRACE mission is used in this thesis work. Though SAOCOM-CS mission got cancelled during the course of this thesis work, the analysis presented here can still be adapted to other satellites in LEO based on the corresponding orbit and satellite parameters.

1.4 Outline

The rest of the report is divided into six chapters which sequentially address the various aspects of the research objective. Chapter 2 provides the relevant theory for orbit estimation and prediction techniques considered for this thesis work. It describes the type of data used for processing as well as the procedure used for the selection of periods for the orbit estimation and prediction. Chapter 3 discusses the outcomes of orbit estimation and prediction done on GRACE-A and PROBA-V with one drag scale factor (C_d) per day and Chapter 4 discusses the results of estimation and prediction done with multiple drag scale factors per day and uses the results obtained from the two satellites to assess the performance of the orbit prediction of SAOCOM-CS. Chapter 5 deals with the effects of the space weather forecast on the satellite orbit prediction. Chapter 6 provides a sensitivity analysis of the various force models used in orbit estimation and prediction. This is ensued by strategies to optimize estimation and prediction for the computational efficiency of PROBA-V. Finally, Chapter 7 summarizes the results of this thesis work and presents the conclusions to the reader along with an outlook of future research in this direction.

Chapter 2

Orbit determination and prediction using GPS state vector data

This chapter deals with the force models and observation models required for the orbit estimation and prediction schemes. Section 2.1 briefly reviews the three types of tracking data that were considered for this thesis work and provides the specifications of the tracking data chosen and used in this thesis work. Section 2.2 provides a comprehensive overview of the force models, observation models and the estimation techniques used. Section 2.3 describes the different orbit prediction methods considered. Section 2.4 briefly describes TUDAT (TUDelft Astrodynamics Toolbox), the orbit determination and prediction software used in this thesis and Section 2.5 briefly explains the procedure for selecting the periods to obtain data for the orbit estimation and prediction.

2.1 Review of tracking data types and specifications of GPS state vector data

Three types of tracking data were investigated for this thesis work: raw GPS data, Two-Line Elements (TLEs) and the GPS navigation solution, hereinafter referred to as the GPS state vector data. Raw GPS data consists of ranging codes and other necessary data for navigation operations, superimposed on the carrier waves which are transmitted in two frequencies known as L_1 and L_2. The ranging codes consist of Coarse Acquisition (C/A) code, Precise (P) code and the Y code. PROBA-V which uses a single frequency GPS receiver, can only make use of C/A code. This reduces the accuracy of the measurement as it relies on less accurate ionosphere models to remove first order ionosphere effects. This problem is mitigated in GRACE satellite which uses a dual frequency GPS receiver with effective and advanced signal processing techniques [Tapley et al., 2004a].

The TLE, distributed by the Joint Space Operations Centre (JSpOC), consists of two lines of just 69 characters which provide orbital information on a large number of Earth orbiting objects. The position and velocity information of a satellite can be obtained by reconstructing its orbit through the application of the SGP4 algorithm to the TLE data [Vallado and Crawford, 2008]. In an accuracy analysis performed by Doornbos [2012] on the TLE of CHAMP (Challenging Minisatellite Payload) and GRACE satellites for epochs free of orbit manoeuvres, it was found that the relative error in the estimated

density due to the TLE orbit error of 0.5 km in the along-track direction [Flohrer et al., 2008], stayed below 1%, even if the time with respect to optimal epoch amounted to several days. Hence, TLEs can be used as a reliable tool for density studies and, if the orbit error is less than 0.2 km, can also be used for orbit prediction analysis of satellites in the very low LEO.

The three dimensional Cartesian position, velocity and the corresponding epoch constitute the state vector data of a satellite. This uniquely defines the trajectory of a satellite. The state vector data is obtained by processing the raw GPS data received by the satellite. Mathematically, the state vector is expressed as,

$$\mathbf{X} = [t \;\; x \;\; y \;\; z \;\; V_{\mathrm{x}} \;\; V_{\mathrm{y}} \;\; V_{\mathrm{z}}]^{\mathrm{T}} \tag{2.1}$$

For PROBA-V, the state vector data is computed on-board and received by the ground station as telemetry data. This is then acquired by Qinetiq Space and used for various purposes. Hence, the accuracy of state vector depends on the quality of the GPS receiver and the on-board processing capacity. For GRACE-A, the state vector data is available as level 1B data product which is obtained by processing both the Level-1A and Level-0 data [Case et al., 2002]. The state vector of GRACE-A is more accurate than the state vector of PROBA-V mainly due to two reasons: more accurate raw GPS data of GRACE-A due to the high quality dual frequency GPS receiver and the complex processing of this data done using ground based processing facilities. Other parameters of the tracking data relevant to this thesis work are summarized in Table 2.1. The state vector data of both satellites are time-tagged with the GPS time, defined as the number of seconds since the epoch January 01, 2000, 12:00 hrs [Bettadpur, 2012]. For this thesis work, the state vectors of both satellites (PROBA-V and GRACE-A) are defined with respect to the Earth-Centered Earth Fixed (ECEF) reference frame. The origin for this reference system is at the centre of mass of the Earth. The XY plane coincides with the equatorial plane of the Earth with the X-axis passing through the Greenwich meridian and Y-axis at 90° to the east of X-axis in the equatorial plane. The Z-axis is perpendicular to the equatorial plane and passes through the North Pole. This reference system rotates along with Earth.

Comparing the three tracking data types, the TLE has the least accuracy. Flohrer et al. [2008] provides a look-up table which gives the average estimated uncertainties of the TLE orbits of the satellites with perigee altitude less than 800 km and eccentricity less than 0.1. Combining the uncertainties in radial, along-track and cross-track directions, the total uncertainty comes to around 0.45 km. With this accuracy, it is not possible to achieve the research objective of this thesis mentioned in Section 1.3. Though using raw GPS data has more advantages than using GPS state vector data, it is not preferred by Qinetiq Space for various reasons. One reason is the limited down-link capacity which restricts the collection of raw GPS data from PROBA-V satellite. Moreover, the complexity of orbit determination is greatly reduced when using the state vector data. Because of these advantages, the state vector data is used in this thesis work. During the thesis, it was found that there were certain days in which the state vector data of PROBA-V had large gaps which caused failure of the orbit determination algorithm. These days were removed from processing and this is explained in Section 2.5. Among the twin GRACE satellites, the state vector data of GRACE-A is used for this thesis, due

[1]RMS = Root Mean Square

Parameters	PROBA-V	GRACE-A
GPS receiver (manufacturer)	Phoenix (DLR)	BlackJack (JPL)
Receiver type	Single frequency	Dual frequency
Raw GPS data measurements (in RMS[1])	L1 C/A code noise: 0.40 m, L1 carrier phase noise: 0.50 mm, Range rate noise from carrier phase: 2 cm/s, Smoothed pseudorange noise: 0.10 m	Ionosphere- free phase noise is less than 0.20 cm, Ionosphere-free range noise is less than 30 cm.
Reference frame of navigation solution	ECEF	ECEF
Availability of navigation solution	Every 60 seconds	Every 5 seconds
3D RMS of navigation solution	Position: 2.50 m, Velocity: 0.06 m/s	Position: 3.70 mm Velocity: 6 μm/s
Source of navigation solution	Qinetiq Space database	JPL database

Table 2.1: Parameters of GPS receivers and their navigation solution.

to less number of manoeuvres compared to GRACE-B. The selection process is further explained in Section 2.5.

2.2 Orbit determination scheme

This section describes the force models, observation models and the application of batch least squares estimation technique. It is accompanied by short descriptions of the time system and the various reference systems used by the orbit determination software. A concise description of this section can be found in Tables 2.2 and 2.3. The orbit determination and prediction in this thesis work is carried out using TUDAT, an in-house C++ software. Implementation of force models and observation models in TUDAT is briefly mentioned in Section 2.2.1. More information on the selection and overview of the software can be found in Section 2.4.

2.2.1 Force models and observation models

The acceleration experienced by a satellite in LEO is given by the expression [Doornbos, 2012],

$$\ddot{\mathbf{r}} = -\frac{\mu}{r^2}\hat{\mathbf{r}} + \ddot{\mathbf{r}}_{\text{eg}} + \ddot{\mathbf{r}}_{\text{3b}} + \ddot{\mathbf{r}}_{\text{t}} + \ddot{\mathbf{r}}_{\text{gr}} + \ddot{\mathbf{r}}_{\text{a}} + \ddot{\mathbf{r}}_{\text{srp}} + \ddot{\mathbf{r}}_{\text{erp}} + \ddot{\mathbf{r}}_{\text{other}} \tag{2.2}$$

where $-\frac{\mu}{r^2}\hat{\mathbf{r}}$ is the Newtonian gravitational acceleration, $\ddot{\mathbf{r}}_{\text{eg}}$ is the acceleration due to the irregularities in Earth's gravity field, $\ddot{\mathbf{r}}_{\text{3b}}$ is the gravitational acceleration due to third bodies, $\ddot{\mathbf{r}}_{\text{t}}$ is the acceleration due to tidal effects, $\ddot{\mathbf{r}}_{\text{gr}}$ is the acceleration due to the effects of general relativity, $\ddot{\mathbf{r}}_{\text{a}}$ is the aerodynamic acceleration, $\ddot{\mathbf{r}}_{\text{srp}}$ is the acceleration due to the solar radiation pressure, $\ddot{\mathbf{r}}_{\text{erp}}$ is the acceleration due to Earth radiation pressure and $\ddot{\mathbf{r}}_{\text{other}}$ represents other accelerations. Except for the acceleration due to the Newtonian

gravity potential ($-\mu/r^2$), this section provides concise descriptions for other accelerations ($\ddot{\mathbf{r}}_{\text{eg}}$, $\ddot{\mathbf{r}}_{\text{3b}}$, ..., $\ddot{\mathbf{r}}_{\text{other}}$).

Spherical harmonics of Earth

The gravitational potential at a point outside the radially asymmetric mass density distributed Earth is given by the following expression [Wakker, 2015],

$$U = -\frac{\mu}{r}\left[1 - \sum_{\text{n=2}}^{\infty} J_{\text{n}}\left(\frac{R}{r}\right)^{\text{n}} P_{\text{n}}(\sin\phi) + \sum_{\text{n=2}}^{\infty}\sum_{\text{m=2}}^{\text{n}} J_{\text{n,m}}\left(\frac{R}{r}\right)^{\text{n}} P_{\text{n,m}}(\sin\phi)(\cos\text{m}(\Lambda - \Lambda_{n,m})\right] \quad (2.3)$$

where R is the mean equatorial radius of the Earth, r is the distance of the point from the centre of mass of the Earth, ϕ is the geocentric latitude of the point, Λ is the geographic longitude of the point, μ is the gravitational parameter of the Earth, J_{n}, $J_{\text{n,m}}$ and $\Lambda_{\text{n,m}}$ are the model parameters, $P_{\text{n}}(\sin\phi)$ are Legendre polynomials of degree n, $P_{\text{n,m}}(\sin\phi)$ are associated Legendre functions of the first kind of degree n and order m. TUDAT numerically computes the potential by making use of the model parameters (i.e. gravity coefficients) obtained from the model ITU_GRACE 16 [Shang et al., 2015]. Under nominal conditions, the degree and order of the model are set to 50. Using a degree and an order higher than 50 did not significantly improve the accuracy of orbit determination and prediction, but cost more computation time. The satellite is considered as a point mass. The changing mass of GRACE-A due to propellant usage from manoeuvres is obtained from the satellite housekeeping files [Case et al., 2002] for the period under consideration and is included in TUDAT computations. Since PROBA-V has no propellant usage, its mass remains constant throughout the processing period. The shape of Earth is considered as an oblate sphere with a reference radius of 6378 km and a flattening parameter of 1/298.25 [Slater and Malys, 1998].

Third body perturbation

A satellite in LEO is influenced by the gravitational forces of the celestial bodies other than Earth. These effects are known as the third body perturbations. The maximum value of the ratio of the magnitude of the acceleration due to the third body to the magnitude of the acceleration due to the Newtonian gravity field of the Earth is given by [Wakker, 2015],

$$\left|\frac{\ddot{\mathbf{r}}_{\text{d}}}{\ddot{\mathbf{r}}_{\text{E}}}\right|_{\text{max}} \approx 2\,\frac{m_{\text{d}}}{m_{\text{E}}}\left(\frac{r}{r_{\text{d}}}\right)^3 \quad (2.4)$$

where m_{d} is the mass of the disturbing body, r_{d} is the distance of the disturbing body from the centre of the Earth, m_{E} is the mass of the Earth and r is the distance of the satellite from the centre of the Earth. It is evident from Equation (2.4) that the relative perturbing acceleration increases with orbital altitude of the satellite. TUDAT numerically computes the perturbing accelerations due to the Sun and the Moon. Both the perturbing bodies and satellites are considered as point masses. The required positions of the Earth, the Sun and the Moon with respect to the Solar System Barycenter (SSB) in the inertial frame J2000 are obtained from the SPICE toolkit provided by NASA's JPL [Acton et al., 2015].

Tides

The gravitational force exerted on Earth by other celestial bodies (such as the Sun and the Moon) varies as a result of eccentricity of the orbit of the celestial bodies and the rotation of the Earth. This results in a difference between the gravitational pull at the surface of the Earth and the gravitational pull experienced at the centre of the Earth which produces long waves on the Earth's surface known as tides. Using the addition theorem of Legendre functions [Lambeck, 1988], the tide induced potential at the satellite altitude due to a planetary body is given by,

$$U'(r_{\mathrm{s}}) \;=\; \frac{\mu_{\mathrm{p}}}{r_{\mathrm{E}}} \sum_{\mathrm{n}=2}^{\infty} \left(\frac{r_{\mathrm{E}}^2}{r_{\mathrm{s}}\, r_{\mathrm{p}}} \right)^{\mathrm{n}+1} \frac{k_{\mathrm{n}}}{2\mathrm{n}+1} \sum_{\mathrm{m}=0}^{\mathrm{n}} \overline{P}_{\mathrm{nm}}\left(\cos\theta_{\mathrm{p}}\right) \overline{P}_{\mathrm{nm}}\left(\cos\theta_{\mathrm{s}}\right) \cos(\mathrm{m}(\lambda_{\mathrm{s}} - \lambda_{\mathrm{p}})) \tag{2.5}$$

where $(r_{\mathrm{s}},\, \theta_{\mathrm{s}},\, \lambda_{\mathrm{s}})$ and $(r_p,\, \theta_p,\, \lambda_p)$ are the spherical co-ordinates of the satellite and the planet, respectively, in the terrestrial frame, μ_{p} is the gravitational parameter of the planetary body, r_{E} is the reference radius of the Earth, k_{n} represents the Love numbers and $\overline{P}_{\mathrm{nm}}\left(\cos\theta_{\mathrm{p}}\right)$ represents the associated Legendre functions of degree n and order m. The dominant Love number of the Earth was obtained from the observations of polar motion [Seitz et al., 2012]. TUDAT numerically computes the tidal acceleration resulting from the deformation of solid Earth due to the Sun and the Moon. This is based on IERS (International Earth rotation and Reference System service) 2010 [Petit and Luzum, 2010]. Highly precise ephemeris for the positions of the Sun, the Moon and the Earth are obtained from the SPICE database. Rotational ephemeris of the Earth is also provided by SPICE database. This includes the realizations of precession, nutation, polar motion and Earth rotation based on IAU (International Astronomical Union) 2000/2006 resolutions [Petit and Luzum, 2010]. Ocean tides model is not included as the functionality was not implemented in TUDAT. The impact of excluding the ocean tides model on the radial orbit error is expected to be one order of magnitude greater than the effect of the solid Earth tides model on the radial orbit error [Scharroo and Visser, 1998].

Radiation force

Solar radiation pressure is a non-gravitational and a non-conservative force. At higher altitudes, the effect of radiation pressure on the satellite surface produces considerable orbit perturbations over long periods of time, except during eclipses, when there is no sunlight. The acceleration of a satellite due to solar radiation pressure is expressed as [Doornbos, 2012],

$$\ddot{\mathbf{r}}_{SRP} \;=\; C_{\mathrm{R}}\, \frac{W\, A_{\mathrm{ref}}}{c\, M} \hat{\mathbf{r}}_{\odot\, s} \tag{2.6}$$

where W is the power density of the solar radiation near Earth and has a value of 1360 W/m^2, M is the mass of the satellite, c is the velocity of light in vacuum, $\hat{\mathbf{r}}_{\odot\, s}$ is the unit vector from the Sun to satellite and C_{R} is the radiation pressure coefficient associated with the reference area of the satellite, A_{ref}. Radiation force results from two kinds of reflection at the satellite surface: specular and diffuse, the details of which can be found in Doornbos [2012] and Sengoku et al. [1995]. For a realistic solar radiation pressure calculation, the varying distance between the Sun and the satellite has to be considered. Applying the inverse square law, the solar radiation pressure can be expressed as [Doornbos, 2012],

$$P \;=\; \left(\frac{1AU}{r_{\odot\, s}} \right)^2 f_{\mathrm{s}}\, P_{\mathrm{1AU}} \tag{2.7}$$

where $P_{1\mathrm{AU}} = 4.56 * 10^{-6}$ N/m^2, $1AU = 149,597,870,660$ m, f_s is the shadow function [Vallado, 2001] and $r_{\odot s}$ is the varying Sun-satellite distance. TUDAT numerically computes the acceleration due to solar radiation pressure by considering the satellite as a cannonball and Earth as the occulting body [Lucchesi, 2002]. SPICE database is used to compute the varying Sun-satellite distance. For GRACE-A, the reference area for radiation is fixed as 6.0711 m^2 [Bettadpur, 2012], which is the area of the largest panel, to include worst case perturbation. Since PROBA-V resembles a rectangular cube, the maximum cross-sectional area of 1.1314 m^2 (Table 1.1) is used as the reference area. The initial values for the radiation pressure coefficient (C_R) are calculated based on the surface properties of GRACE-A [Bettadpur, 2012] and PROBA-V (Personal communication: Dr. Joris Naudet, Qinetiq Space). These values are then input to the batch least squares estimator for further processing. Modelling of Earth radiation pressure, which includes the sunlight reflected by the Earth and the thermal radiation from the Earth, is not available in TUDAT. Earth radiation pressure has little effect on the drag force modelling of the satellites, because its magnitude is relatively small and it acts in the radial direction [Doornbos, 2012]. Moreover, implementation of this force model requires computation of the time-varying reflectivity of the Earth and factoring the Sun-Earth-satellite geometry [Knocke et al., 1988]. Since these are beyond the scope of this thesis, it is decided to exclude the Earth radiation pressure.

Atmospheric force

The interaction between the Earth's atmosphere and a satellite in the very low LEO results in a non-conservative force which is hard to predict and model. The acceleration due to atmospheric drag force is given by [Doornbos, 2012],

$$\ddot{\mathbf{r}}_\mathrm{D} = \frac{1}{2}\,\rho\,\frac{A_\mathrm{ref}}{M}\,C_\mathrm{d}\,v_\mathrm{r}^2\,\hat{\mathbf{v}}_\mathrm{r} \tag{2.8}$$

$$\mathbf{v}_\mathrm{r} = \mathbf{v}_\mathrm{r,i} + \mathbf{v}_\mathrm{r,c} + \mathbf{v}_\mathrm{r,w} \tag{2.9}$$

where ρ is the atmospheric density, M is the mass of the satellite, C_d is the drag coefficient of the reference surface A_ref, $\mathbf{v}_\mathrm{r}$ is the relative velocity vector, $\mathbf{v}_\mathrm{r,i}$ is the inertial velocity of the satellite in its orbit, $\mathbf{v}_\mathrm{r,c}$ is the velocity caused by the co-rotating atmosphere and $\mathbf{v}_\mathrm{r,w}$ denotes the velocity of winds. Generally, the density of the Earth's atmosphere is considered to decrease exponentially with altitude. However, for precise orbit determination and prediction this approximation is not enough and hence thermosphere density models are used. Besides the exponential decrease of density with altitude, these models include several other density variations such as diurnal variation, seasonal variation, semi-annual variation, solar activity variation and geomagnetic activity variation. All these variations are due to the temporal and spatial differences in the energy and heat input into the atmosphere. Emmert [2015] gives a comprehensive account of these variations.

Thermosphere models can be broadly classified into physical models and empirical models. Physical models, based on the governing physical equations of the atmosphere system, provide the detailed response of density, temperature, composition and winds to the diverse energy inputs to the atmosphere (e.g. Thermosphere Global Circulation Models (TGCMs)). Compared to empirical models, physical models are more complex, requiring more expertise to run and are computationally intensive. Hence, they are not preferred for routine applications in orbit determination. On the other hand, empirical models provide only the major variations in the number densities of the major constituents

of the atmosphere through relatively simple functions, resulting in total density and temperature as the usual outputs [Doornbos, 2012]. Two modes of gas-surface interaction are generally recognized: specular re-emission and diffuse re-emission. Quantification of these re-emissions based on the atmospheric composition at higher altitudes can be found in Harrison and Swinerd [1996] and Pilinski et al. [2010]. The outputs from the thermosphere model, together with the state vector data of a satellite and the gas-surface interaction model, included in a numerical propagator can represent the low density flow encountered at LEO altitude. Some of the important empirical models are the Jacchia series [Bowman et al., 2006, 2008, Jacchia, 1972], the DTM (Drag Temperature Model) series [Berger et al., 1998, Bruinsma et al., 2003] and the MSIS (Mass Spectrometer Incoherent Scattering radar) series [Hedin, 1987, Picone et al., 2002]. Among these empirical models, NRLMSISE-00 (Naval Research Laboratory-Mass Spectrometer and Incoherent Scatter radar Exosphere-00) is used in this thesis due to its availability in TUDAT.

The inputs to the NRLMSISE-00 model [Picone et al., 2002] in TUDAT are the (GPS) time, geodetic altitude, geodetic latitude, longitude, solar and geomagnetic activity data. The outputs include the number densities of the major atmospheric constituents, anomalous oxygen number density, total mass density, exospheric temperature and the temperature at the given altitude. Solar and geomagnetic activity data are obtained from the publicly available `http://celestrak.com/SpaceData/` website. The extent of solar EUV energy input into the atmosphere of Earth due to solar activity can be represented by the amount of heat flux received by the Earth at 10.7 cm radio-wavelength. This is called the solar activity proxy. It is expressed in solar flux units (1 sfu = 10^{-22} $Wm^{-2}Hz^{-1}$). The NRLMSISE-00 model requires two such parameters: the daily observed solar radio flux ($F_{10.7}$) and the centered 81-day average radio flux ($F_{10.7A}$). Similarly, geomagnetic activity can be represented by a_p in units of nanoTesla (nT). The period of a_p is 3 hours which amounts to 8 values per day. The average of all 8 a_p values in a UTC (Universal Time Co-ordinated) day is denoted as the A_p index. More information about the geomagnetic indices can be found in Menvielle and Berthelier [1991]. NRLMSISE-00 model takes the 8 a_p values and the single A_p index as inputs. Wind model is not considered for this thesis as the orbital velocity of the satellite is much greater than the wind velocity at 620 km altitude of the planned SAOCOM-CS mission.

Density provided by the NRLMSISE-00 model is used by TUDAT to numerically compute the acceleration due to drag force by considering the satellite as a cannonball. The reference area for GRACE-A is fixed as 1.0013 m^2 [Bettadpur, 2012] and for PROBA-V, the reference area is 1.1314 m^2. These values are the frontal areas of both satellites (Table 1.1). A value between 2 and 3 is given as the initial value for the drag coefficients (or drag scale factors, C_d) of both satellites [Wakker, 2015]. These values are then iteratively improved through the batch least squares estimator. According to the analysis by Cook [1964], atmospheric lift force produces significant perturbations to the orbit of a stabilized disk shaped satellite under certain conditions. This is not relevant to this thesis as disk shaped satellites are not considered. In an analysis performed by Doornbos [2012] on the CHAMP (CHAllenging Mini-satellite Payload) and GRACE satellites, it was found that the lift coefficient was very small ($C_l = 0.06$) compared to the drag coefficient ($C_d = 2.80$). Since PROBA-V orbits at a higher altitude, the effect of lift force on orbit perturbations can be assumed to be negligible. For these reasons, it is decided to exclude the lift force.

Other forces

Under the influence of Earth's magnetic field, a satellite can experience Lorentz force if it acquires an overall negative or positive potential through mechanisms such as bombardment of the satellite by high thermal velocity electrons, surface degradation of the satellite from high-energy photons, etc. This force is excluded from this thesis for the following reasons: the various mechanisms mentioned are significant only at altitudes over 1000 km; there is no in-situ observation data on satellite ionization and the Earth's magnetic field mostly affects the attitude of the satellite with very little effect on the orbit of the satellite. Owing to differential heating of its components, a satellite in orbit experiences thermal self radiation which may produce drag-like characteristics. These effects are small and a general rule of thumb is that when the satellite is in thermal equilibrium, the thermal self radiation is a fraction of the solar radiation pressure (SRP) and acts in the same direction as the SRP. Hence, the thermal self radiation is usually modelled as an error in SRP [Larson and Wertz, 1992]. The light-time corrections based on special and general relativity and due to oblateness of the Earth [Larson et al., 2007], usually required when using raw GPS data, are not relevant for this thesis as the state vector data is used (Section 2.1). The relativistic precession of the argument of latitude of the satellite orbit can also be neglected as it has an order of magnitude below the error level of the force models considered.

Observation model

Since the GPS state vector data is used as measurement for this thesis, the observation model is straightforward: the state of the satellite involved in the numerical integration process is also the observation. Hence, the observation vector at a given epoch t is,

$$\mathbf{Y}(t) = [x \;\; y \;\; z \;\; V_{\mathrm{x}} \;\; V_{\mathrm{y}} \;\; V_{\mathrm{z}}]^{\mathrm{T}} \tag{2.10}$$

The epoch is provided in the GPS time (Section 2.1) whereas TUDAT uses the Terrestrial Time (TT) [Petit and Luzum, 2010]. The conversion from GPS time to TT is given by,

$$\mathrm{TT} = \mathrm{GPS\ time} \;+\; 19 \;+\; 32.18 \text{ seconds} \tag{2.11}$$

The Cartesian position and velocity are available in the ECEF reference frame whereas TUDAT uses J2000 as the Earth Centered Inertial (ECI) frame during numerical integration. The transformation between the position co-ordinates of ECEF and ECI is given by [Tapley et al., 2004a],

$$\begin{bmatrix} x \\ y \\ z \end{bmatrix}_{\mathrm{ECEF}} = \mathbf{WS'NP} \begin{bmatrix} X \\ Y \\ Z \end{bmatrix}_{\mathrm{ECI}} \tag{2.12}$$

where $\mathbf{P}$, $\mathbf{N}$, $\mathbf{S'}$ and $\mathbf{W}$ denote the transformation matrices to account for precession, nutation, Earth rotation and polar motion respectively. The transformation between the velocity components of ECEF and ECI is given by [Montenbruck and Gill, 2000],

$$\begin{bmatrix} V_x \\ V_y \\ V_z \end{bmatrix}_{\mathrm{ECEF}} = \mathbf{WS'NP} \begin{bmatrix} V_X \\ V_Y \\ V_Z \end{bmatrix}_{\mathrm{ECI}} + \mathbf{W}\frac{d\mathbf{S'}}{dt}\mathbf{NP} \begin{bmatrix} X \\ Y \\ Z \end{bmatrix}_{\mathrm{ECI}} \tag{2.13}$$

The components of the transformation matrices are available in Petit and Luzum [2010]. The outputs of numerical integration in the ECI frame are transformed into the radial,

along-track, cross-track (RSW) frame for the ease of representation. Documentation regarding this conversion is available at `http://doxygen.tudat.tudelft.nl/d2/d70/reference_frame_transformations_8cpp.html` website. The standard deviations of the observed Cartesian position and velocities of GRACE-A and PROBA-V are mentioned in Table 2.1. These are used as weights in the batch least squares estimator.

2.2.2 Batch least squares estimation

In the reduced-dynamic orbit determination approach, the orbit of a satellite is determined by considering the observations of the satellite and the dynamics of the satellite motion. This allows for precisely computing the orbit of a satellite as well as to propagate it when there are gaps in the observation. The accuracy of the computed orbit depends on the quality of the force models used for the satellite dynamics and the quality of the observations. Neither the model nor the observations is perfect. Hence, physical parameters such as drag coefficient (or drag scale factor, C_d), radiation pressure coefficients (C_R) are introduced into the force model to absorb modelling errors. Initial weights are assigned to the force model and to the observations based on their quality. They are optimally combined to get the best estimate of the orbit and force model parameters in an iterative manner. Two well known methods of reduced dynamic orbit determination are the batch least squares estimation and Kalman filter estimation. In an analysis of the reduced dynamic orbit determination of GRACE using GPS code and carrier measurements by Montenbruck et al. [2005], it was found that the extended Kalman filter required less computer resources such as memory and processing time while the batch least square estimator ensured a better smoothness of the resulting trajectory and was more robust in case of data gaps. Batch least squares estimation was chosen for this thesis as it was readily available in TUDAT with the functionality to estimate several model parameters including drag coefficient (or drag scale factor, C_d).

Least squares technique minimizes the sum of the squares of the residuals with respect to the parameters considered for estimation. Thus, the cost function to be minimized is given by [Vallado, 2001],

$$J \;=\; \sum_{\mathrm{i}=1}^{\mathrm{N}} \overline{r}_{\mathrm{i}}{}^{2} \tag{2.14}$$

where N is the total number of data points or observations and $\overline{r}_{\mathrm{i}}$ is the residual of the i^{th} data point or observation. The estimated parameters only direct the solution as the solution is predetermined based on some assumptions such as the shape of the orbit, drag model, etc., before the minimization of the cost function. The estimated parameters are given by the expression [Vallado, 2001],

$$\hat{\mathbf{X}} \;=\; (\mathbf{A}^{\mathbf{T}}\,\mathbf{A})^{-\mathbf{1}}\,\mathbf{A}^{\mathbf{T}}\,\mathbf{b} \tag{2.15}$$

where $\hat{\mathbf{X}}$ is the state space vector which contains the estimated parameters, $\mathbf{A}$ is the matrix of partial derivatives of the residuals with respect to the estimated parameters, $\mathbf{b}$ is the observation vector and $(\mathbf{A}^{\mathbf{T}}\,\mathbf{A})^{-\mathbf{1}}$ is the covariance matrix which provides uncertainties of the estimated parameters. There are extra parameters that appear in the model formulation but are not estimated through processing. The effect of uncertainty of these parameters on the covariance can be included through consider parameters [Bierman, 2006]. If some observations are considered as more accurate than other observations,

then weighted least squares technique is used. In this case, the estimated parameters are given by the expression [Vallado, 2001],

$$\hat{\mathbf{X}} \;=\; (\mathbf{A^T\,W\,A})^{-1}\,\mathbf{A^T\,W\,b} \tag{2.16}$$

and

$$\mathbf{W} \;=\; {w_{\mathrm{i}}}^{T}\,w_{\mathrm{i}} \tag{2.17}$$

$$w_{\mathrm{i}} \;=\; \frac{1}{\sigma_{\mathrm{i}}} \tag{2.18}$$

where $\mathbf{W}$ is the weighting matrix, σ_{i} is the standard deviation of the i^{th} observation and $(\mathbf{A^T\,W\,A})^{-1}$ is the covariance matrix. Since precise orbit determination is a non-linear problem, a set of nominal state space vector, $\mathbf{X_0}$ is assumed as the initial state and a Taylor series expansion about this nominal state space is done. Neglecting the higher order terms, this is now used, along with the weights of the observations, in the least squares method to determine the corrections to the nominal state to obtain a better estimate. This non-linear weighted least squares approach is given by the expression [Vallado, 2001],

$$\delta\hat{\mathbf{x}} \;=\; (\mathbf{A^T\,W\,A})^{-1}\,\mathbf{A^T\,W}\,\tilde{\mathbf{b}} \tag{2.19}$$

$$\delta\hat{\mathbf{x}} \;=\; \mathbf{P\,A^T\,W}\,\tilde{\mathbf{b}} \tag{2.20}$$

where $\delta\hat{\mathbf{x}}$ is the vector containing the estimated corrections to the nominal state space vector, $\mathbf{P}$ is the covariance matrix, $\tilde{\mathbf{b}}$ is the residual matrix formed by the difference between the observation and the nominal value computed using the nominal state space and $\mathbf{A}$ is the matrix of partial derivatives of the residuals with respect to the nominal state space. The estimated $\delta\hat{\mathbf{x}}$ is added to the nominal state space, $\mathbf{X_0}$ and the result becomes the new nominal state space vector. This is now used in the iteration to get a better estimate of $\delta\hat{\mathbf{x}}$. This iteration continues until a stopping criterion is met. In general, the stopping criterion is given by [Vallado, 2001],

$$\left|\frac{RMS_{\mathrm{old}} \;-\; RMS_{\mathrm{new}}}{RMS_{\mathrm{old}}}\right| \;\leq\; \epsilon \tag{2.21}$$

$$RMS \;=\; \sqrt{\frac{\tilde{\mathbf{b}}^T\,\mathbf{W}\,\tilde{\mathbf{b}}}{n_{\mathrm{obs}}\,(N\;-\;1)}} \tag{2.22}$$

where N is the number of observations, n_{obs} is the number of types of measurement associated with each observation and ϵ is the convergence tolerance. The partial derivative matrix, $\mathbf{A}$ is given by [Vallado, 2001],

$$\mathbf{A} \;=\frac{\partial(\mathrm{observations})}{\partial\mathbf{X_0}} \;=\; \frac{\partial(\mathrm{observations})}{\partial\mathbf{X}}\,\frac{\partial\mathbf{X}}{\partial\mathbf{X_0}} \tag{2.23}$$

$$\mathbf{A} \;=\; \mathbf{H}\,\mathbf{\Phi} \tag{2.24}$$

where $\mathbf{H}$ is the observation partials matrix and $\mathbf{\Phi}$ is the matrix of variational equations or the state transition matrix. The analytical and numerical formulations to compute both these matrices are provided in Vallado [2001] and the references mentioned therein. Using the state transition matrix, the estimated corrections vector, $\delta\hat{\mathbf{x}}$ and the covariance matrix $\hat{\mathbf{P}}$ are propagated to the current time as shown,

$$\delta\hat{\mathbf{x}} \;=\; \mathbf{\Phi}\,\delta\hat{\mathbf{x}}_0 \tag{2.25}$$

$$\hat{\mathbf{P}} \;=\; \mathbf{\Phi}\,\hat{\mathbf{P}}_0\,\mathbf{\Phi}^{\mathbf{T}} \tag{2.26}$$

The state transition matrix, $\mathbf{\Phi}$, being a linearized approximation of the dynamics, cannot be used for the propagation of the state space itself. Hence, the state space is propagated to the current time by using a suitable propagator.

TUDAT orbit determination algorithm performs the non-linear weighted least squares with batches of observations known as estimation arcs. Under nominal conditions, for both satellites, the estimation arc length is fixed as one day. For each estimation arc, the initial state of the satellite is obtained from the GPS state vector data corresponding to the initial epoch. The procedures for obtaining initial values of C_R and C_d were explained in Section 2.2.1. Cowell's method [Wakker, 2015] is used for propagation along with the fourth order Runge-Kutta integration scheme. Between both satellites, the GPS state vector of GRACE-A is more frequently available: every 5 seconds (Table 2.1). Hence, the stepsize is chosen as 5 seconds for ease of validation and better accuracy. Within each estimation arc, for each satellite, the observation vector ($\mathbf{b}$) is obtained from the corresponding state vector data. Similarly, the weighting matrix ($\mathbf{W}$) is computed according to Equations (2.17) and (2.18) based on the standard deviations of the observations provided in Table 2.1. The observation partials matrix ($\mathbf{H}$) and the state transition matrix ($\mathbf{\Phi}$) are numerically computed, based on the formulations of the force and observation models, and are included in the estimation process. Maximum number of iterations per estimation arc is set to 6 and the convergence tolerance (ϵ) is set to $1 * 10^{-20}$. The estimation process stops if either of these criteria is satisfied. Initially, the following parameters were estimated per estimation arc: the initial state of the vehicle, radiation pressure coefficient (C_R) and the drag coefficient (C_d). Hence, the parameter vector is given by,

$$\hat{\mathbf{X}} \;= [x \;\; y \;\; z \;\; V_{\mathrm{x}} \;\; V_{\mathrm{y}} \;\; V_{\mathrm{z}} \;\; C_R \;\; C_d]^{\mathrm{T}} \tag{2.27}$$

The estimated parameter vector ($\hat{\mathbf{X}}$) and the resulting trajectory constitute the outputs of the estimation process. The resulting trajectory is verified and validated by comparing it against the GPS state vector data of the corresponding satellites for the corresponding estimation arc. Since the stepsize of the integrator is 5 seconds, the resulting trajectory of PROBA-V is interpolated before validating with its state vector data which has a time step of 60 seconds.

In this estimation process, the conventional drag coefficient of the satellite (C_d) serves as a correction factor for errors in atmospheric density from the empirical model, errors in gas-surface interaction and attitude of the satellite. Hence in this thesis, C_d will be referred to as the drag scale factor. Figure 2.1 shows the variation of the correlation coefficient between the estimated C_R and C_d for both satellites during January, 2014. Since the correlation is less than 10%, it can be concluded that the solar radiation pressure is almost uncorrelated with the drag force. This is further supported by Figures 2.2a and 2.2b which show almost no correlation between the estimated C_d and β, the angle between the orbital angular momentum vector and sun-satellite vector. Further orbit determination results showed the estimates of C_R to be unreliable. From these initial results, it was decided to fix values for C_R of both satellites based on the estimations carried out during a period of low solar activity to ensure minimum influence of drag force. The value of C_R for GRACE-A was fixed to 0.57 and the value of C_R for PROBA-V was fixed to 1.34. These fixed C_R values are used for the rest of the analysis described in this report. Hence, the new parameter vector is given by,

$$\hat{\mathbf{X}} \;= [x \;\; y \;\; z \;\; V_{\mathrm{x}} \;\; V_{\mathrm{y}} \;\; V_{\mathrm{z}} \;\; C_d]^{\mathrm{T}} \tag{2.28}$$

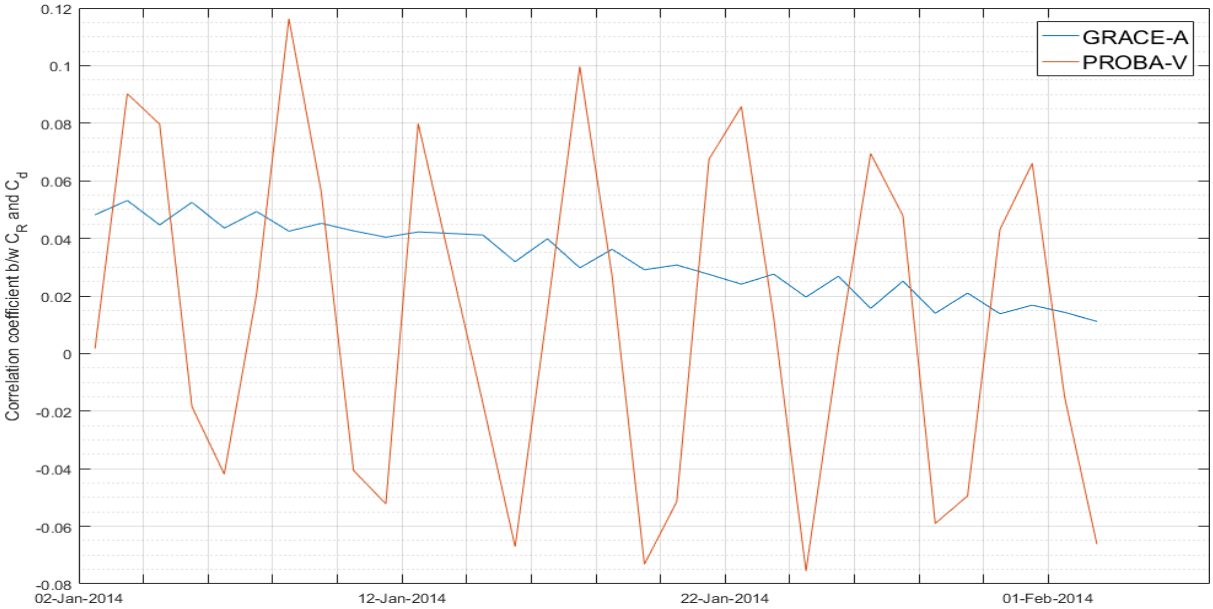

Figure 2.1: Correlation coefficient between the estimated radiation pressure coefficient (C_R) and drag scale factor (C_d) for GRACE-A and PROBA-V.

The following estimation schemes for C_d are considered for the thesis work to improve drag force modelling, which in turn will be required for orbit prediction (Section 2.3): single C_d per day and multiple C_d per day with 4 different resolutions - 2 C_d per day, 3 C_d per day, 4 C_d per day and 8 C_d per day. Among these resolutions, estimation of 4 scale factors per day has been done by researchers such as Doornbos et al. [2007] and Panzetta et al. [2019]. The choice of the resolution depends on the tracking information density and the strength of the drag signal in the tracking information.

2.3 Orbit prediction scheme

The main goal of this thesis, defined by the research question in Section 1.3 is orbit prediction. TUDAT orbit prediction algorithm propagates the orbit of both satellites (GRACE-A and PROBA-V) using the force models described in Section 2.2.1. It is noted here that the orbit prediction is done using the observed values of $F_{10.7}$ and A_p indices for the corresponding prediction arc and not the forecast values of the indices. This issue is addressed separately in Chapter 5. For nominal conditions, the arc length for prediction is same as that of estimation (i.e. one day). Given a satellite and a prediction arc, the initial state for prediction is obtained from the state vector corresponding to the last epoch in the resulting trajectory of the estimation output of previous day for that particular satellite. The drag scale factor (C_d) of a satellite for the prediction arc is also obtained from the estimated parameters of that satellite. The value of C_R is fixed as explained in Section 2.2.2. Encke's method [Wakker, 2015], which gives slightly more accurate results for orbit prediction than Cowell's method, is used along with the fourth order Runge-Kutta integration scheme with a stepsize of 5 seconds. The output of the prediction process is the predicted trajectory for one day. The accuracy of prediction is determined by comparing the predicted trajectory with the GPS state vector data of the corresponding satellite for the corresponding arc, similar to the validation mentioned in

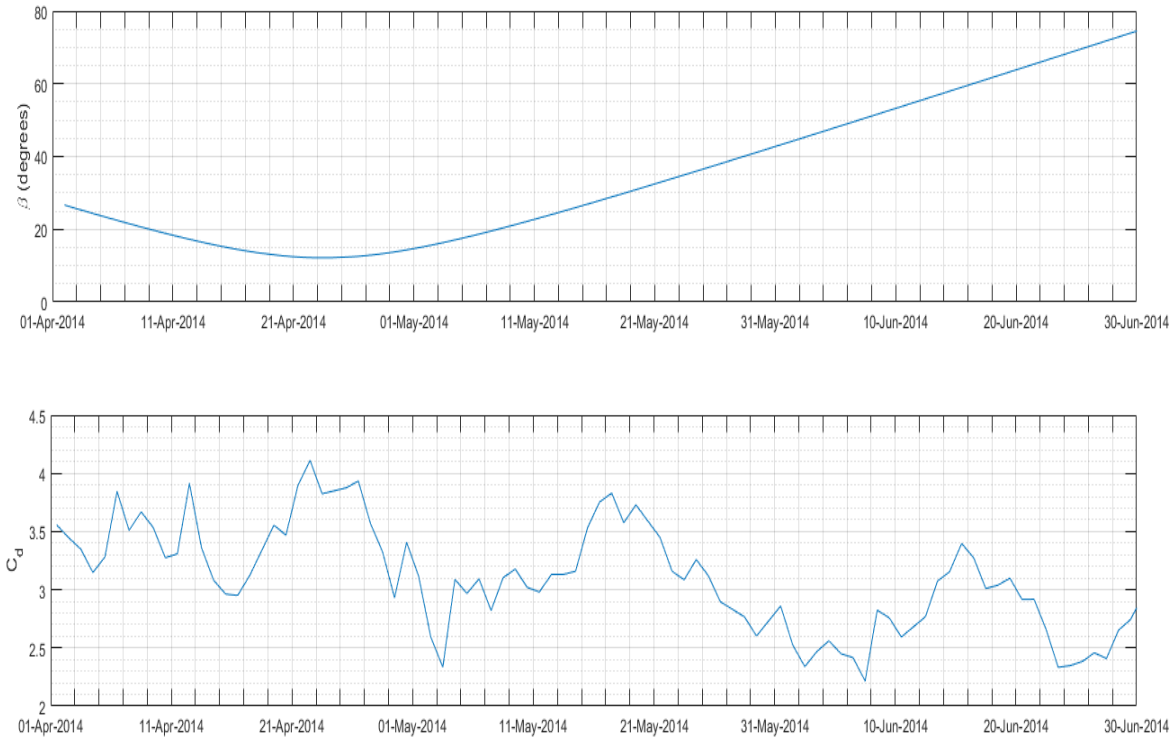

(a) Variation of the estimated C_d and β (angle between the orbital angular momentum vector and sun-satellite vector) for GRACE-A during April to June, 2014.

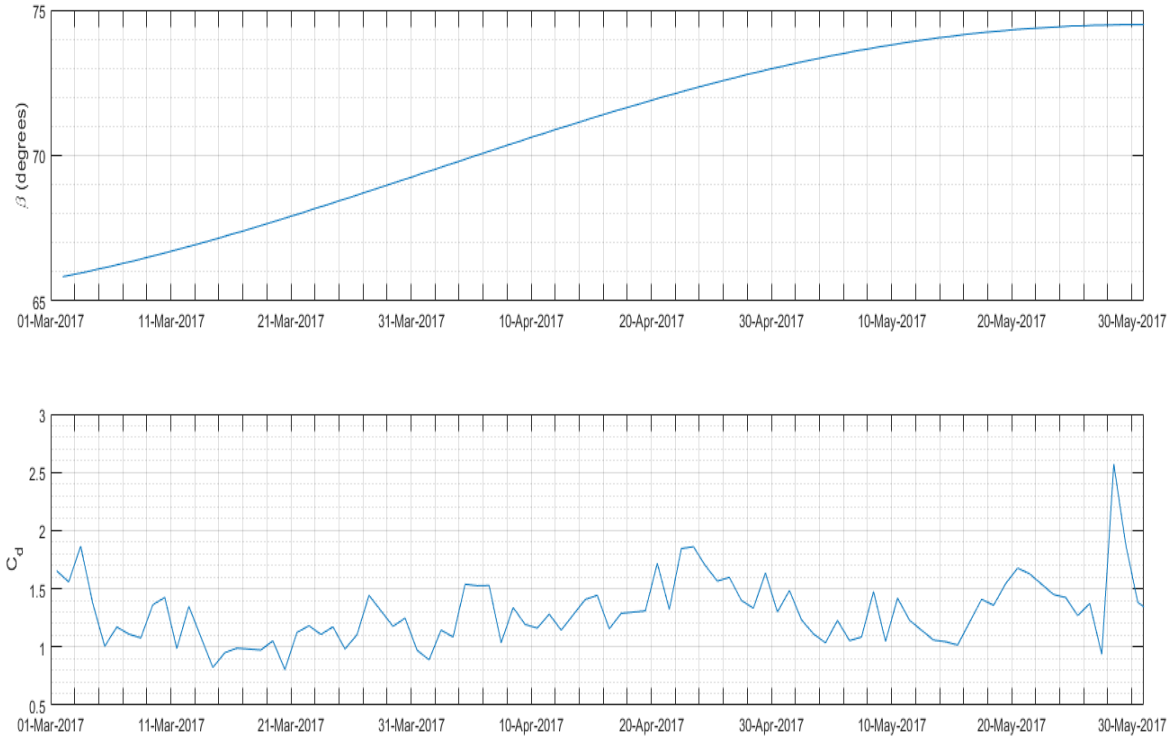

(b) Variation of the estimated C_d and β (angle between the orbital angular momentum vector and sun-satellite vector) for PROBA-V during March to May, 2017.

Figure 2.2

Model	Description with references
Measurement model:	
GPS state vector data	Obtained by processing raw GPS data of GRACE-A [Case et al., 2002] and PROBA-V (Source: Qinetq Space).
Position accuracy	GRACE-A: 3.70 mm, PROBA-V : 2.50 m
Velocity accuracy	GRACE-A : 6 μm/s PROBA-V : 0.06 m/s
Reference frame	ECEF
Time tag	GPS time [Bettadpur, 2012]
Gravitational force model:	
Earth gravity	ITU_GRACE 16 with degree and order 50 [Shang et al., 2015]
Solid Earth tides	IERS 2010 [Petit and Luzum, 2010]
Luni-solar gravity	SPICE ephemeris [Acton et al., 2015]
Non-gravitational force model:	
Atmospheric drag	NRLMSISE-00 density model [Picone et al., 2002] with solar activity inputs from `http://celestrak.com/SpaceData/` and estimated C_d per 24 hour arc.
Solar radiation pressure	Conical Earth shadow model [Lucchesi, 2002] with fixed C_R
Satellite model:	
Mass	GRACE-A: 487.20 kg at BOL with changing mass history [Case et al., 2002] PROBA-V: 138.00 kg
Surface model	Cannonball model with corresponding reference areas for GRACE-A [Bettadpur, 2012] and PROBA-V (Source: Qinetq Space).
Reference frame model:	
Precession, nutation, polar motion and Earth rotation	IAU 2000/2006 resolutions [Petit and Luzum, 2010]

Table 2.2: Description of the force models and measurement models used in precise orbit determination and prediction (Position and velocity accuracy are used as weights in the orbit determination. These conditions are applicable throughout this report unless stated otherwise.)

Section 2.2.2. This type of validation was also done by Jäggi et al. [2011].

Depending on the estimation scheme mentioned in Section 2.2.2, the following prediction schemes/methods are considered for the thesis work to arrive at the drag scale factor (C_d) for the prediction arc. This is done to determine the optimum prediction method for the satellites based on the solar activity period (Section 2.5):

- Estimation of single C_d per day:
  - Using the C_d of the previous day estimation as the C_d for the prediction arc. This is referred to as 'C_d of previous day' in this thesis
  - Using the estimated C_d of the previous week to obtain a third order polynomial fit. The C_d for the prediction arc is then obtained by extrapolating the polynomial. This is referred to as 'polyfit or polynomial fit of previous week C_d' in this thesis
  - Using the mean value of the estimated C_d of the previous week as the C_d for the prediction arc. This is referred to as 'mean C_d of previous week' in this thesis.
- Estimation of multiple C_d per day:
  - Using the last (i.e.most recent) C_d of the previous day estimation as the C_d for the prediction arc. This is referred to as 'last C_d of previous day' in this thesis.
  - Using the mean value of the estimated C_d of the previous day as the C_d for the prediction arc. This is referred to as 'mean C_d of previous day' in this thesis.
  - Using the mean value of the estimated C_d of the previous week as the C_d for the prediction arc. This is referred to as the 'mean C_d of previous week' in this thesis.
  - Using the estimated C_d of the previous week to obtain a third order polynomial fit. The C_d for the prediction arc is then obtained by extrapolating the polynomial. This is referred to as the 'polyfit or polynomial fit of previous week C_d' in this thesis.

For estimation using single C_d per day, all the mentioned prediction methods are carried out. However, this is not the case for estimation using multiple C_d per day. Since there are 2 satellites, each with 4 different C_d estimation schemes which in turn have 4 different prediction methods, it would result in a total of 32 different computations. To reduce the load on computation and subsequent analysis, a prediction metric is used to determine if the prediction method is necessary for a given satellite and estimation scheme. For a selected period (Section 2.5), the prediction metric PM, is defined as the root mean square (RMS) value of the differences between the predicted C_d and the estimated C_d of each day throughout the selected period. Mathematically,

$$PM \;=\; RMS\left((C_d)_{p,i} \;-\; (C_d)_{e,i} \right) \tag{2.29}$$

where $(C_d)_{p,i}$ is the predicted C_d for the i$^{\text{th}}$ day and $(C_d)_{e,i}$ is the estimated C_d for the i$^{\text{th}}$ day. When estimating multiple C_d per day, the mean of all the estimated C_d of a day

Parameter type	**Value**
Orbit determination:	
Estimation technique	Weighted least squares
Propagation method	Cowell
Integration method	Fourth order Runge-Kutta
Stepsize	5 seconds
Estimated parameters	Initial state and C_d
Inputs	Initial values of state vector and C_d, force model and measurements
Outputs	Estimated Initial state, C_d and resulting trajectory.
Resolution of estimated C_d	Single C_d per day, multiple C_d per day (2,3,4,and 8 C_d per day)
Validation	GPS state vector data
Orbit prediction:	
Propagation method	Encke
Integration method	Fourth order Runge-Kutta
Stepsize	5 seconds
Inputs	Estimated final state vector and C_d of previous day, force model
Outputs	Propagated trajectory
Prediction methods under single C_d per day estimation	C_d of previous day, Polynomial fit of previous week C_d, Mean C_d of previous week
Prediction methods under multiple C_d per day estimation	Last C_d of previous day, Mean C_d of previous day, Mean C_d of previous week, Polynomial fit of previous week C_d,
Validation	GPS state vector data

Table 2.3: Settings used for orbit determination and prediction. (These conditions are applicable throughout this report unless stated otherwise.)

is taken as the estimated C_d for that day. The smaller the value of PM, the closer is the predicted C_d to the estimated C_d which in turn leads to better orbit prediction. The application of this prediction metric is discussed in Chapter 4.

2.4 Software package information

The following software applications were considered for developing orbit determination and prediction algorithms in this thesis: OREkit (ORbit Extrapolation kit) [Bernard et al., 2015], GEODYN II (Orbital and Geodetic Parameter Estimation program) [Pavlis et al., 1998, 2006] and TUDAT (TUDelft Astrodynamics Toolbox) [Kumar et al., 2012]. Since the use of OREkit required expertise in Java which was not familiar to the author, the option of using OREkit for this thesis was ruled out. Since GEODYN II is not open source, it would restrict the application of developed algorithms in commercial enterprises like Qinetiq Space. Hence, it was decided to use TUDAT for this thesis. Moreover, the author was familiar with the framework of TUDAT which was made open source before the start of the thesis. The TUDelft Astrodynamics Toolbox (TUDAT), developed and maintained by the staff and students of the Astrodynamics and Space missions branch of TUDelft, is a powerful set of C++ libraries used for astrodynamics and space research. TUDAT includes a range of libraries, all the way from gravity models to numerical integrators and other mathematical tools which are combined into a simulator framework that can be used for orbit computations. The following modules of TUDAT are used in developing orbit determination and prediction algorithms.

Environment set up: This module creates the main and perturbing bodies in whose gravity field a satellite describes its orbit.

Vehicle creation: This module defines the properties of the satellite such as its mass, the behaviour of aerodynamic and radiation pressure coefficients.

Acceleration models set up: This module defines the main and perturbing accelerations acting on the satellite such as the spherical harmonics of Earth's gravity, solid Earth tides, the third body perturbations, the aerodynamic and radiation pressure accelerations.

Propagation settings: This module defines the list of bodies and the origins with respect to which these bodies are to be propagated, the initial Cartesian state to be used and the termination conditions for propagation.

Estimation settings: This module defines the position and velocity observables of the satellite with respect to Earth along with their standard deviations and the parameter estimation vector for each estimation arc. It provides the stopping criterion for the least squares estimation process and stores the results in a convenient file format.

These modules were customized to work with real data. Based on the request to the software developer, features were created to include velocity observable and to estimate multiple drag scale factors per estimation arc. The orbit determination and prediction algorithms developed were validated using the highly precise ephemeris of the GRACE-A satellite. MATLAB (MATrix LABoratory) software was used to post-process the results of orbit determination and prediction.

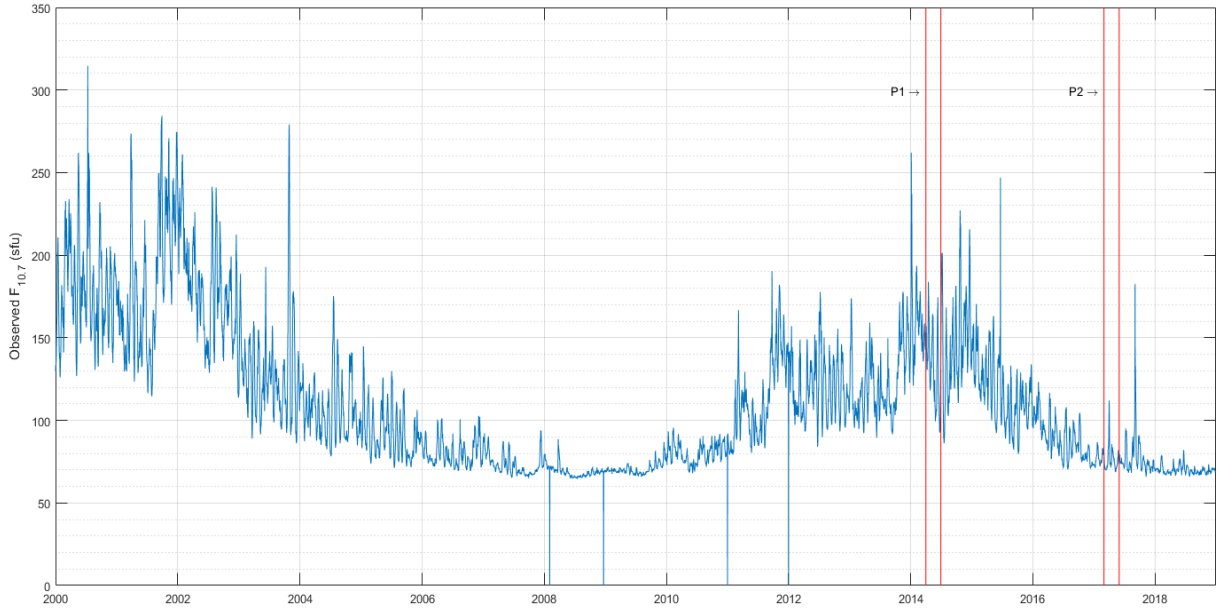

Figure 2.3: Chosen periods for orbit estimation and prediction. P1 = April - June, 2014 and P2 = March - May, 2017 [Source: `http://celestrak.com/SpaceData/`]

2.5 Selection of periods for orbit estimation and prediction

The orbit estimation and prediction schemes/methods described in Sections 2.2.2 and 2.3 are applied to two different periods of solar activity [Vallado, 2001] for both satellites. These two periods of different atmospheric density conditions can be used to evaluate the drag force modelling used in the estimation and prediction schemes. Figure 2.3 shows the variation of the observed $F_{10.7}$ since the year 2000. Based on the avialability of GPS state vector data of GRACE-A and PROBA-V, the following periods are chosen for data processing: April to June, 2014 (91 days) and March to May, 2017 (92 days). These are indicated by P1 and P2 in Figure 2.3. P1 and P2 are referred to as the chosen solar maximum and chosen solar minimum respectively, in this thesis. P2 is chosen such that the solar activity is minimum as well as the altitude of GRACE-A, which was nearing its end of life, is high enough to make reasonably accurate orbit estimation and prediction analysis. Mean value of $F_{10.7}$ during P1 is 132.20 sfu and during P2 is around 76.31 sfu. The mean altitude of the GRACE-A during P1 was 415.56 km and during P2 was 333.03 km. This difference in altitude counters the impact of minimum solar activity on the drag signal of GRACE-A.

It was explained in Section 1.3 that this thesis involves precise orbit determination and prediction for days without orbit manoeuvres. For GRACE-A, the sequence of events file available at `ftp://isdcftp.gfz-potsdam.de/grace/DOCUMENTS/TECHNICAL_NOTES/` was used to find and remove the dates with orbit manoeuvres. Though PROBA-V has no manoeuvres, there are certain dates in which its state vector data has gaps that are detrimental to the orbit determination process. These gaps are possibly due to errors in telemetry downlink. These dates are identified and removed by manual processing. Besides these dates, there are a few other days without any manoeuvres or gaps that produced huge position and velocity errors (i.e. outliers) during orbit determination and

S.No.	Dates skipped	Problematic satellite	Data gap duration	No. of orbits missed	Included in orbit prediction
1	April 24	GRACE-A	None. CM calibration during the day.	None.	No.
2	April 18	PROBA-V	None. Results in huge outliers.	None.	No.
3	May 27	PROBA-V	02:18 to 09:38 hrs	4.20	No.
4	May 30	PROBA-V	08:22 to 10:36 hrs	1.27	Yes.
5	June 11	PROBA-V	06:57 to 10:35 hrs	2.08	No.

Table 2.4: Analysis of skipped dates for orbit estimation during April - June, 2014 (mean observed $F_{10.7} = 132.20$ sfu)

prediction processes. These were also removed to prevent skewing of the results. The overview of all days that are excluded is listed in the column 'Dates skipped' in Table 2.4 for chosen solar maximum (P1) and in Table 2.5 for chosen solar minimum (P2).

Since orbit prediction requires initial state and C_d from the estimation output of previous day (Section 2.3), all the days subsequent to the 'Dates skipped' in Tables 2.4 and 2.5 are excluded from prediction. This also applies to the first days of P1 (April 1, 2014) and P2 (March 1, 2017). The days with data gaps that are not suitable for orbit determination are analyzed to find the number of orbits missed due to the gap. Mathematically,

$$\text{No. of orbits missed} = \frac{\text{Data gap duration (min)}}{\text{Corresponding satellite orbit period (min)}} \tag{2.30}$$

The orbit period of the GRACE-A during P2 is 91.23 minutes. The orbit period of the PROBA-V during P1 is 104.88 minutes and during P2 is 104.83 minutes. If the number of orbits missed is greater than 2 which equals a data gap of more than 3 hours, then the corresponding date is excluded from orbit prediction process. Results of this analysis are presented in Tables 2.4 and 2.5. Additionally, for orbit prediction methods that involve the estimated C_d of the previous week (see Section 2.3), the first seven days of P1 (April 1 - 7, 2014) and P2 (March 1 - 7, 2017) are excluded from prediction.

S.No.	Dates skipped	Problematic satellite	Data gap duration	No. of orbits missed	Included in orbit prediction
1	March 13	GRACE-A	02:30 to 09:31 hrs	4.61	No.
2	March 17	PROBA-V	03:43 to 05:25 hrs	0.97	Yes.
3	March 28	PROBA-V	19:38 to 21:57 hrs	1.32	Yes.
4	April 13	PROBA-V	03:46 to 06:05 hrs	1.32	Yes.
5	April 18	PROBA-V	00:21 to 06:21 hrs	3.43	No.
6	May 12	PROBA-V	04:40 to 09:51 hrs	2.96	No.
7	May 22	PROBA-V	12:12 to 20:55 hrs	5.00	No.
8	May 16	PROBA-V	None. Presence of a few enormous fluctuations.	None.	No. It results in large position and velocity errors.

Table 2.5: Analysis of skipped dates for orbit estimation during March - May, 2017 (mean observed $F_{10.7}$ = 76.31 sfu)

Chapter 3

Estimation and prediction with one drag scale factor per day

This chapter focuses on the results and their interpretation for the case of orbit determination in which only one drag scale factor (C_d) is estimated per day. Orbit prediction is then carried out using different prediction methods pertaining to one C_d estimation per day as defined in Section 2.3. Sections 3.1 and 3.2 provide the estimation and prediction results, respectively, for both satellites (GRACE-A and PROBA-V) during the chosen solar maximum, P1 and solar minimum, P2.

3.1 Results and interpretation of orbit estimation

Orbit determination was carried out for GRACE-A and PROBA-V satellites during the selected periods P1 and P2 with the estimation of one drag scale factor (C_d) per day. As explained in Section 2.5, certain days were skipped for estimation. For each estimation arc (i.e. one day), the initial state vector and one C_d were estimated, yielding resulting trajectory as the output. This process was repeated for successive estimation arcs throughout P1 and P2. The validation was done as explained in Section 2.2 and the statistics of estimation for both periods are summarized in the Table 3.1 with the dominating error highlighted in red colour. The table shows, for GRACE-A, during both periods, the RMS of position error in the along-track direction is larger than the error in other directions. This can be interpreted as the mismodelling of drag force in the along-track direction, which is not sufficiently absorbed by estimating one C_d per day. The error in the along-track direction is even larger during March - May, 2017 due to the low altitude of GRACE-A (mean altitude = 333.03 km) than the period April - June, 2014 (mean altitude = 415.56 km). The difference in altitude results in a higher atmospheric density, which in turn leads to larger drag force in the along-track direction. This increase in the density is not properly represented in the model, leading to larger along-track errors. The table also shows that, for PROBA-V the RMS of position error in radial direction is higher than the error in other directions. This can be explained by the fact that the effect of the Vertical Dilution of Precision (VDOP) in the GPS state vector data is larger than the effect of drag force at the altitude of PROBA-V. This is because almost all of the GPS signals received by a LEO satellite come from above (i.e. radially outward) the satellite altitude [Langley, 1999]. Though this is also true for the state vector data of GRACE-A,

Period	**Satellite Name**	**RMS of position error** (m)			**RMS of velocity error** (m/s)			**3D Position RMS** (m)	**Mean estimated** C_d
		Radial	Along-track	Cross-track	Radial	Along-track	Cross-track		
April to June, 2014	GRACE-A	0.92	5.83	0.59	0.0064	0.0009	0.0006	5.93	3.10 ± 0.45
	PROBA-V	3.09	1.35	1.32	0.1128	0.0619	0.0391	3.63	1.85 ± 0.32
March to May, 2017	GRACE - A	1.99	18.54	1.05	0.0210	0.0018	0.0012	18.68	2.53 ± 0.47
	PROBA - V	1.99	0.90	0.82	0.0305	0.0216	0.0114	2.34	1.30 ± 0.28

Table 3.1: Results of estimation with 1 C_d per day.

the lower altitude of GRACE-A compared to PROBA-V results in a larger drag force, which in turn results in a larger RMS of position error in the along-track direction.

The orbit estimation position errors of both satellites are shown in Figures 3.1 and 3.2 along with solar and geomagnetic activity indices for the periods P1 and P2, respectively. The gaps seen in the plots are due to the missing days that were skipped for the estimation. For the period P1, the position error of GRACE-A shows a very low positive correlation of 3 % and 4 % with the observed $F_{10.7}$ and the daily A_p, respectively. For the same period, the position error of PROBA-V shows a very low negative correlation of 4 % and 2 % with the observed $F_{10.7}$ and the daily A_p, respectively. The position errors of PROBA-V indicate the presence of more noise compared to the results of GRACE-A. This is true because, inherently the state vector data of PROBA-V is not as accurate as that of GRACE-A (Table 2.1) and this inaccuracy is propagated in the estimation process according to the law of propagation of error [Langley, 1999]. Another factor that can contribute to the noise is the GPS state vector data density of PROBA-V which is low compared to that of GRACE-A (Table 2.1). This results in less number of observations per estimation arc which also affects the quality of the estimation. Besides, there are some outliers in the position error plot of PROBA-V such as during May 20 and June 22, 2014. These are probably due to single event upsets (SEUs) such as striking of a sensitive node in a micro-electronic device on-board by an ionizing particle, which occurs at the altitude of PROBA-V. These aspects can also be observed in the orbit estimation position errors of PROBA-V during March - May, 2017 (Figure 3.2a).

During the period P2, the position error of GRACE-A shows a very low correlation of 1 % and 6 % with the observed $F_{10.7}$ and the daily A_p, respectively. For the same period, the position error of PROBA-V shows a -1 % and 1 % correlation with the observed $F_{10.7}$ and the daily A_p, respectively. A small 'bulge' in the position error of PROBA-V can be observed during April 8-10, 2017. This is more likely due to a problem with the state vector data of the satellite than the possibility of short-term disturbances in the atmosphere, which are not represented in the density model. The overall along-track error of GRACE-A is larger compared to that observed during P1 due to an altitude difference of nearly 80 km for GRACE-A during P2. This altitude difference produces changes in the drag force which are not properly represented in the model. This difference is not observed in the position error of PROBA-V as the altitude hardly changes by 600 m between P1 and P2. The largest peak in the along-track error of GRACE-A occurs on May 2, 2017 when there is no appreciable solar and geomagnetic activity. Upon checking the sequence of events file, it was found that an attitude control manoeuvre had been executed on that day. Since the magnitude of the manoeuvre was not so large, the estimation process was able to characterize the manoeuvre. The correlations mentioned above indicate that during both the periods, the position errors of neither satellites show

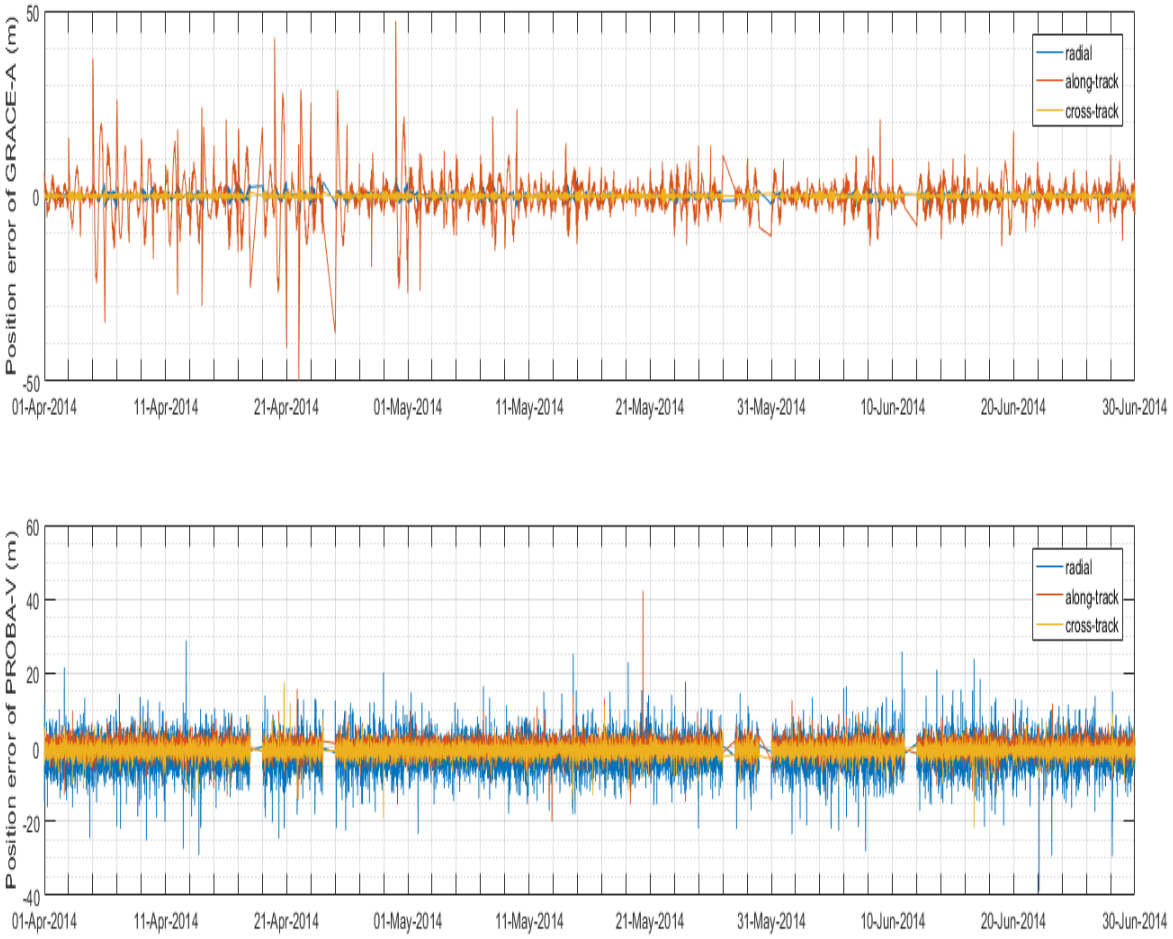

(a) Orbit estimation (1 C_d per day) position errors for GRACE-A (top) and PROBA-V (bottom) during April - June, 2014.

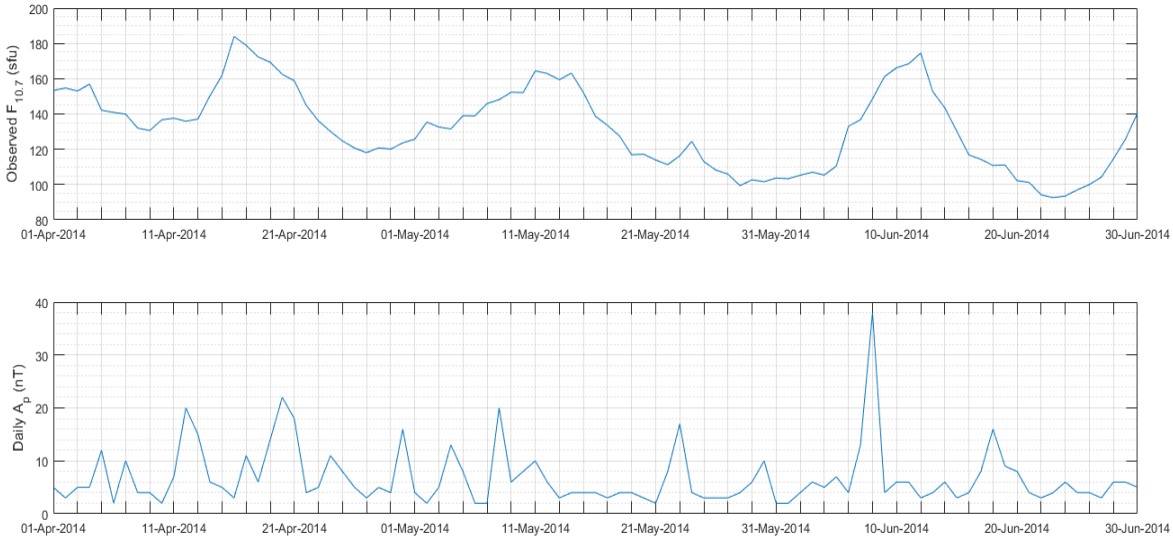

(b) Variation of observed $F_{10.7}$ (top) and daily A_p (bottom) during April - June, 2014.

Figure 3.1: Comparison of the orbit estimation (1 C_d per day) position errors of GRACE-A and PROBA-V with solar and geomagnetic activity indices during April - June, 2014.

(a) Orbit estimation (1 C_d per day) position errors for GRACE-A (top) and PROBA-V (bottom) during March - May, 2017.

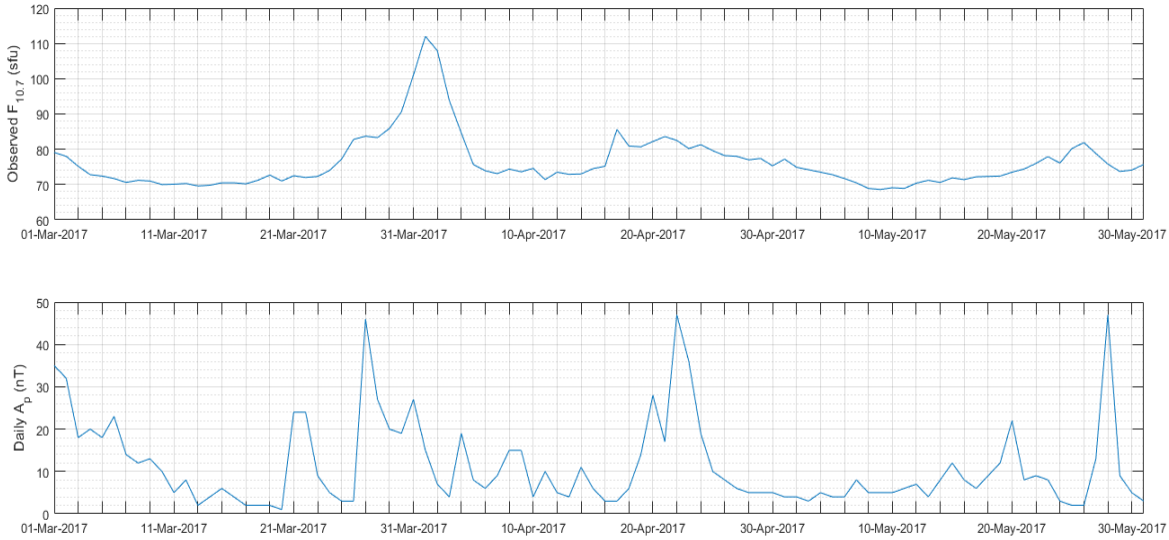

(b) Variation of observed $F_{10.7}$ (top) and daily A_p (bottom) during March - May, 2017.

Figure 3.2: Comparison of the orbit estimation (1 C_d per day) position errors of GRACE-A and PROBA-V with solar and geomagnetic activity indices during March - May, 2017.

a correlation of more than 10 % with the observed $F_{10.7}$ and the daily A_p. This might indicate that the position errors observed in Figures 3.1a and 3.2a are due to the estimation of just one C_d per day, which is a mismodelling of the drag force experienced by the satellites in a single day. The effect of the unmodelled forces in this thesis such as the ocean tides also contribute to the overall position errors observed in these figures.

The estimated drag scale factors of both satellites for both periods are shown along with the corresponding plots of solar and geomagnetic activity indices in Figure 3.3. The estimated drag scale factors are satellite dependent. From the Figure 3.3, it can be seen that the estimated drag scale factors (C_d) of the satellites show very good correlation among themselves. The correlation coefficient between the drag scale factors of GRACE-A & PROBA-V during April - June, 2014 comes to around 0.94. This value drops to 0.74 during March - May, 2017. Higher correlation during the chosen solar maximum (April - June, 2014) can be attributed to the strong drag signal experienced by both satellites compared to the chosen solar minimum (March - May, 2017). An interesting point to be noted is the change in the mean value of the estimated C_d between the periods P1 and P2 (Table 3.1). The C_d of GRACE-A changes from 3.10 to 2.53 and that of PROBA-V changes from 1.85 to 1.30. Since the satellite specific parameters such as the shape and surface properties remain the same between P1 and P2, a change in the C_d indicates that the variation of density due to solar activity has not been adequately incorporated in the density model. This is discussed further in the multiple C_d estimation (Chapter 4). During the period P1, the estimated C_d of GRACE-A and PROBA-V show a correlation of 33 % and 27 %, respectively with the observed $F_{10.7}$ and a correlation of 10 % with the daily A_p. During the period P2, the estimated C_d of GRACE-A and PROBA-V show a correlation of 48 % and 49 %, respectively with the daily A_p and a correlation of 3 % with the observed $F_{10.7}$. Hence, correlations of more than 25 % are observed between the estimated C_d and the observed $F_{10.7}$ during P1 and between the estimated C_d and the daily A_p during P2. These correlations support the speculation that the estimation of just one C_d per day is not good enough to accurately model the drag force experienced by the satellites in a single day. It is noted here that the estimated C_d can't be used as a pure scaling factor to study the density variation. Rather, it can be used for a more general purpose such as orbit prediction for that particular satellite.

The NRLMSISE-00 atmosphere model has a separate subroutine (GTD7D) which computes the effective mass density as a summation of thermospheric mass density and the mass density of the anomalous oxygen component. This component accounts for the contribution of non-thermospheric species such as the hot atomic oxygen and atomic oxygen ions (O^+) to the drag near the exobase altitudes. These species result from the photochemical processes in the upper atmosphere [Picone et al., 2002]. In an attempt to improve the results of orbit estimation, this subroutine was used for the orbit estimation of GRACE-A and PROBA-V with 1 C_d per day resolution during the chosen solar maximum and minimum. Results of this estimation are given in Table 3.2. The 3D RMS of the difference between the estimated position when including the anomalous oxygen effect and when not including the anomalous oxygen effect is provided in Table 3.3. It can be seen that for both periods and for both satellites, the anomalous oxygen effect on the estimated position error is not very significant. Moreover, the computation time increased by more than two fold, which reduces the efficiency of orbit determination. Hence, the subroutine GTD7D is not considered for further analysis.

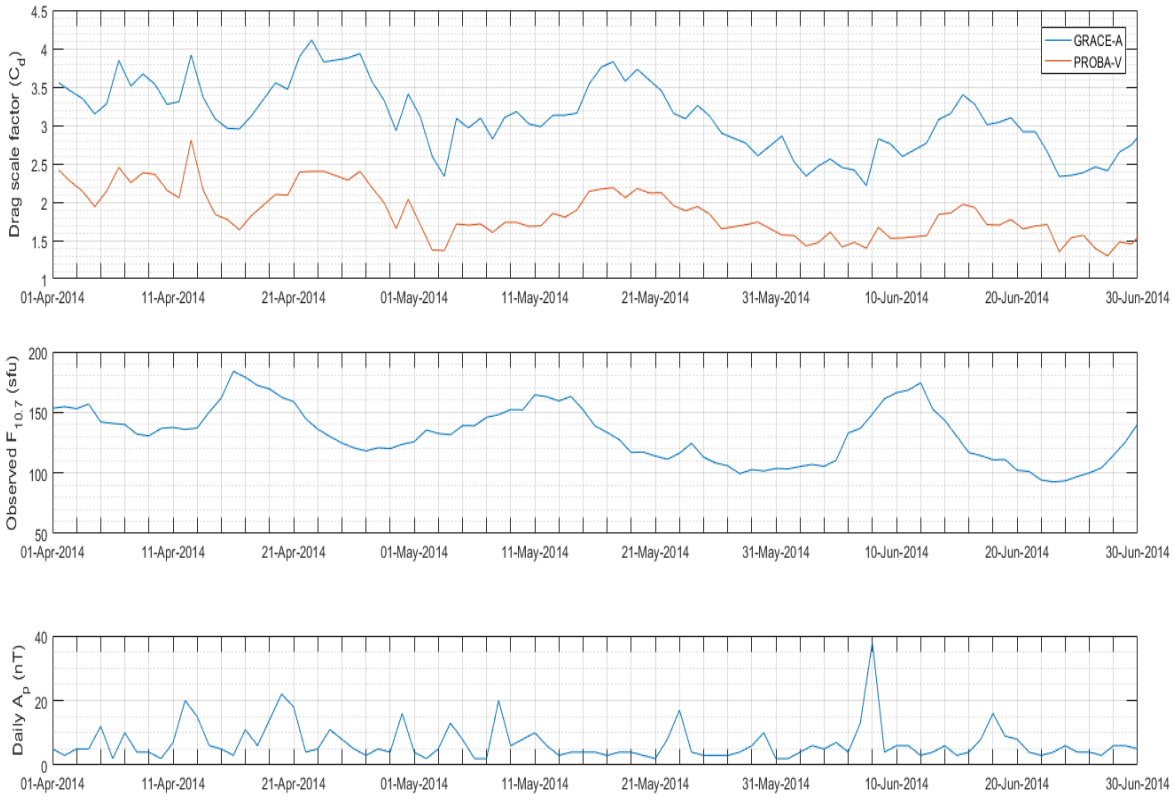

(a)

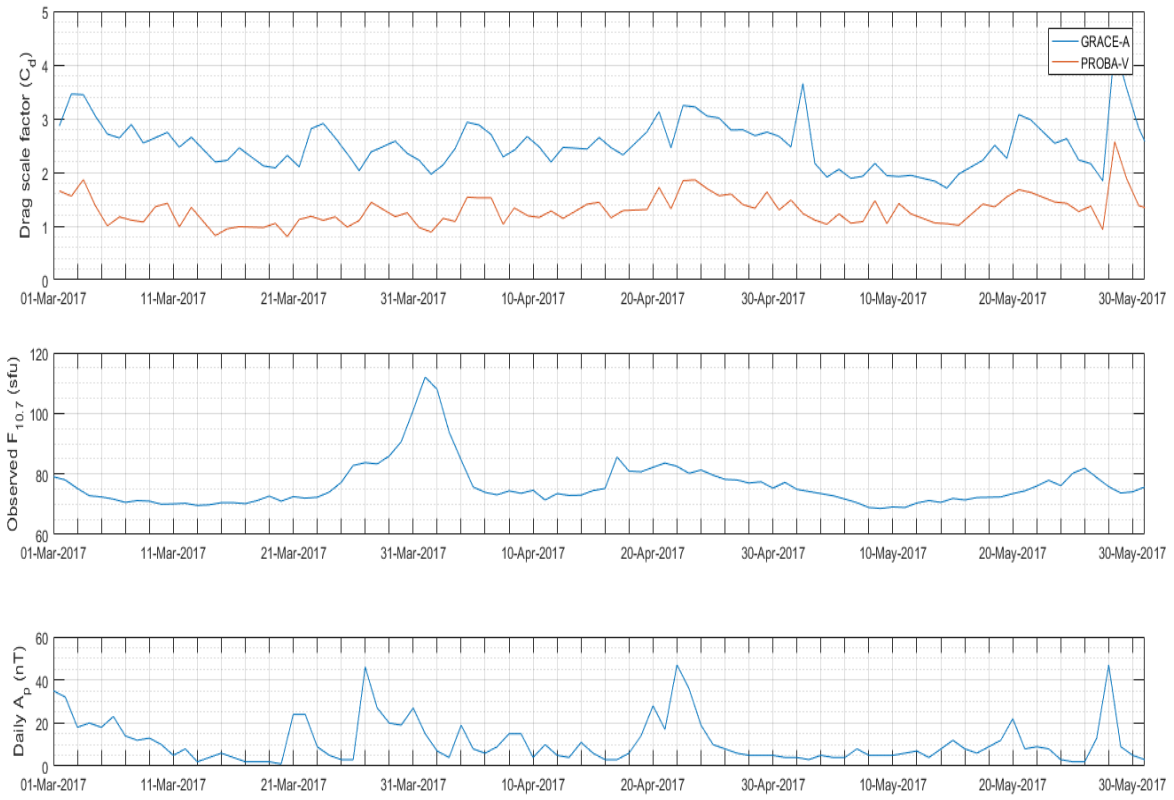

(b)

Figure 3.3: Comparison of the estimated drag scale factors (1 C_d per day) of GRACE-A and PROBA-V with solar and geomagnetic activity indices during April - June, 2014 and March - May, 2017.

Period	Satellite Name	RMS of position error (m)			RMS of velocity error (m/s)			3D Position RMS (m)	Mean estimated C_d
		Radial	Along-track	Cross-track	Radial	Along-track	Cross-track		
April to June, 2014	GRACE-A	0.92	5.83	0.59	0.0064	0.0009	0.0006	5.93	3.10 ± 0.45
	PROBA-V	3.09	1.35	1.32	0.1128	0.0619	0.0391	3.63	1.79 ± 0.33
March to May, 2017	GRACE-A	1.99	18.54	1.05	0.0210	0.0018	0.0012	18.68	2.53 ± 0.47
	PROBA-V	1.99	0.90	0.82	0.0305	0.0216	0.0114	2.34	1.24 ± 0.25

Table 3.2: Results of estimation with 1 C_d per day including the effect of anomalous oxygen (AO).

Period	Satellite name	3D RMS of Δ Est.position (m)
April to June, 2014	GRACE-A	0.0024
	PROBA-V	0.0070
March to May, 2017	GRACE-A	0.0050
	PROBA-V	0.0027

Table 3.3: Impact of anomalous oxygen.

3.2 Results and interpretation of orbit prediction

Orbit prediction was carried out for both satellites during the selected periods P1 and P2 using the outputs of the estimation process. All the three prediction methods that are listed in the category of estimation using single C_d per day (Section 2.3) were performed. Figure 3.4 shows the comparison of the estimated and predicted drag scale factors during periods P1 and P2 for both satellites. From Figure 3.4a, it can be seen that for both satellites the drag scale factor obtained using the C_d of previous day closely follows the estimated C_d. The prediction method that obtains the drag scale factor by fitting a third order polynomial to the previous week C_d appears to have large variance in its output. This shows that capturing the complex dynamics of C_d variation using polynomials is a crude approximation. Similar trends are observed during the period P2 for both satellites (Figure 3.4b). Worse orbit prediction performance is expected when the C_d is less well predicted.

As explained in Section 2.5, certain days were skipped for prediction. For each prediction arc (i.e. one day), the last state vector from the resulting trajectory of the previous day estimation was used as the initial state. Depending on the prediction method, the C_d for the prediction arc was obtained from the estimated parameters. This process was repeated for successive prediction arcs throughout P1 and P2 to obtain propagated trajectories which were validated using the GPS state vector data. Statistics of prediction for both periods are summarized in Tables 3.4 and 3.5 for GRACE-A and PROBA-V respectively. For a given prediction (i.e. propagation) arc, the error in the predicted orbit increases steadily as the time progresses and reaches a maximum value at the end of the arc. This value, which can be positive or negative, is called the maximum position error of that arc. Throughout the entire selected period, a mean is computed for the absolute values of the maximum position error of all the prediction arcs. This is called the mean of maximum position error. Best and worst prediction methods are chosen on the basis of the mean of maximum position error in the along-track direction. Best prediction method

Period	**Prediction method**	**Mean of maximum position error** (m)			**Mean of maximum velocity error** (m/s)			**3D RMS of position error** (m)	
		Radial	Along-track	Cross-track	Radial	Along-track	Cross-track	Predicted orbit	Estimated orbit
April to June, 2014	C_d of previous day	8.00	340.39	2.74	0.3810	0.0068	0.0031	209.16	5.93
	polynomial fit of previous week C_d	12.24	611.05	2.77	0.6863	0.0095	0.0031	367.45	5.93
	mean C_d of previous week	9.39	410.30	2.78	0.4606	0.0077	0.0032	248.18	5.93
March to May, 2017	C_d of previous day	17.24	966.98	5.28	1.1077	0.0143	0.0061	722.83	18.68
	polynomial fit of previous week C_d	28.21	1634.16	5.32	1.8740	0.0213	0.0062	997.00	18.68
	mean C_d of previous week	17.70	1031.15	5.30	1.1810	0.0140	0.0061	665.68	18.68

Table 3.4: Results of orbit prediction for GRACE-A using different C_d prediction schemes.

Period	**Prediction method**	**Mean of maximum position error** (m)			**Mean of maximum velocity error** (m/s)			**3D RMS of position error** (m)	
		Radial	Along-track	Cross-track	Radial	Along-track	Cross-track	Predicted orbit	Estimated orbit
April to June, 2014	C_d of previous day	18.42	13.30	7.98	2.3680	1.1219	0.8548	6.10	3.63
	Polynomial fit of previous week C_d	18.34	15.53	7.98	2.3356	1.1251	0.8466	7.39	3.63
	Mean C_d of previous week	18.35	13.96	7.98	2.3359	1.1251	0.8466	6.34	3.63
March to May, 2017	C_d of previous day	9.43	8.64	3.60	0.2062	0.0920	0.0638	4.26	2.34
	Polynomial fit of previous week C_d	9.46	9.03	3.55	0.2017	0.0905	0.0637	4.50	2.34
	Mean C_d of previous week	9.46	8.48	3.55	0.2019	0.0905	0.0637	4.22	2.34

Table 3.5: Results of orbit prediction for PROBA-V using different C_d prediction schemes.

is indicated by green colour and the worst method by red colour in Tables 3.4 and 3.5.

For GRACE-A, the Table 3.4 shows that the method of using the C_d of previous day for prediction turns out to be the best prediction method during both periods. The prediction error during March - May, 2017 is much larger than the error during other period due to the difference in altitude as is the case for the estimation error. For both periods, prediction using a polynomial fit of the previous week C_d turns out to be the worst prediction method. During March to May, 2017, it can be seen that the prediction using the C_d of previous day gives a mean maximum along-track position error of 967 m, which is 64 m less than the corresponding error for prediction using the C_d of the previous week. However, it is interesting to note that, for the same period, prediction using mean C_d of previous week gives a value of 666 m for 3D RMS of the position error of predicted orbit, which is 57 m less than the corresponding error for prediction using the mean C_d of the previous day. Jäggi et al. [2011] predicted the orbit of GOCE satellite during 2009 when it descended (not a drag-free flight) to its final orbital altitude, by estimating piece-wise constant accelerations for non-gravitational forces. The altitude of GOCE during that period was between 275 and 265 km. For a prediction arc length of 24 hours, it resulted in a mean along-track error of 1089 m. Considering the difference in altitude, the results obtained for GRACE-A (mean along-track error during March - May, 2017: 967 m) using the best prediction method (C_d of previous day) are not as good as the results of Jäggi et al. [2011]. This comparison will be further discussed in Section 4.2. However, the orbit determination that precedes the prediction strategy used

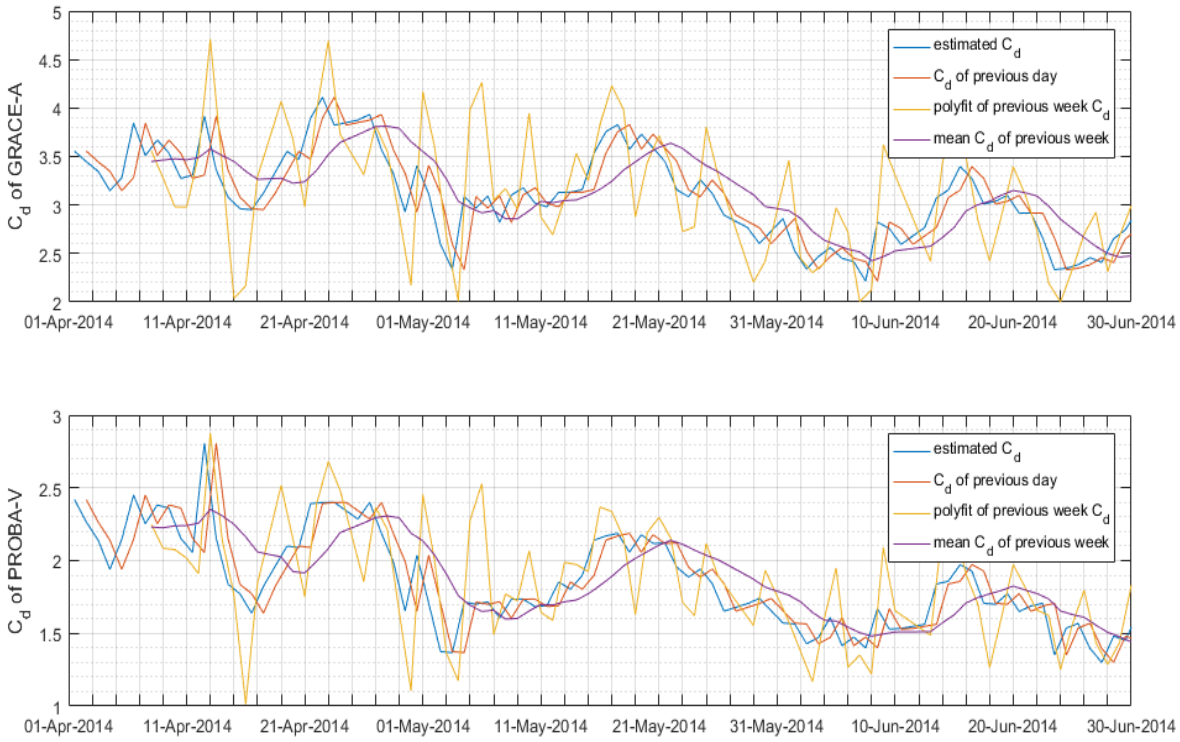

(a)

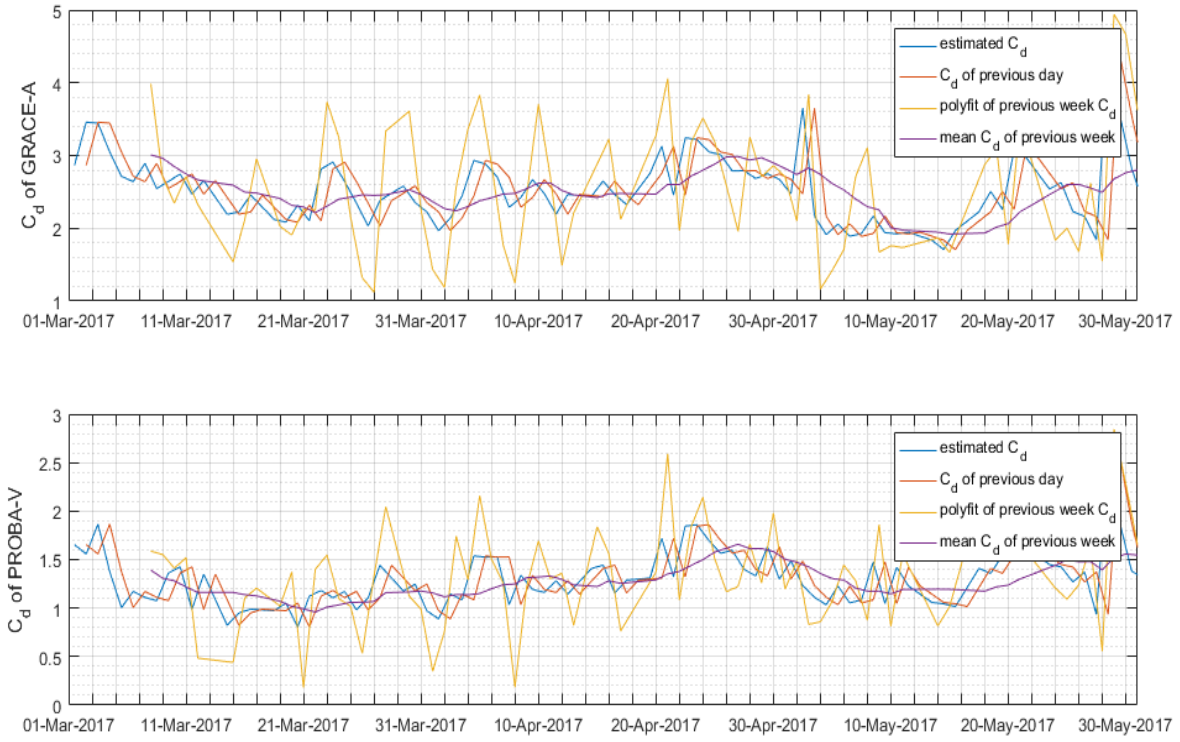

(b)

Figure 3.4: Comparison of the estimated drag scale factors (1 C_d per day) of GRACE-A and PROBA-V with different prediction methods during April - June, 2014 (Figure 3.4a) and March - May, 2017 (Figure 3.4b).

by Jäggi et al. [2011] involves estimation of 240 piece-wise constant accelerations besides estimating the initial state and 3 empirical accelerations for a single day. This imposes a huge computational load in comparison to the orbit determination strategy used in this thesis. The problem of computational load becomes significant when considering the on-board orbit determination and prediction for autonomous maintenance of satellite formation. This is treated in more detail in the Chapter 6. The orbit determination strategy of this thesis has a different data rate and accuracy of observations than the orbit determination employed by Jäggi et al. [2011]. These factors also contribute to the difference in the orbit prediction accuracy. It should be noted that the lowest along-track prediction error using the C_d of previous day, 340.4 m, does not satisfy the requirement of 125 m mentioned in Section 1.3. Hence, to reduce the prediction error of GRACE-A, estimation and prediction using multiple drag scale factors per day are required.

For PROBA-V, the prediction errors are much smaller compared to the GRACE-A during both the periods P1 and P2. The Table 3.5 shows that during April - June, 2014 the prediction method using the C_d of the previous day turns out to be the best method, while for the other period using the mean C_d of the previous week turns out to be the best prediction method. This may be due to the low solar activity during March - May, 2017 which causes moderate density variations at PROBA-V altitude that can be best represented by an average value of the drag scale factor per week. The prediction error is larger during P1 than P2 due to increased drag from higher density which results from higher solar activity. It can also be observed that the mean of maximum position error in the radial direction is larger compared to other directions for both periods. Since orbit prediction is based on the results of orbit estimation which, for PROBA-V, showed higher RMS in radial direction (Table 3.1) due to larger VDOP effect, the same is reflected in the prediction results as well. During March - May, 2017, the prediction based on the mean C_d of previous week provides slightly better results (2.05 % more accurate) than the prediction based on the C_d of the previous day. However, to compute the mean C_d of previous week, estimation has to be done for the previous week which results in more computational load compared to obtaining the estimated C_d of previous day. Hence, from a computation point of view, it is recommended to choose the prediction method that uses the estimated C_d of the previous day.

The orbit prediction position errors for the best and the worst prediction methods are shown in Figures 3.5 and 3.6 for periods P1 and P2 respectively. There are gaps in the plots which are due to the days that were skipped for prediction and due to the prediction method such as using a polynomial fit of the previous week C_d. From Figures 3.5a and 3.5b, it can be seen that for both satellites, the best prediction method gives along-track errors of less magnitude than the worst prediction method. This trend can be observed in Figure 3.6. For PROBA-V, there are quite a number of days for which the along-track error is larger than the radial error. These are the days when the effect of drag is larger than the VDOP effect. Similar to the estimation, results of the orbit prediction for both satellites show more number of large position errors during April 2014. For the best prediction method, during P1, the orbit prediction position error of GRACE-A and PROBA-V show low correlation of 12 % and -11 %, respectively with the daily A_p index. The outliers observed in the estimation output of PROBA-V are also reflected in both the best and worst case prediction results.

(a) Position errors of GRACE-A (top) and PROBA-V (bottom) resulting from orbit prediction using C_d of previous day, during April - June, 2014 - best prediction method.

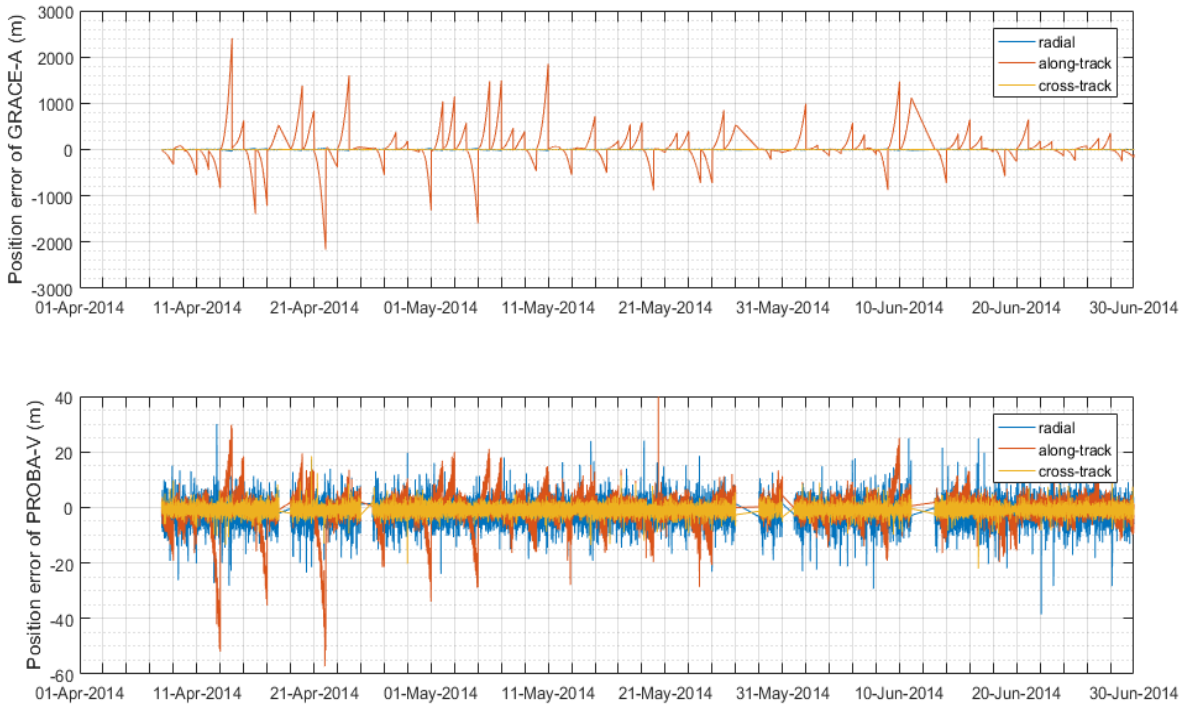

(b) Position errors of GRACE-A (top) and PROBA-V (bottom) resulting from orbit prediction using polynomial fit of previous week C_d, during April - June, 2014 - worst prediction method.

Figure 3.5: Orbit prediction position errors of GRACE-A and PROBA-V during April - June, 2014 - best case and worst case scenarios.

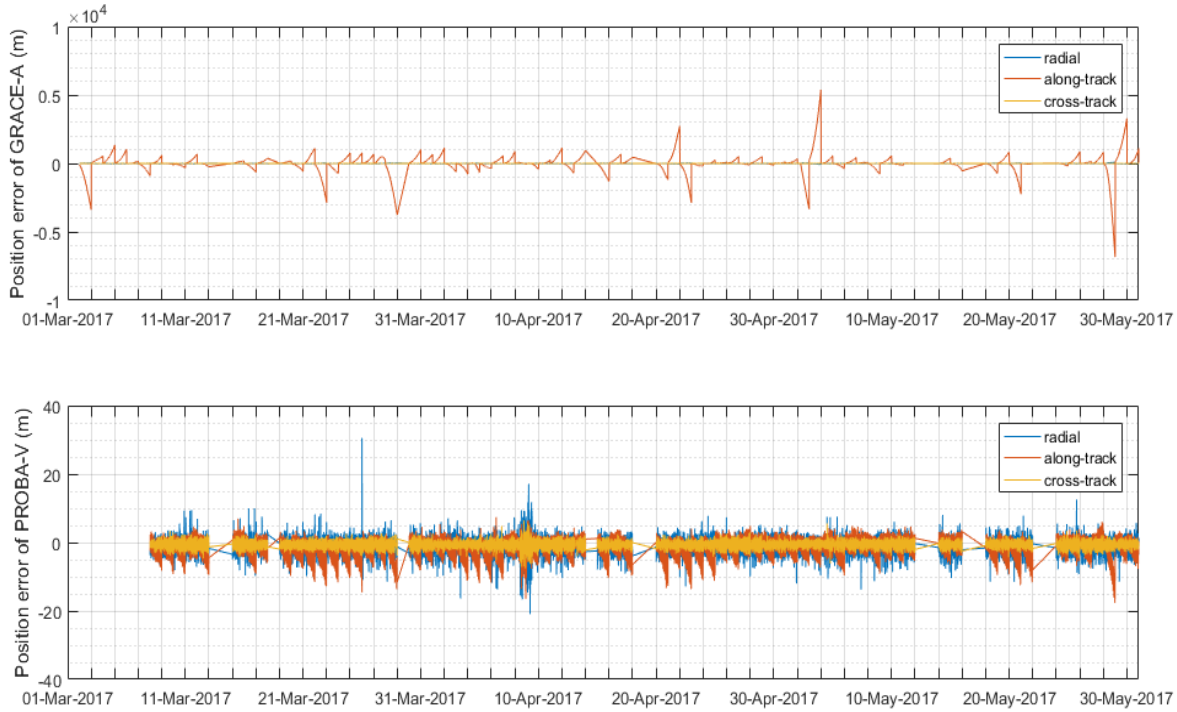

(a) Position errors of GRACE-A (top) and PROBA-V (bottom) from orbit prediction using C_d of previous day for GRACE-A and mean C_d of previous week, during March - May, 2017 - best prediction method.

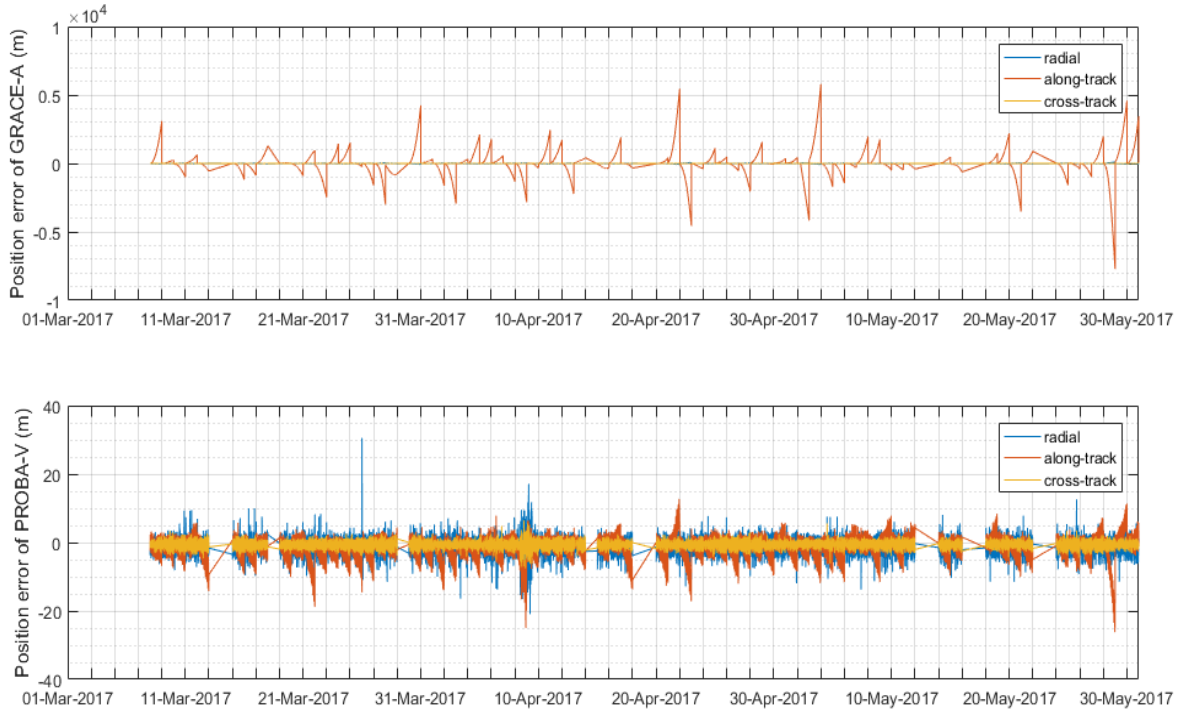

(b) Position errors of GRACE-A (top) and PROBA-V (bottom) from orbit prediction using polynomial fit of previous week C_d, during March - May, 2017 - worst prediction method.

Figure 3.6: Orbit prediction position errors of GRACE-A and PROBA-V during March - May, 2017 - best case and worst case scenario.

The mean maximum position error (3D) of the predicted orbit is computed as,

$$\begin{aligned}(\text{Mean max. position error})_{\text{3D,pred.}} \;=\; &((\text{mean max. error})^2{}_{\text{rad, pred}} + \\ &(\text{mean max. error})^2{}_{\text{along, pred}} + (\text{mean max. error})^2{}_{\text{cross, pred}})^{\frac{1}{2}} \end{aligned} \quad (3.1)$$

When using the estimated C_d of previous day for orbit prediction during April to June, 2014, the mean maximum position error (3D) of PROBA-V becomes 24.08 m. When using the estimated C_d of previous day for orbit prediction during March to May, 2017, the mean maximum position error (3D) of PROBA-V becomes 13.28 m. Hence, for PROBA-V, it is sufficient to estimate the orbit using only one drag scale factor per day and predict the orbit using the estimated C_d of the previous day to achieve the accuracy requirement of 125 m (Section 1.3). Nevertheless, estimation of multiple drag scale factors for PROBA-V can still be done to see if it offers any further reduction of the 3D RMS of the position error. However, for GRACE-A, estimation and prediction with multiple drag scale factors per day should be further investigated. It is expected that this can further improve the prediction accuracy of GRACE-A in order to reach the 125 m accuracy requirement.

Chapter 4

Estimation and prediction with multiple drag scale factors per day

It was pointed out in Chapter 3 that the estimation of multiple drag scale factors per day will likely improve the orbit prediction of GRACE-A. This is because the drag force is predominantly a 1 cycle-per-revolution (CPR) force as both the satellites pass through the day side and the night side of the Earth in one orbit. The satellites also encounter density variations due to the difference in altitude between the equatorial and polar regions. Due to these changes in density, there can be variations in the gas-surface interaction at the surface of the satellites which can alter the drag force. Not all variations are characterized by the atmosphere model and the aerodynamic force model. To capture all these variations sufficiently, estimation of multiple drag scale factors per day is required. The information from this orbit estimation is then used in the prediction process. The results of these processes are the focus of this chapter.

Section 4.1 presents the results of estimation using multiple drag scale factors per day for both satellites. It is shown that the estimation of multiple drag scale factors does not improve the orbit accuracy of PROBA-V, and leads to unrealistic drag scale factors. Section 4.2 provides the results of prediction performed for GRACE-A using the different prediction methods under multiple C_d estimation per day as briefed in Section 2.3. The section also provides an analysis of the results to determine the best prediction method for GRACE-A for both periods P1 and P2.

4.1 Results and interpretation of orbit estimation

The procedure for estimation is similar to the one briefed in Section 3.1 except that multiple drag scale factors are estimated per day. A new feature in TUDAT, exclusively created for this purpose, was used to conduct four different estimations with four different resolutions of estimated drag scale factors: 2 C_d per day, 3 C_d per day, 4 C_d per day and 8 C_d per day. Figures 4.1 and 4.2 compare the estimated drag scale factors of both satellites under different resolutions with the solar and geomagnetic activity indices during periods P1 and P2, respectively. Figures 4.1a and 4.1b show more peaks and an increased range of variation in the estimated C_d compared to the estimation of single C_d per day shown in Chapter 3. This is more prominent for the estimation using 8 C_d per day which

results in unrealistic values for the estimated C_d of GRACE-A. Both the figures (4.1a and 4.1b) show a periodicity in the estimated C_d of GRACE-A corresponding to three solar rotations, each with a period of roughly 27 to 28 days. During P1, the estimated C_d of GRACE-A show a 32 % correlation with the observed $F_{10.7}$ for the resolution of 2 C_d per day. This correlation drops to 25 % for the resolution of 8 C_d per day. During P2, the estimated C_d of GRACE-A show a 39 % correlation with the daily A_p for the resolution of 2 C_d per day. This correlation drops to 32 % for the resolution of 8 C_d per day. The drop in correlation may be due to the increased resolution of the estimated C_d which, in part, reduces the mismodelling of the drag force experienced by GRACE-A. From Figures 4.2a and 4.2b, it can be observed that as the resolution of the estimated C_d of GRACE-A increases, the value of the outlier C_d on May 2, 2017, corresponding to the attitude control manoeuvre of GRACE-A also increases. Comparing the value of the estimated C_d obtained during the manoeuvre, using one C_d per day resolution ($C_d = 3.6$ (see Figure 3.3b)) with the corresponding value obtained using 8 C_d per day resolution ($C_d = 10$), the C_d increases by a factor of more than 2.5. This is reflected as a significant reduction of the estimation position error during the manoeuvre. Hence, an increased resolution of the estimated C_d is capable of absorbing the manoeuvre to some extent, if the magnitude of the manoeuvre is not large enough to result in failure of the estimation process. A more suitable solution would be to include the manoeuvre in the force model.

It can be seen from Figures 4.1a, 4.1b, 4.2a and 4.2b that when more than one drag scale factor is estimated per day for PROBA-V, the resulting drag scale factors are very unrealistic; negative drag scale factors can be observed for certain conditions. This is the reason for not performing the estimation of 8 C_d per day for PROBA-V. The estimated drag scale factors of PROBA-V no longer show good correlation with the estimated drag scale factors of GRACE-A, which was the case when one drag scale factor was estimated per day (Section 3.1). This is due to the weak drag force experienced by PROBA-V at its altitude which is sufficiently approximated by the estimation of one drag scale factor per day. Hence, the results of orbit estimation position errors of PROBA-V with the estimation of multiple C_d per day are not shown here.

Figures 4.3 and 4.4 compare the orbit estimation position errors of GRACE-A under different resolutions of estimated C_d with the solar and geomagnetic activity indices during periods P1 and P2, respectively. In comparison with the position errors of GRACE-A obtained using one C_d per day estimation (Figure 3.1), the position errors obtained using multiple C_d per day estimation show reduction by a factor of 2 to 3.5 (Figure 4.3). As the resolution of estimated C_d increases, the overall position error decreases. During periods of high solar and geomagnetic activity, deviations from co-rotating atmosphere model may occur. This might affect the velocity relative to the atmosphere, resulting in slightly larger position errors [Panzetta et al., 2019]. The orbit estimation position errors of GRACE-A hardly exhibit a correlation of 1 % with the solar or geomagnetic activity indices during both periods P1 and P2 for all resolutions of the estimated C_d. The most prominent feature seen in Figures 4.4a and 4.4b is the reduction in the along-track error during the manoeuvre on May 2, 2017. In comparison with the one C_d estimation per day (Figure 3.2) the along-track error reduces from 300 m to 60 m (i.e. 80 %) and accordingly the estimated C_d increases from 3.6 to 10.

Table 4.1 summarizes the results of the multiple C_d estimation of GRACE-A for all the resolutions. During April - June, 2014, compared to the RMS of along-track position error obtained from one C_d per day estimation (Table 3.1), the RMS of along-

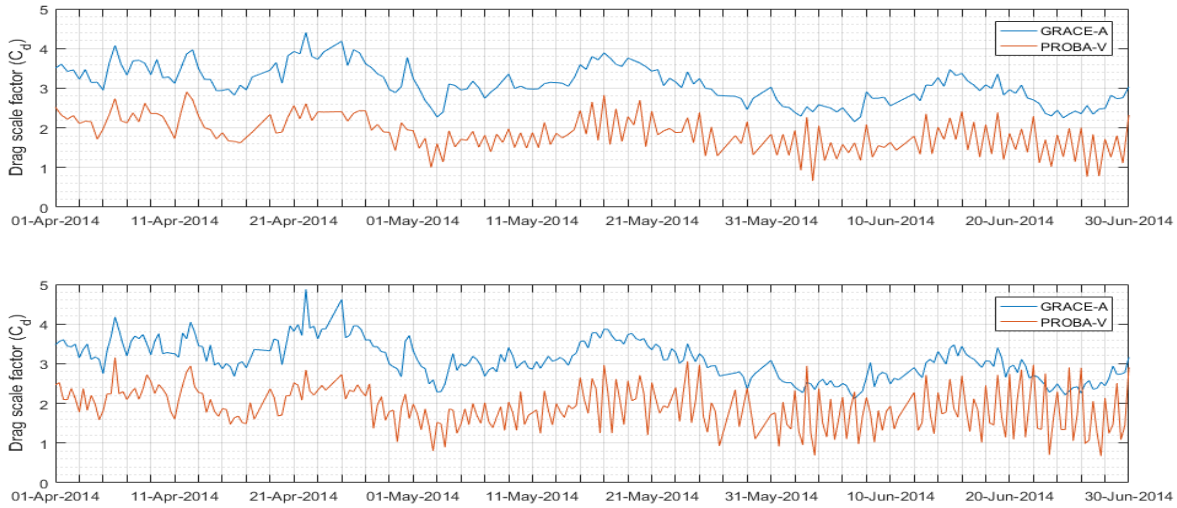

(a) Estimation of 2 C_d per day (top) and 3 C_d per day (bottom) during April - June, 2014.

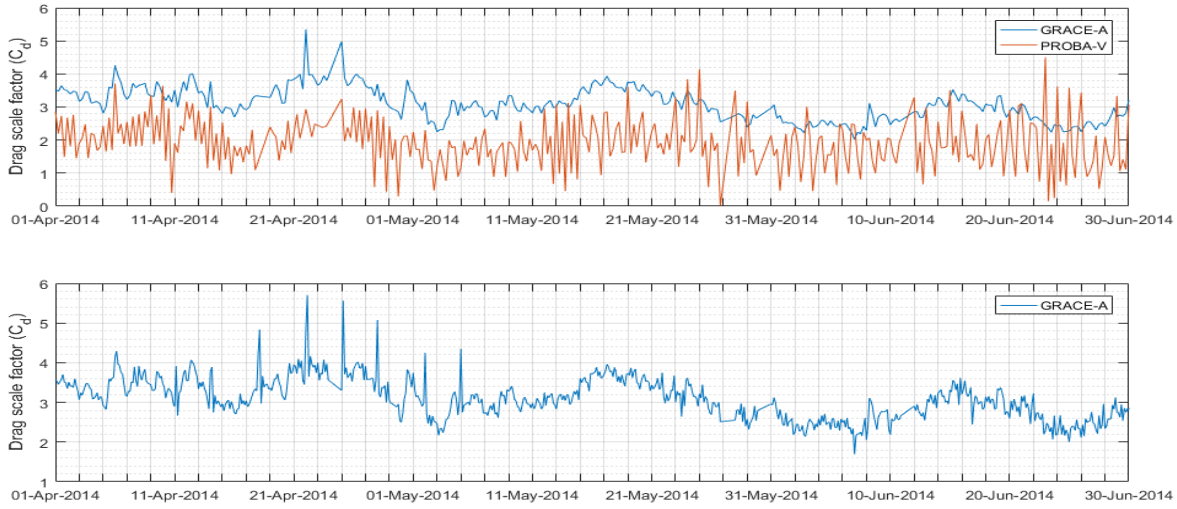

(b) Estimation of 4 C_d per day (top) and 8 C_d per day (bottom) during April - June, 2014.

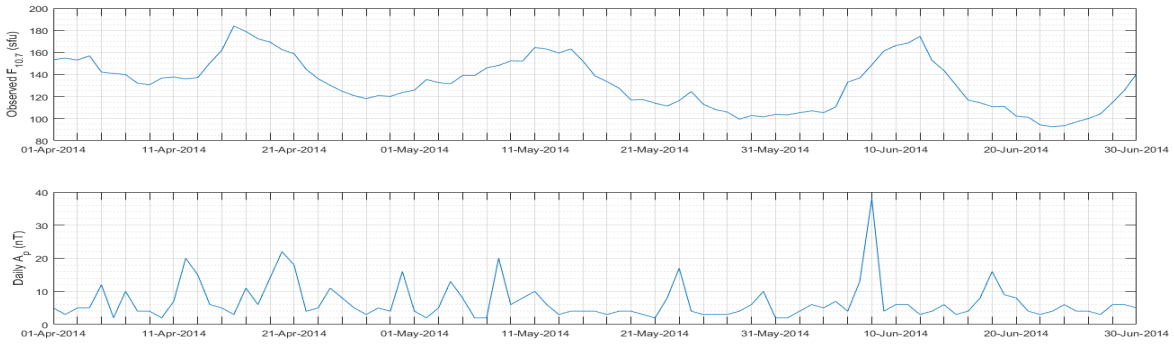

(c) Variation of observed $F_{10.7}$ (top) and daily A_p (bottom) during April - June, 2014.

Figure 4.1: Comparison of the estimated drag scale factors (C_d) of GRACE-A and PROBA-V under different resolutions, with the solar and geomagnetic activity indices during April - June, 2014.

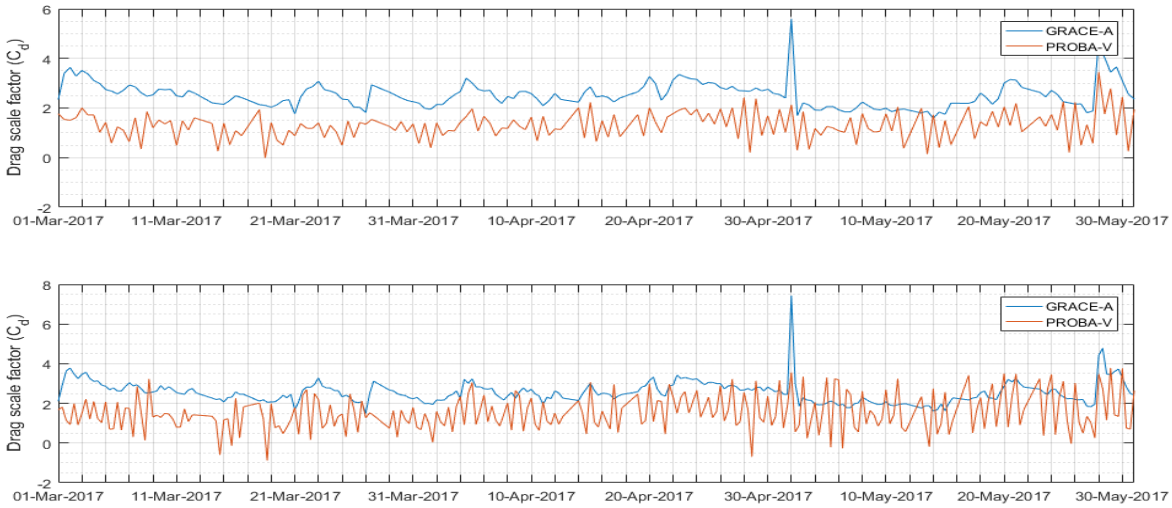

(a) Estimation of 2 C_d per day (top) and 3 C_d per day (bottom) March - May, 2017.

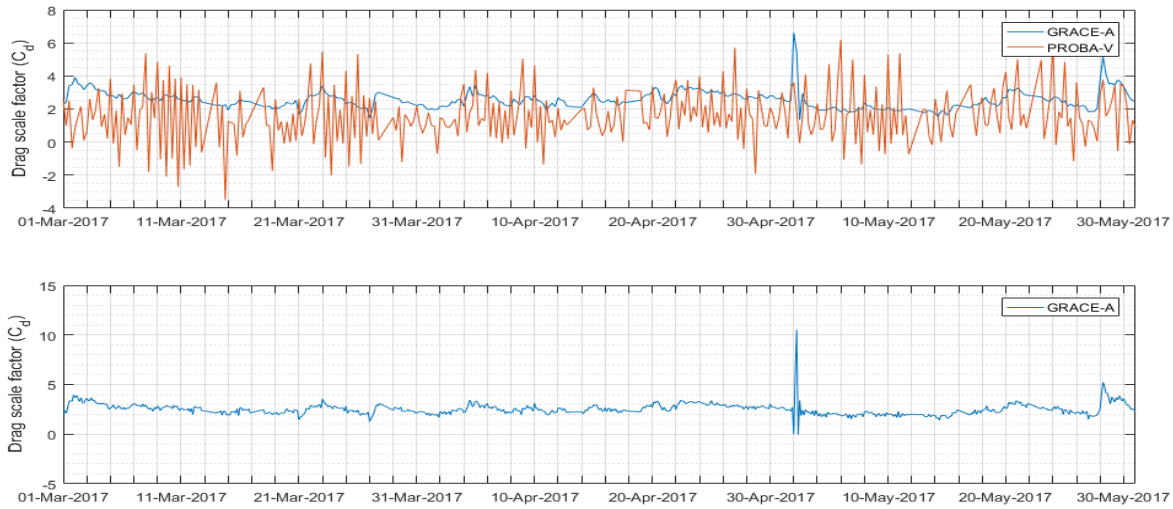

(b) Estimation of 4 C_d per day (top) and 8 C_d per day (bottom) March - May, 2017.

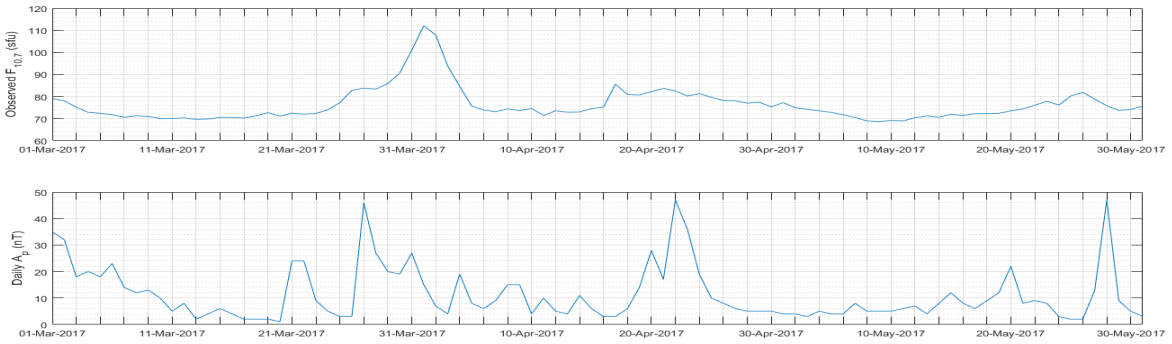

(c) Variation of observed $F_{10.7}$ (top) and daily A_p (bottom) during March - May, 2017.

Figure 4.2: Comparison of the estimated drag scale factors (C_d) of GRACE-A and PROBA-V under different resolutions, with the solar and geomagnetic activity indices during March - May, 2017.

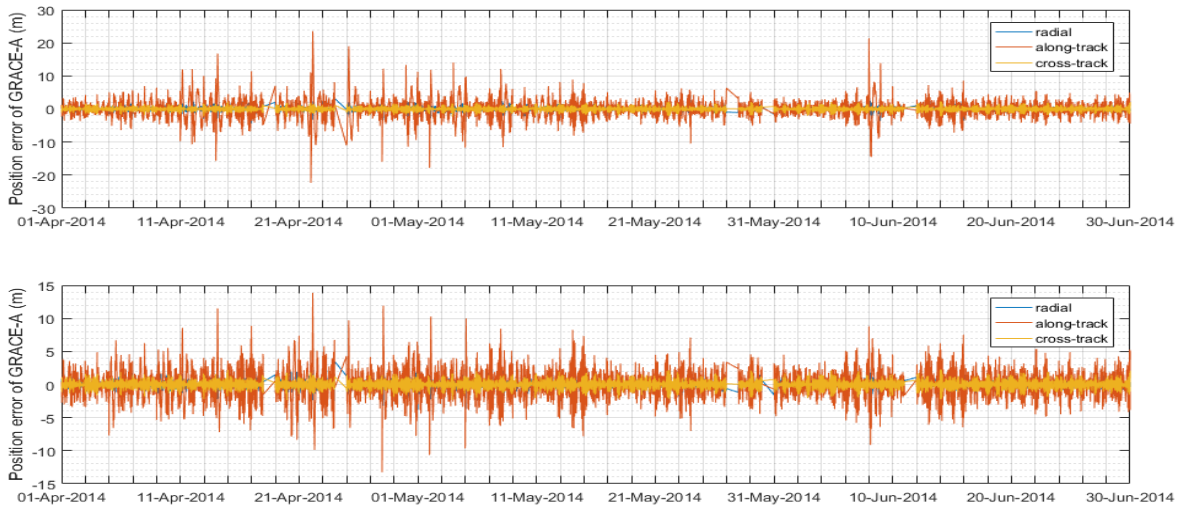

(a) Orbit estimation position errors of GRACE-A with 2 C_d per day resolution (top) and 3 C_d per day resolution (bottom) during April - June, 2014.

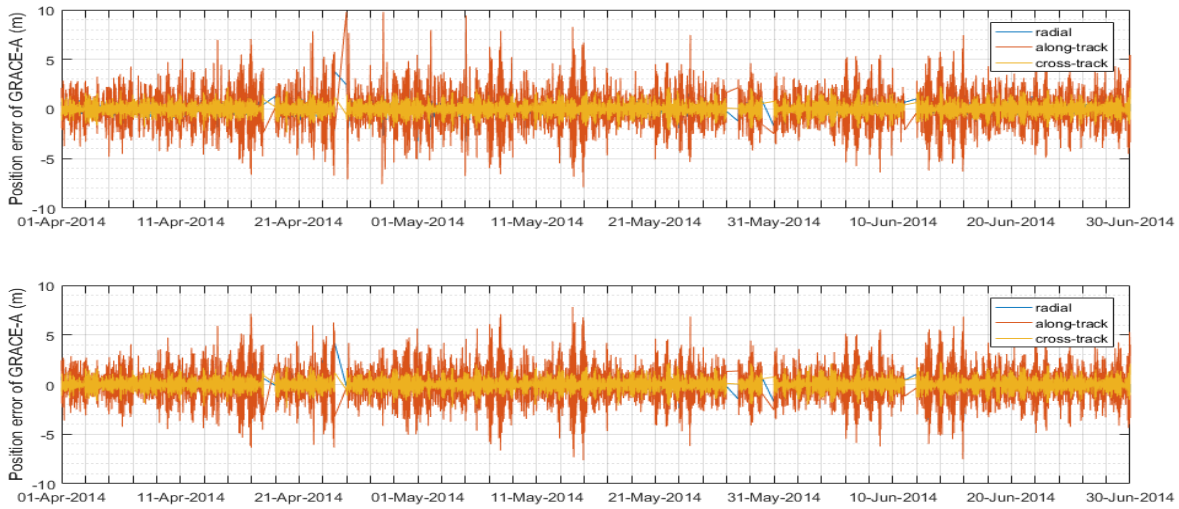

(b) Orbit estimation position errors of GRACE-A with 4 C_d per day resolution (top) and 8 C_d per day resolution (bottom) during April - June, 2014.

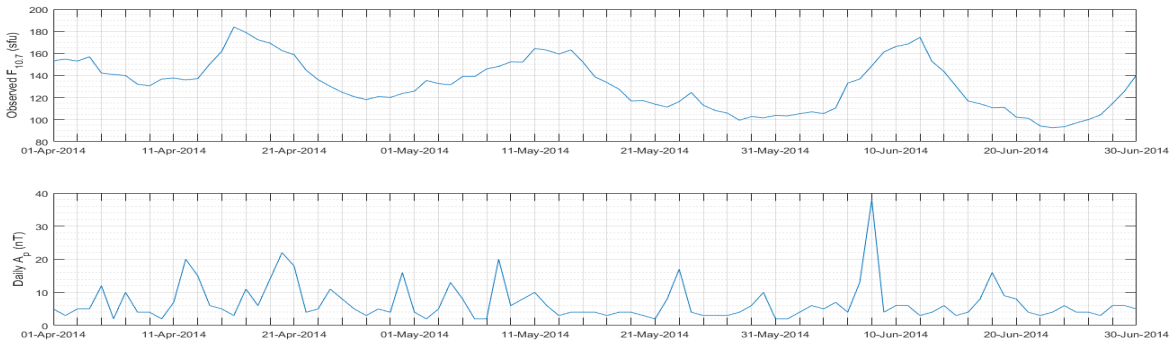

(c) Variation of observed $F_{10.7}$ (top) and daily A_p (bottom) during April - June, 2014.

Figure 4.3: Comparison of the orbit estimation position errors of GRACE-A under different resolutions of estimated C_d, with the solar and geomagnetic activity indices during April - June, 2014.

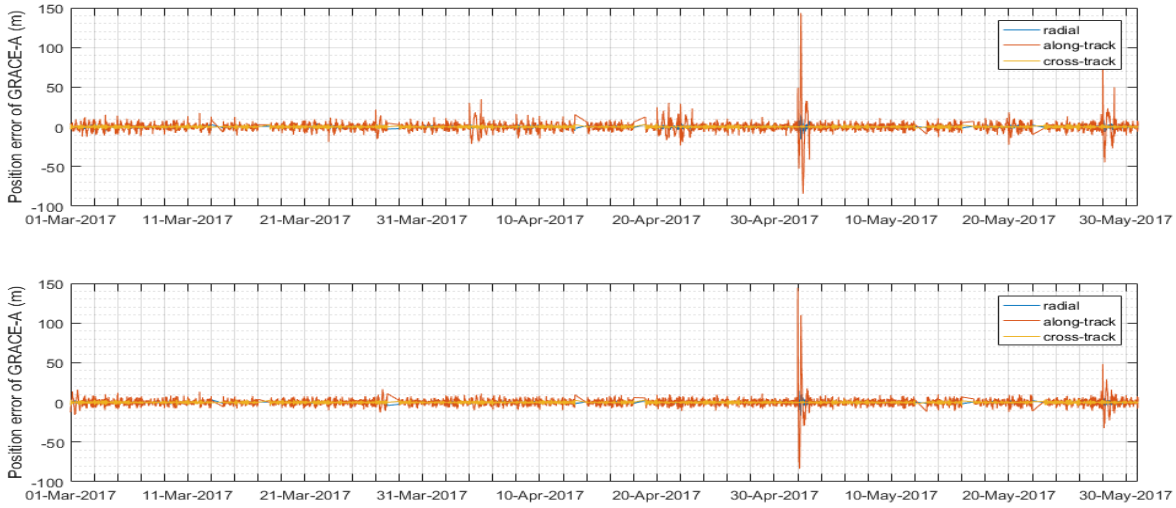

(a) Orbit estimation position errors of GRACE-A with 2 C_d per day resolution (top) and 3 C_d per day resolution (bottom) during March - May, 2017.

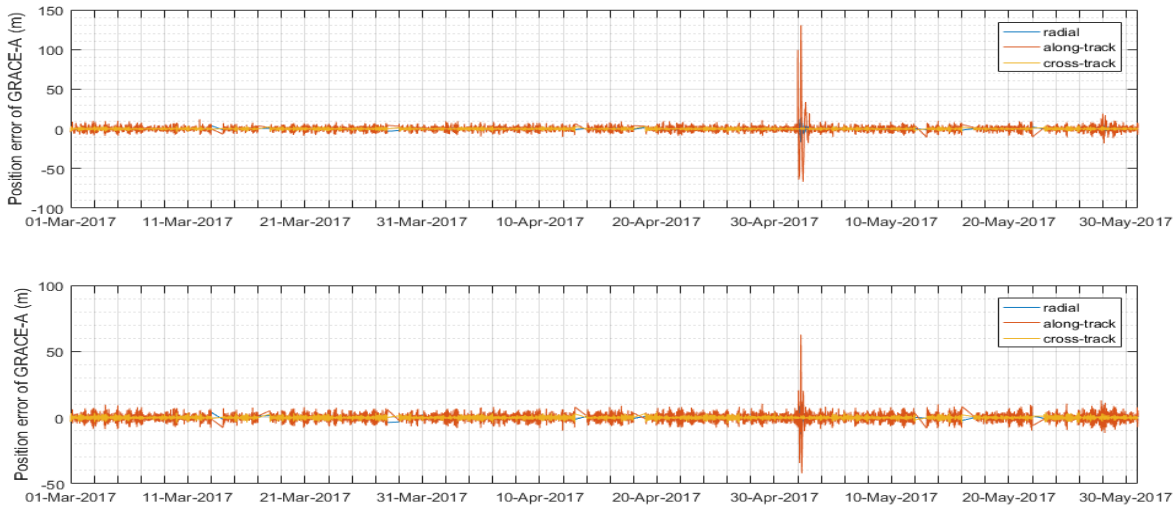

(b) Orbit estimation position errors of GRACE-A with 4 C_d per day resolution (top) and 8 C_d per day resolution (bottom) during March - May, 2017.

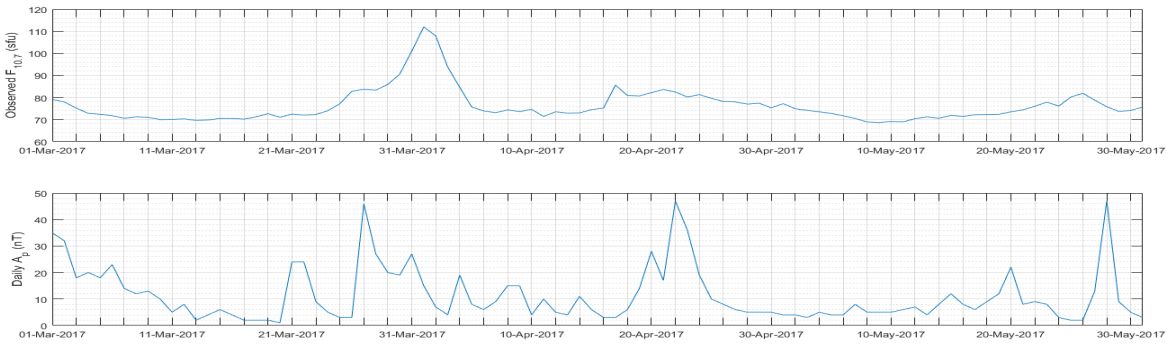

(c) Variation of observed $F_{10.7}$ (top) and daily A_p (bottom) during March - May, 2017.

Figure 4.4: Comparison of the orbit estimation position errors of GRACE-A under different resolutions of estimated C_d, with the solar and geomagnetic activity indices during March - May, 2017.

Period	**Resolution of estimated C_d**	**RMS of position error** (m)			**RMS of velocity error** (m/s)			**3D Position RMS** (m)	**Mean estimated C_d**
		Radial	Along-track	Cross-track	Radial	Along-track	Cross-track		
April to June, 2014	2 C_d per day	0.82	2.81	0.59	0.0028	0.0008	0.0006	3.00	3.10
	3 C_d per day	0.80	2.11	0.59	0.0018	0.0008	0.0006	2.33	3.09
	4 C_d per day	0.79	1.79	0.59	0.0013	0.0008	0.0006	2.05	3.08
	8 C_d per day	0.78	1.64	0.59	0.0011	0.0008	0.0006	1.91	3.09
March to May, 2017	2 C_d per day	1.57	7.13	1.05	0.0076	0.0016	0.0012	7.37	2.53
	3 C_d per day	1.54	5.73	1.05	0.0059	0.0016	0.0012	6.02	2.56
	4 C_d per day	1.52	5.50	1.05	0.0056	0.0016	0.0012	5.81	2.55
	8 C_d per day	1.38	3.27	1.05	0.0026	0.0015	0.0012	3.70	2.52

Table 4.1: Results of estimation with multiple C_d per day for the satellite GRACE-A.

track position error obtained from 2 C_d per day estimation shows a reduction of 52 %. This reduction increases to 72 % for 8 C_d per day estimation. Similar trends can be observed during the period P2. The along-track error during March-May, 2017 is higher than the error during April-June, 2014 due to the low altitude of GRACE-A. It is to be noted that the difference between the along-track error and the error in other directions has reduced compared to the results obtained from one C_d per day estimation. This is an indication that estimating multiple C_d per day better characterizes the variations of drag force within a day. The difference between the mean estimated C_d during April to June, 2014 and March to May, 2017 ranges between 0.5 and 0.6, a relative difference of 17.75 %. Similar to the results of estimation with one C_d per day, this difference is observed in spite of including the solar activity variation in the NRLMSISE-00 model (Section 3.1). This indicates an inadequacy of the atmosphere model in representing the density variations due to solar activity.

Figure 4.5 shows the variation of the 3D RMS of position error for GRACE-A and PROBA-V with the number of estimated drag scale factors per day and the variation of the minimum and maximum values of the estimated C_d of GRACE-A between the periods P1 and P2. From Figure 4.5a, it can be seen that the 3D RMS of position error of GRACE-A decreases with the number of estimated drag scale factors per day, in an exponential fashion. Though the 3D RMS of position error can be expected to decrease when the number of estimated drag scale factors per day is increased to 12, the reduction will not be very appreciable. Hence, it is decided not to proceed with the estimation of 12 drag scale factors per day. Figure 4.5c shows the variation of the minimum and maximum values of the estimated C_d of GRACE-A with the number of estimated drag scale factors per day from which the outlier C_d corresponding to the manoeuvre on May 2, 2017 has been removed. It can be observed that for both periods P1 and P2, the difference between the minimum and the maximum estimated C_d increases with the resolution, suggesting that the estimated C_d becomes unrealistic with the increasing resolution. The 3D RMS of position error of PROBA-V (Figure 4.5b) shows very little change with the increasing resolution. The 3D RMS of the difference between the estimated position of PROBA-V for the resolution of 4 C_d per day and for the resolution of 1 C_d per day comes to around 0.23 m during P1 and 0.17 m during P2. Since the difference is hardly a metre and there is a possibility of obtaining negative drag scale factors during the selected periods, it is decided not to use the results of multiple C_d estimation per day for the orbit prediction of PROBA-V. From Section 3.2, it can be seen that using the estimated C_d of previous day with an estimation resolution of 1 C_d per day for orbit prediction of PROBA-V has a position error no more than 25 m, which is much lower compared to the requirement of

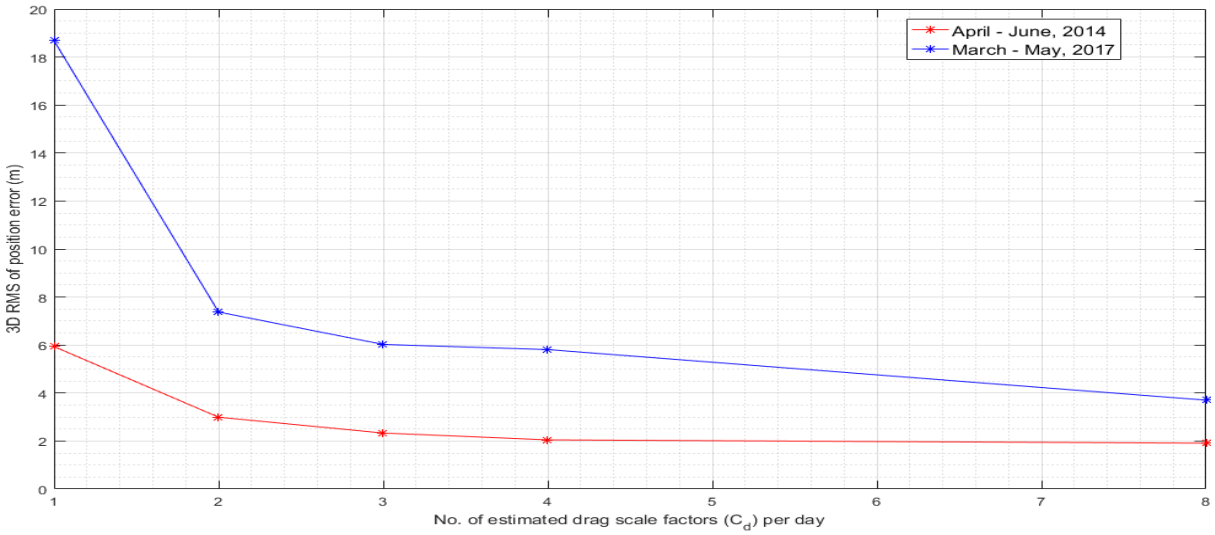

(a)

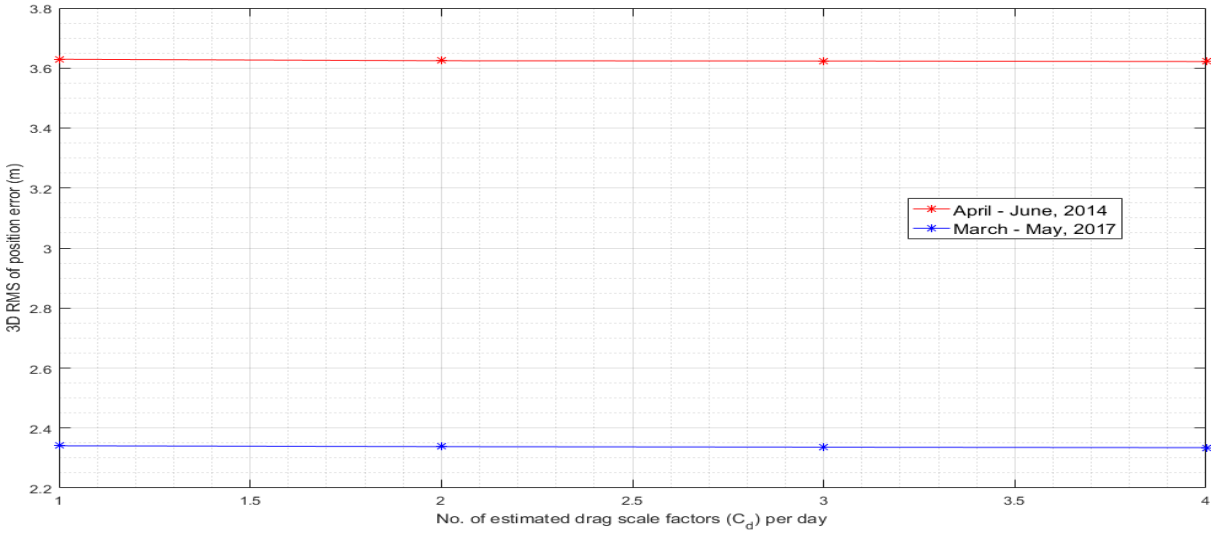

(b)

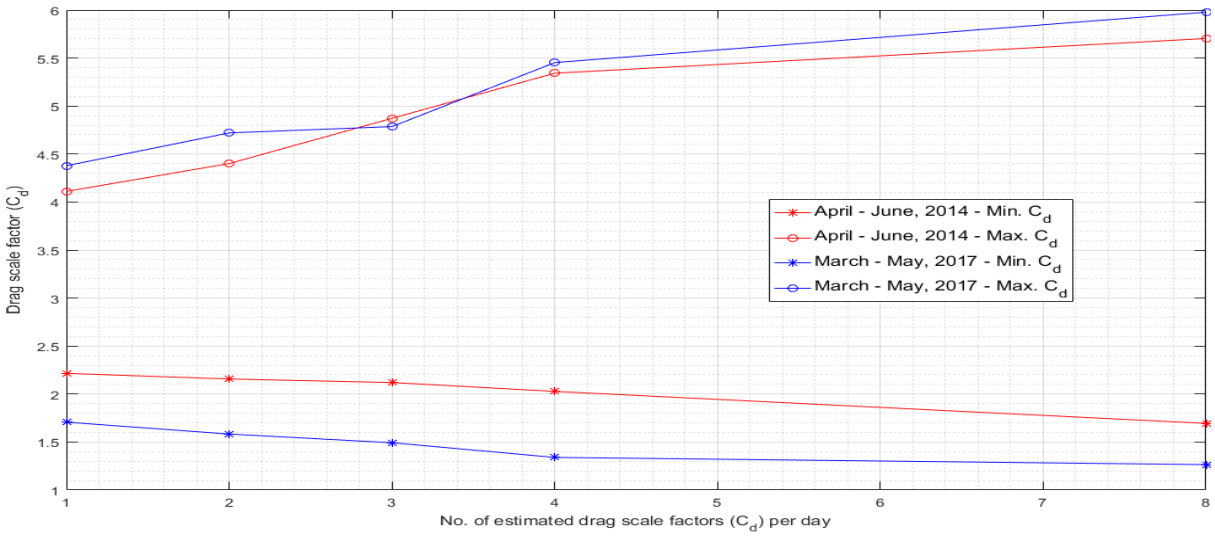

(c)

Figure 4.5: Variation of the 3D position RMS of GRACE-A (Figure 4.5a) and PROBA-V (Figure 4.5b) with the number of estimated drag scale factors per day. Variation of the minimum and maximum values of the estimated C_d of GRACE-A (Figure 4.5c) is also shown.

Period	Prediction method	Prediction Metric (PM)			
		2 C_d per day	3 C_d per day	4 C_d per day	8 C_d per day
April to June, 2014	Last C_d of previous day	0.23	0.22	0.21	0.27
	Mean C_d of previous day	0.25	0.24	0.24	0.24
	Mean C_d of previous week	0.38	0.38	0.38	0.37
	Polynomial fit of previous week C_d	0.40	0.33	0.30	0.31
March to May, 2017	Last C_d of previous day	0.41	0.38	0.36	0.32
	Mean C_d of previous day	0.47	0.48	0.47	0.38
	Mean C_d of previous week	0.46	0.47	0.47	0.42
	Polynomial fit of previous week C_d	0.66	0.60	0.56	0.44

Table 4.2: Values of the prediction metric (PM) for different resolutions of estimated C_d and for different prediction methods.

125 m mentioned in Section 1.3. Hence, it can be concluded that for the orbit prediction of PROBA-V, it is sufficient to make use of the estimated C_d of the previous day with an estimation resolution of 1 C_d per day, for both periods of solar activity.

4.2 Results and interpretation of orbit prediction

The accuracy of orbit prediction depends on the accuracy of the force model used, the numerical integrator employed, the accuracy of the initial state which depends on the accuracy of the resulting trajectory of orbit estimation and a realistic estimate of drag scale factor. Hence, orbit prediction results can also be used as a measure of the quality of orbit determination. Using the results of the multiple C_d estimation per day, orbit prediction was carried out for periods P1 and P2, according to the procedure described in Section 2.3. As explained in Section 2.5, certain days were skipped for prediction based on the availability of the estimation results and the prediction methods used. The values of the prediction metric (PM) were computed to compare the various prediction methods under multiple C_d estimation. Table 4.2 provides the prediction metric (PM) for different resolutions of estimated C_d and for different prediction methods during both periods of solar activity. For each resolution, the lowest prediction metric is highlighted in green colour for both periods. Among the 32 possibilities, only these 8 selected predictions are carried out from which the optimum prediction method for each period is determined. From the table, it can be seen that during April to June, 2014, prediction using the last estimated C_d of the previous day turns out to be the best prediction method except when using the results from the estimation resolution of 8 C_d per day for which prediction using the mean C_d of the previous day is the optimum method. During March to May, 2017, for all resolutions of estimated C_d, prediction using the last estimated C_d of the previous day turns out to be the optimum prediction method.

Figures 4.6 and 4.7 show the comparison of the drag scale factors obtained from the estimation and the 4 different prediction methods, across all estimation resolutions during the periods P1 and P2, respectively. From Figure 4.6, it can be seen that prediction using the polynomial fit of previous week C_d has lower PM compared to prediction using the mean C_d of previous week, except for the 2 C_d per day resolution. This is because with a larger number of estimated C_d per day there are more data points in a given interval

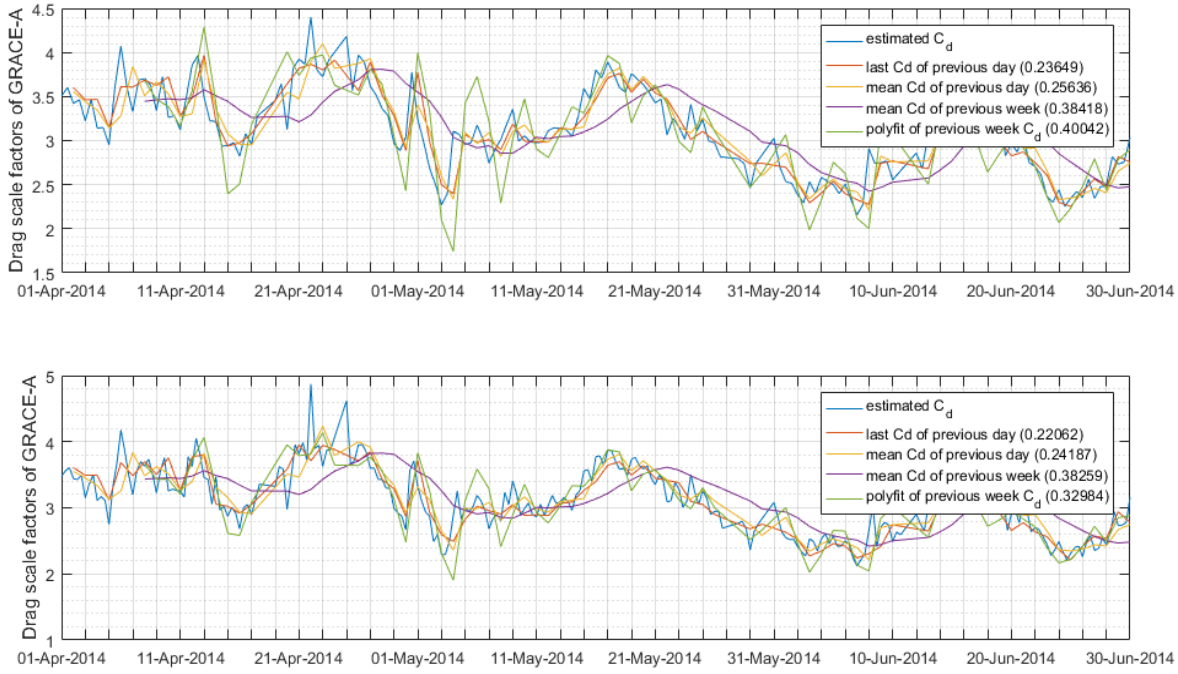

(a) Estimated drag scale factors with 2 C_d per day resolution and its prediction methods (top). Estimated drag scale factors with 3 C_d per day resolution and its prediction methods (bottom).

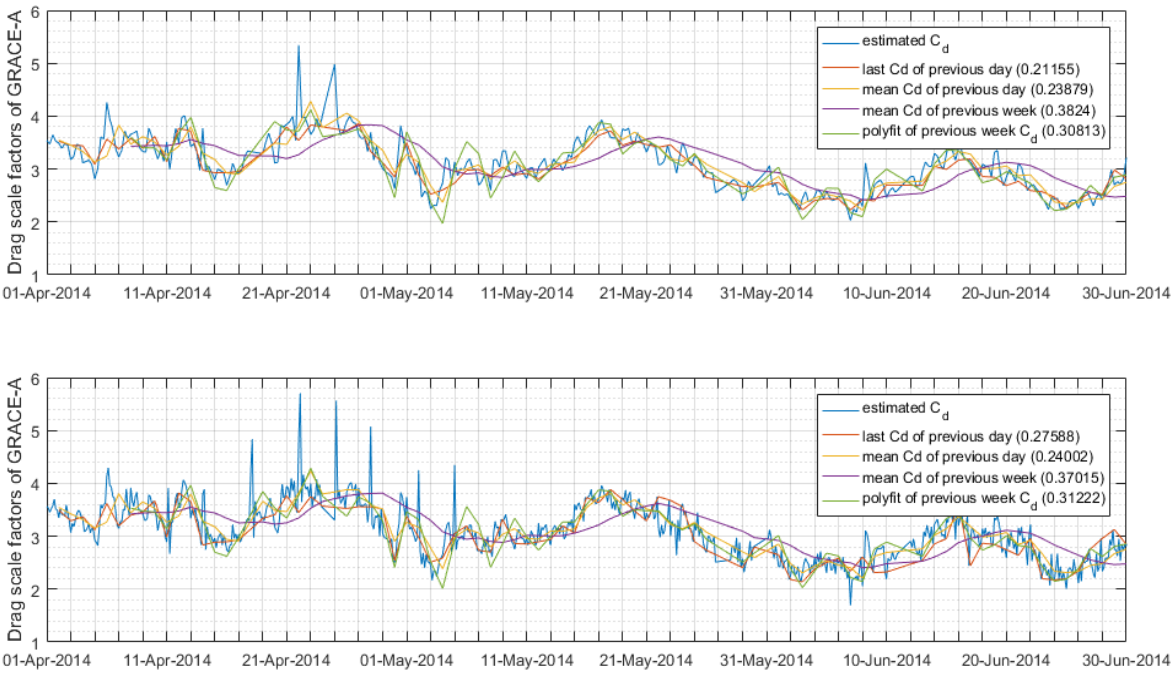

(b) Estimated drag scale factors with 4 C_d per day resolution and its prediction methods (top). Estimated drag scale factors with 8 C_d per day resolution and its prediction methods (bottom).

Figure 4.6: Comparison of the estimated drag scale factors of GRACE-A under different resolutions with their corresponding prediction methods during April - June, 2014. (The value of prediction metric (PM) is mentioned in parentheses in the legend.)

Resolution of estimated C_d	**Selected prediction method**	**Mean of maximum position error** (m)			**Mean of maximum velocity error** (m/s)			**3D RMS of position error** (m)	
		Radial	Along-track	Cross-track	Radial	Along-track	Cross-track	Predicted orbit	Estimated orbit
1 C_d per day	Last C_d of the previous day	8.00	340.39	2.74	0.3810	0.0068	0.0031	209.16	5.93
2 C_d per day	Last C_d of the previous day	7.35	271.78	2.74	0.3035	0.0064	0.0031	170.20	2.99
3 C_d per day	Last C_d of the previous day	7.37	261.60	2.75	0.2921	0.0065	0.0031	156.59	2.33
4 C_d per day	Last C_d of the previous day	7.25	243.47	2.75	0.2716	0.0065	0.0031	148.80	2.05
8 C_d per day	Mean C_d of the previous day	7.66	284.98	2.73	0.3185	0.0066	0.0031	177.77	1.91

Table 4.3: Results of orbit prediction for GRACE-A using different resolutions of the estimated C_d, during April - June, 2014.

Resolution of estimated C_d	**Selected prediction method**	**Mean of maximum position error** (m)			**Mean of maximum velocity error** (m/s)			**3D RMS of position error** (m)	
		Radial	Along-track	Cross-track	Radial	Along-track	Cross-track	Predicted orbit	Estimated orbit
1 C_d per day	Mean C_d of the previous week	17.70	1031.15	5.30	1.181	0.0140	0.0061	665.68	18.68
2 C_d per day	Last C_d of the previous day	14.22	677.38	5.29	0.7751	0.0122	0.0061	522.25	7.37
3 C_d per day	Last C_d of the previous day	12.92	552.85	5.28	0.6321	0.0113	0.0061	455.21	6.02
4 C_d per day	Last C_d of the previous day	12.39	525.71	5.27	0.6008	0.0109	0.0061	444.78	5.81
8 C_d per day	Last C_d of the previous day	13.89	640.14	5.28	0.7328	0.0116	0.0061	461.19	3.70

Table 4.4: Results of orbit prediction for GRACE-A using different resolutions of the estimated C_d, during March - May, 2017.

for fitting a third order polynomial. This makes it possible to better characterize the C_d variation than computing an average C_d per week. From Figure 4.7, it can be seen that prediction using the mean C_d of previous week has lower PM than the prediction using the mean C_d of the previous day, except for the 8 C_d per day resolution. Though it is an interesting variation compared to the C_d variations during the period P1, it is not relevant for this thesis. The figure also shows that the manoeuvre on May 2, 2017 is closely followed by the curves of the methods 'polynomial fit of previous week C_d' and 'mean C_d of previous day'.

Figures 4.8 and 4.9 show the results of the selected orbit prediction cases (Table 4.2) during the periods P1 and P2, respectively. In both figures, a gradual reduction in the along-track error component can be observed with the increasing resolution of estimated C_d except for the resolution of 8 C_d per day. During both periods P1 and P2, for the resolution of 4 C_d per day, the magnitude of the along-track error peaks is smaller compared to the magnitude of the along-track error peaks of other resolutions. This suggests that a mere increase in the resolution of estimated C_d does not always result in better predictions. A very low correlation of 8 % is observed between the prediction position errors of GRACE-A and the observed $F_{10.7}$ during P1 for the resolutions of 4 and 8 C_d per day. This correlation drops to 6 % during P2.

Tables 4.3 and 4.4 show the results of these 8 selected prediction cases along with

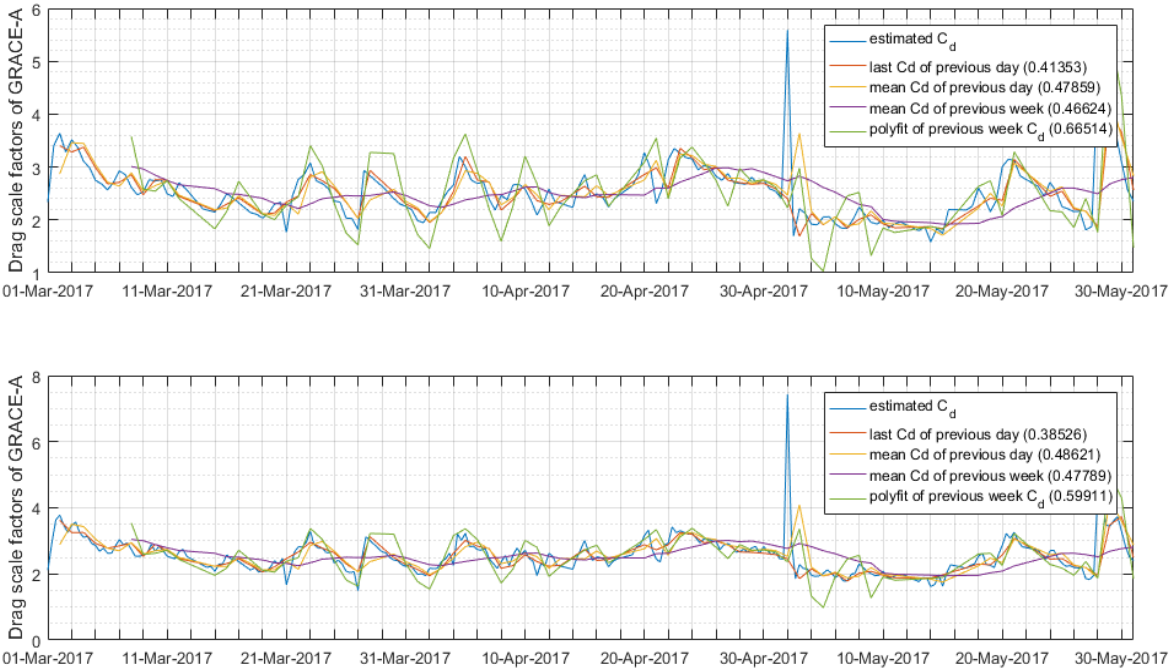

(a) Estimated drag scale factors with 2 C_d per day resolution and its prediction methods (top). Estimated drag scale factors with 3 C_d per day resolution and its prediction methods (bottom).

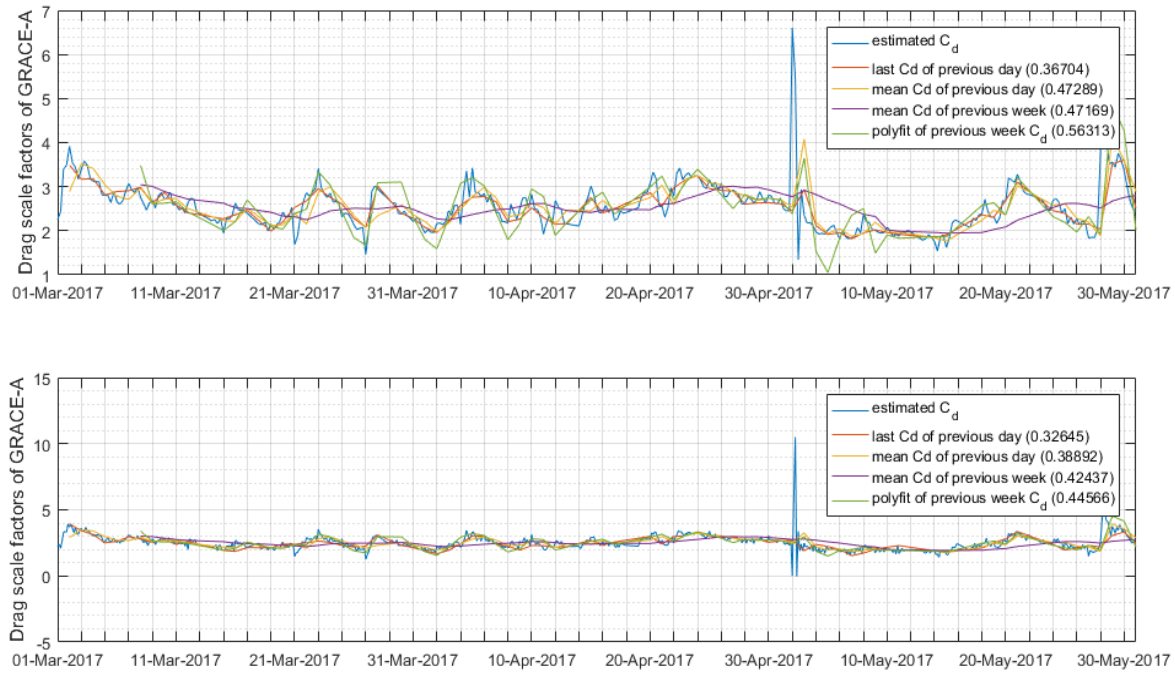

(b) Estimated drag scale factors with 4 C_d per day resolution and its prediction methods (top). Estimated drag scale factors with 8 C_d per day resolution and its prediction methods (bottom).

Figure 4.7: Comparison of the estimated drag scale factors of GRACE-A under different resolutions with their corresponding prediction methods during March - May, 2017. (The value of prediction metric (PM) is mentioned in parentheses in the legend.)

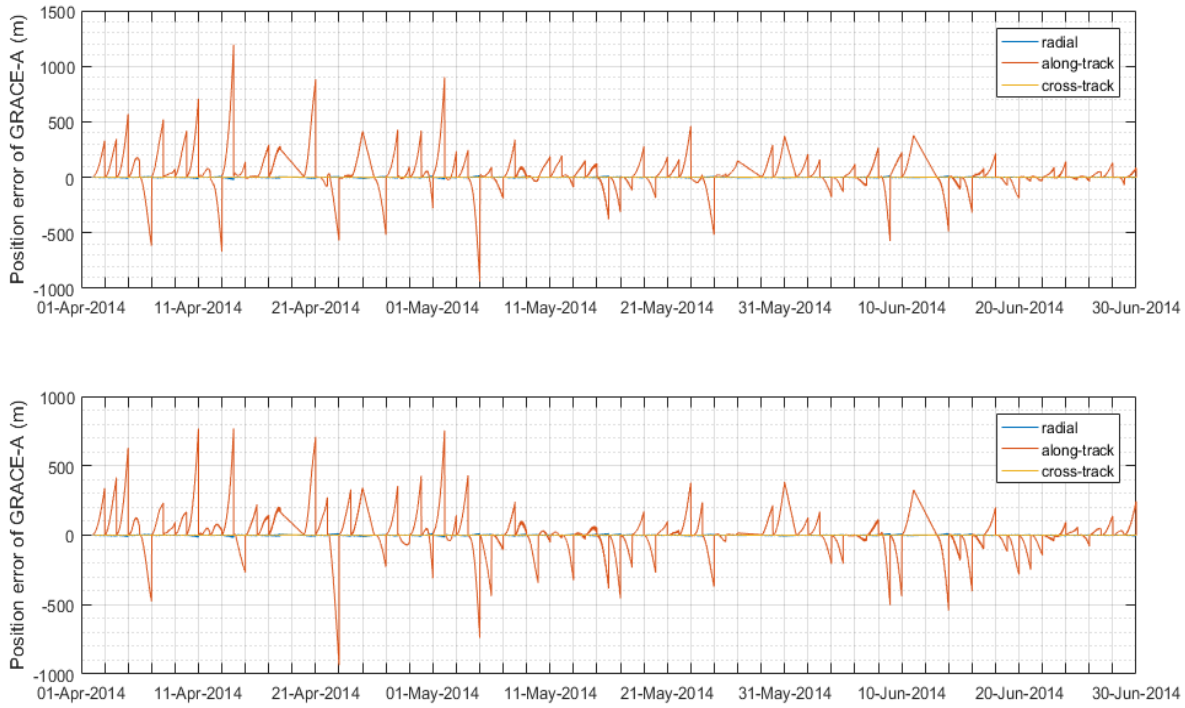

(a) Orbit prediction position errors of GRACE-A with 2 C_d per day estimation (top) and 3 C_d per day estimation (bottom) during April - June, 2014 (Prediction method used: last C_d of previous day for both cases).

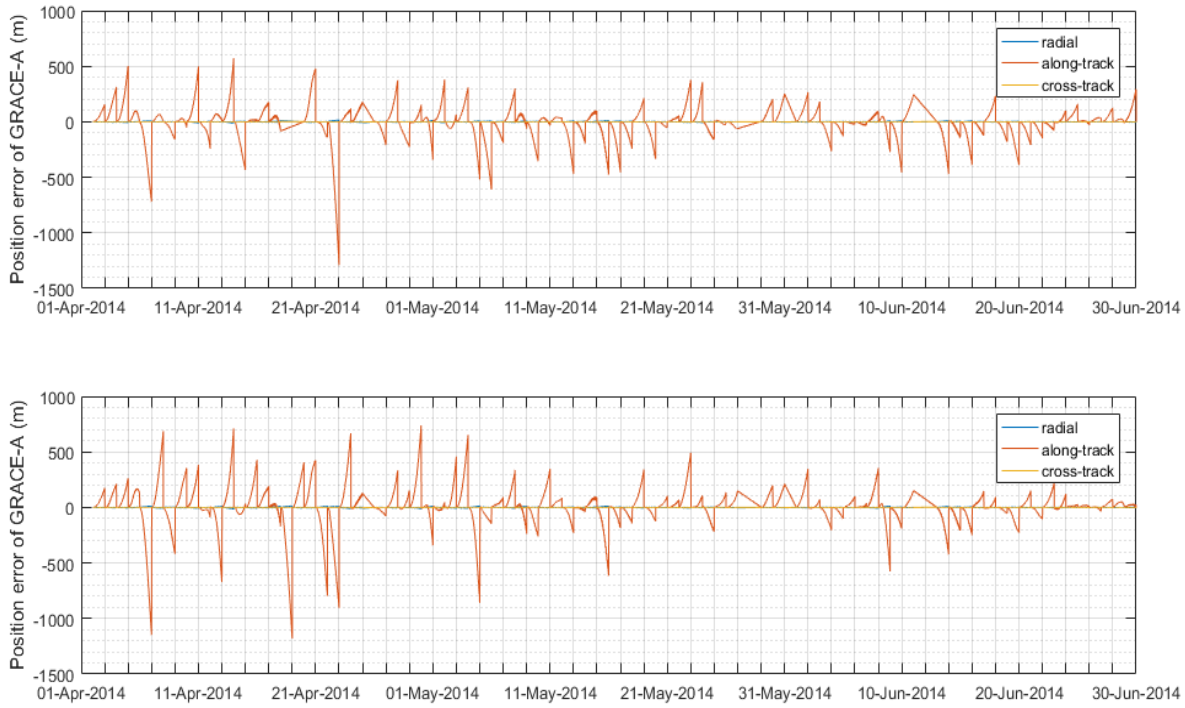

(b) Orbit prediction position errors of GRACE-A with 4 C_d per day estimation (top) and 8 C_d per day estimation (bottom) during April - June, 2014 (Prediction method used: last C_d of previous day for 4 C_d per day and mean C_d of previous day for 8 C_d per day).

Figure 4.8: Orbit prediction position errors of GRACE-A under different resolutions of estimated C_d during April - June, 2014.

(a) Orbit prediction position errors of GRACE-A with 2 C_d per day estimation (top) and 3 C_d per day estimation (bottom) during March - May, 2017 (Prediction method used: last C_d of previous day for both cases).

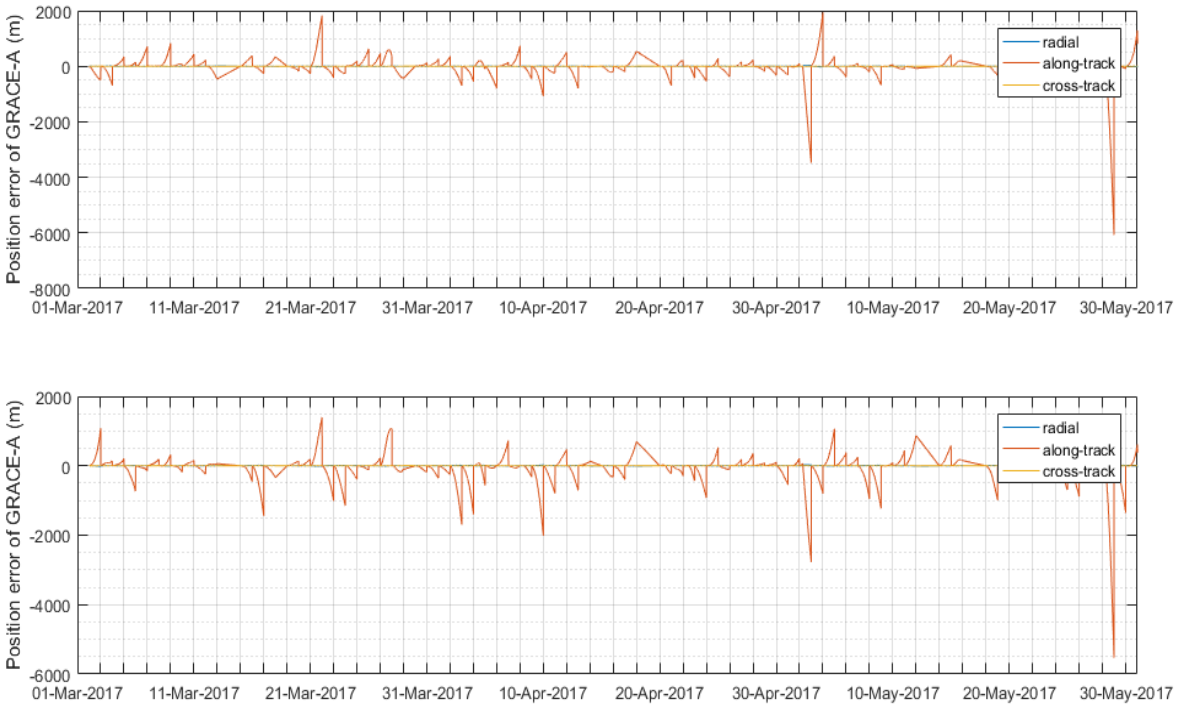

(b) Orbit prediction position errors of GRACE-A with 4 C_d per day estimation (top) and 8 C_d per day estimation (bottom) during March - May, 2017 (Prediction method used: last C_d of previous day for both cases).

Figure 4.9: Orbit prediction position errors of GRACE-A under different resolutions of estimated C_d during March - May, 2017.

Parameter	GRACE-A	SAOCOM-CS	PROBA-V
Altitude (km)	415.56	619.60	812.68
Orbital velocity (km/s)	7.66	7.55	7.45
Mass (kg)	464.30	400.00	138.00
Reference area (m^2)	1.0013	3.7700	1.1314
Density (kg/m^3)	$4.13*10^{-12}$	$2.44*10^{-13}$	$2.52*10^{-14}$

Table 4.5: Parameters considered for rule of thumb analysis (Date used: April 1, 2014)

the results from prediction using one drag scale factor per day (Section 3.2). During March - May, 2017, for the estimation resolution of 1 C_d per day, the method of using the mean C_d of the previous week has been selected as it gives the least 3D RMS of position error of the predicted orbit. Because of the low altitude of GRACE-A, the prediction errors during P2 are larger than the errors during P1. The optimum prediction method for the periods is chosen based on the mean of maximum position error in the along-track direction and the 3D RMS of position error of the predicted orbit. Figure 4.10 shows the variation of these quantities with the number of estimated C_d along with the corresponding prediction method during the periods P1 and P2. During both periods, it can be seen that both these quantities reach a minimum value for the estimation resolution of 4 C_d per day with the prediction method being the use of last estimated C_d of the previous day. Hence, this combination of estimation and prediction proves to be the best prediction strategy for GRACE-A for both periods P1 and P2.

Though the resolution of 8 C_d per day gives the lowest value for the 3D RMS of the estimated position (Figure 4.5a) which translates to an improvement in the estimate of the initial state, it does not necessarily give better prediction results compared to 4 C_d per day estimation. This is because the 4 C_d per day resolution gives more realistic estimates for the drag scale factors. This leads to the interpretation that beyond a certain resolution, the estimated C_d contributes more to the quality of orbit prediction than the initial state. Hence, for better orbit prediction, the models used in the computation of aerodynamic acceleration (satellite geometry, gas-surface interaction and thermosphere models) should be improved instead of increasing the resolution of the estimated C_d. The prediction strategy used by Jäggi et al. [2011] for GOCE satellite during 2009 gave a mean along-track error of 1089 m for an altitude range of 275-265 km with a prediction arc length of 24 hours. In comparison, the best prediction strategy for GRACE-A during March - May, 2017 results in a mean along-track error of 526 m for an altitude of 333 km with a prediction arc length of 24 hours. Considering the difference in altitude and satellite specific drag coefficient, an error of 526 m is comparable to the results obtained by Jäggi et al. [2011].

4.3 Interpolating the results for orbit prediction of SAOCOM-CS

This section presents a rule of thumb analysis for obtaining the maximum position error in the predicted orbit of SAOCOM-CS for a prediction arc length of one day. Since there

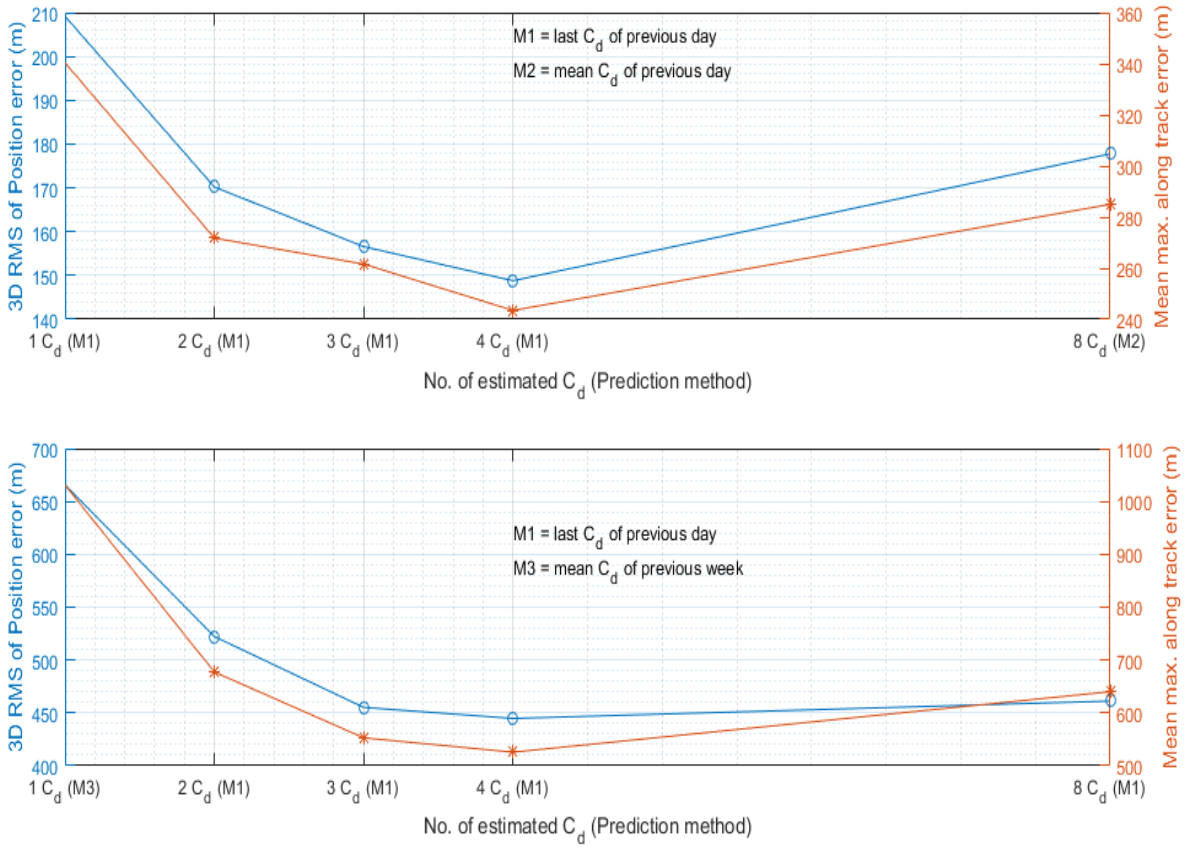

Figure 4.10: Variation of 3D RMS of position error and mean maximum along-track error of the predicted orbit with the estimation and prediction techniques, during April - June, 2014 (top) and March - May, 2017 (bottom).

Satellite name	**Acceleration ratio**	**Maximum position error from linear interpolation (m)**	**Maximum position error from exponential interpolation (m)**
GRACE-A	1.00 (baseline)	243.50	243.50
SAOCOM-CS	0.25	75.59	41.32
PROBA-V	0.02	24.10	24.10

Table 4.6: Results of the rule of thumb analysis

is no orbit data available for SAOCOM-CS or any other satellite at the same altitude (619.60 km), some assumptions are used to arrive at the maximum position error of the predicted orbit. Table 4.5 lists the parameters of the three satellites that are used in the rule of thumb analysis. The NRLMSISE-00 atmosphere model is used to obtain the density at the respective altitudes of the satellites on April 1, 2014, the date used for the analysis. This day has high solar activity and therefore presents a conservative estimate of the maximum position error. The magnitude of the acceleration due to drag force acting on the satellite is given by,

$$|\ddot{\mathbf{r}}_{\mathrm{D}}| \;=\; \frac{1}{2}\,\rho\,\frac{A_{\mathrm{ref}}}{M}\,C_{\mathrm{d}}\,v_{\mathrm{r}}^{2}\,|\hat{\mathbf{v}}_{\mathrm{r}}| \tag{4.1}$$

where ρ is the atmosphere density, A_{ref} is the reference area for drag force, M is the mass of the satellite, C_d is drag coefficient of the satellite, v_{r} is the magnitude of the relative velocity and $|\hat{\mathbf{v}}_{\mathrm{r}}|$ is a unit vector. Assuming the orbital velocity as the relative velocity and substituting the relevant parameters from Table 4.5, the drag acceleration acting on the satellites becomes,

$$|\ddot{\mathbf{r}}_{\mathrm{D}}|_{\mathrm{G}} \;=\; (C_{\mathrm{d}})_{\mathrm{G}}\,(2.613 * 10^{-7}) \tag{4.2}$$

$$|\ddot{\mathbf{r}}_{\mathrm{D}}|_{\mathrm{S}} \;=\; (C_{\mathrm{d}})_{\mathrm{S}}\,(6.55 * 10^{-8}) \tag{4.3}$$

$$|\ddot{\mathbf{r}}_{\mathrm{D}}|_{\mathrm{P}} \;=\; (C_{\mathrm{d}})_{\mathrm{P}}\,(5.733 * 10^{-9}) \tag{4.4}$$

where $|\ddot{\mathbf{r}}_{\mathrm{D}}|_{\mathrm{G}}$, $|\ddot{\mathbf{r}}_{\mathrm{D}}|_{\mathrm{S}}$ and $|\ddot{\mathbf{r}}_{\mathrm{D}}|_{\mathrm{P}}$ are the drag accelerations of GRACE-A, SAOCOM-CS & PROBA-V respectively and $(C_{\mathrm{d}})_{\mathrm{G}}$, $(C_{\mathrm{d}})_{\mathrm{S}}$ and $(C_{\mathrm{d}})_{\mathrm{P}}$ are the drag coefficients of GRACE-A, SAOCOM-CS & PROBA-V respectively. Assuming $(C_{\mathrm{d}})_{\mathrm{G}} = (C_{\mathrm{d}})_{\mathrm{S}} = (C_{\mathrm{d}})_{\mathrm{P}}$, the ratio of drag acceleration becomes,

$$\frac{|\ddot{\mathbf{r}}_{\mathrm{D}}|_{\mathrm{S}}}{|\ddot{\mathbf{r}}_{\mathrm{D}}|_{\mathrm{G}}} \;=\; 0.25 \tag{4.5}$$

$$\frac{|\ddot{\mathbf{r}}_{\mathrm{D}}|_{\mathrm{P}}}{|\ddot{\mathbf{r}}_{\mathrm{D}}|_{\mathrm{G}}} \;=\; 0.022 \tag{4.6}$$

in which the drag acceleration of GRACE-A is considered as baseline. Using Equation (3.1) and Table 4.3, the maximum position error of GRACE-A for the best prediction method during the chosen solar maximum (April - May, 2014) is obtained as 243.5 m. Similarly, for PROBA-V, the maximum position error during the same period is obtained as 24.1 m. Using MATLAB, a first order polynomial model ($y \;=\; a\,x \,+\, b$) and a single-term exponential model ($y \;=\; a\,\exp(b\,x)$) are fit, considering the ratio of drag acceleration as x and the maximum position error as y. Evaluating the constants a and b for both models and employing the drag acceleration ratio of SAOCOM-CS as input, the maximum position error is obtained as 75.59 m for the first order polynomial model and 41.32 m for the exponential model. The results are summarized in Table 4.6. Hence, based on the rule of thumb analysis, when the best prediction strategy of GRACE-A is used for SAOCOM-CS, the resulting maximum position error, considering linear and exponential interpolation, is still within the requirement of 125 m.

Chapter 5

Effects of space weather forecast errors on satellite orbit prediction

The orbit prediction strategies discussed in Chapters 3 and 4 make use of the observed space weather indices ($F_{10.7}$ and A_p) of the prediction arc, as mentioned in Section 2.3. However, real world orbit prediction involves the use of forecast values of $F_{10.7}$ and A_p. The major driving factors of the thermospheric neutral density are the Extreme Ultra Violet (EUV) and particle (solar wind) radiation from the Sun. The dynamic state of the thermosphere depends on the relative forcing between these inputs. Geomagnetic storms, which are a result of energy transfer between the solar wind and thermosphere mainly at high latitudes, account for about 20 % of thermospheric heating [Marcos et al., 2010]. The occurrence of these storms are episodic and unpredictable. Marcos et al. [2010] provides a short account of the thermospheric density response at 400 km altitude to the geomagnetic superstorm of 2004.

Research in the area of density modelling indicates imperfect correlations between $F_{10.7}$, A_p and density, which is a large source of error. The proxies are ground-based measurements, with a limited temporal and spatial sampling. By their very nature, they are not truly representing the processes happening at the satellite altitude [Doornbos et al., 2007]. Because of these limitations, even accurate forecast of $F_{10.7}$ and A_p will result in inaccurate orbit propagation. This demands the need for new thermospheric models with more accurate solar and geomagnetic indices. The new model Jacchia-Bowman 2006 (JB06) has 3 components in solar indices: EUV (Extreme Ultra Violet) measurements in the 250-300 nm range from the Solar & Heliospheric Observatory (SOHO) satellite, FUV (Far Ultra Violet) MgII data (from Solar Backscatter Ultraviolet spectrographs on Nimbus satellites) and $F_{10.7}$. An improved model, Jacchia-Bowman 2008 (JB08) based on JB06, has a new index called Dst (disturbance storm time) index for geomagnetic storms. Another important factor not included in the NRLMSISE-00 model is the change in thermospheric density of 5 % per decade due to climate change. This is due to the transport of the greenhouse gases to the lower thermosphere [Marcos et al., 2010, Panzetta et al., 2019]. For the case of satellite orbit prediction, the empirical model used has to rely on the imperfect forecasts of the already inadequate space weather proxies. This calls for a need to improve the forecast of the space weather indices that describe thermospheric heating [Doornbos and Klinkrad, 2006, Marcos et al., 2010]. Schiemenz et al. [2019] derived a universal analytic approximation of density uncertainty caused by uncertainty in solar EUV flux. This was done by ascertaining the sensitivity of the exospheric temperature

Period	Mean % error in $F_{10.7}$ forecast
April, 2014 (extrapolated)	10.70
April, 2016	7.78
March, 2017 (interpolated)	6.40
November, 2018	4.01
May, 2019	4.57

Table 5.1: Mean percentage error in the $F_{10.7}$ forecast obtained from various space weather files

to the changes in the daily solar flux input.

This chapter deals with the effects of forecast errors in $F_{10.7}$ and A_p indices on the results of orbit prediction of GRACE-A and PROBA-V. This is accomplished by carrying out the orbit predictions using predetermined errors in the indices. The best prediction strategies of GRACE-A and PROBA-V are used. Hence, for GRACE-A, the estimation results of 4 C_d per day are used along with prediction using the last estimated C_d of previous day and for PROBA-V, the estimation results of 1 C_d per day are used along with prediction using the estimated C_d of previous day. Data regarding $F_{10.7}$, A_p indices and geomagnetic storms were obtained from `https://celestrak.com/SpaceData/` and `https://www.swpc.noaa.gov/sites/default/files/images/u2/Usr_guide.pdf`. Section 5.1 presents a method of arriving at the predetermined error for $F_{10.7}$ index and the results of this error on orbit prediction. Section 5.2 provides the effect of random variations in A_p index on orbit prediction as well as the performance of the orbit prediction method during various categories of geomagnetic storms.

5.1 Effect of error in solar radio flux forecast

Three archived space weather files pertaining to April 2016, November 2018 and May 2019 were obtained. Each file included a 44 day forecast of the $F_{10.7}$ index. The forecast values of the first seven forecast days were compared with the corresponding observed values of $F_{10.7}$. These differences were translated in terms of percentage errors and are shown in Figure 5.1a. A positive percentage error indicates a higher value of forecast $F_{10.7}$ than the observed $F_{10.7}$. The absolute values of the mean percentage errors in the $F_{10.7}$ forecast for the first seven forecast days are obtained. The mean values thus obtained are extrapolated and interpolated to obtain the absolute value of mean percentage error in the $F_{10.7}$ forecast during April 2014 and March 2017. These results are summarized in Table 5.1 and are shown in Figure 5.1b. From the figure, it can be observed that the mean percentage error in $F_{10.7}$ forecast decreases and reaches a minimum during November, 2018. This is because during periods of high solar activity (April, 2014) variations in the thermospheric heat inputs are hard to predict.

The period P1 (April - June, 2014) is used to test the error in $F_{10.7}$ forecast for both satellites as the mean percentage error during April 2014 (10.70 %) is higher than the error during March 2017 (6.40 %). The initial state for GRACE-A is obtained from

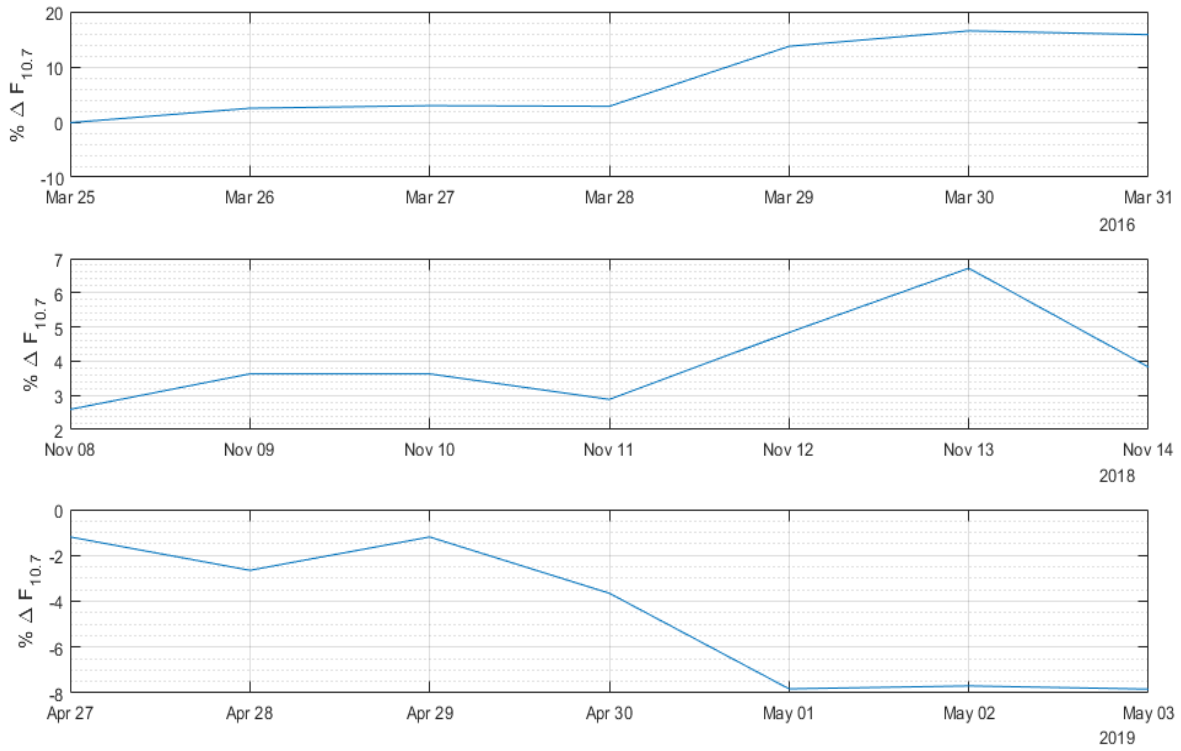

(a) Difference between the forecast and observed solar radio flux for first 7 forecast days in 2016, 2018 and 2019 (Positive values indicate a higher value of forecast $F_{10.7}$ than the observed).

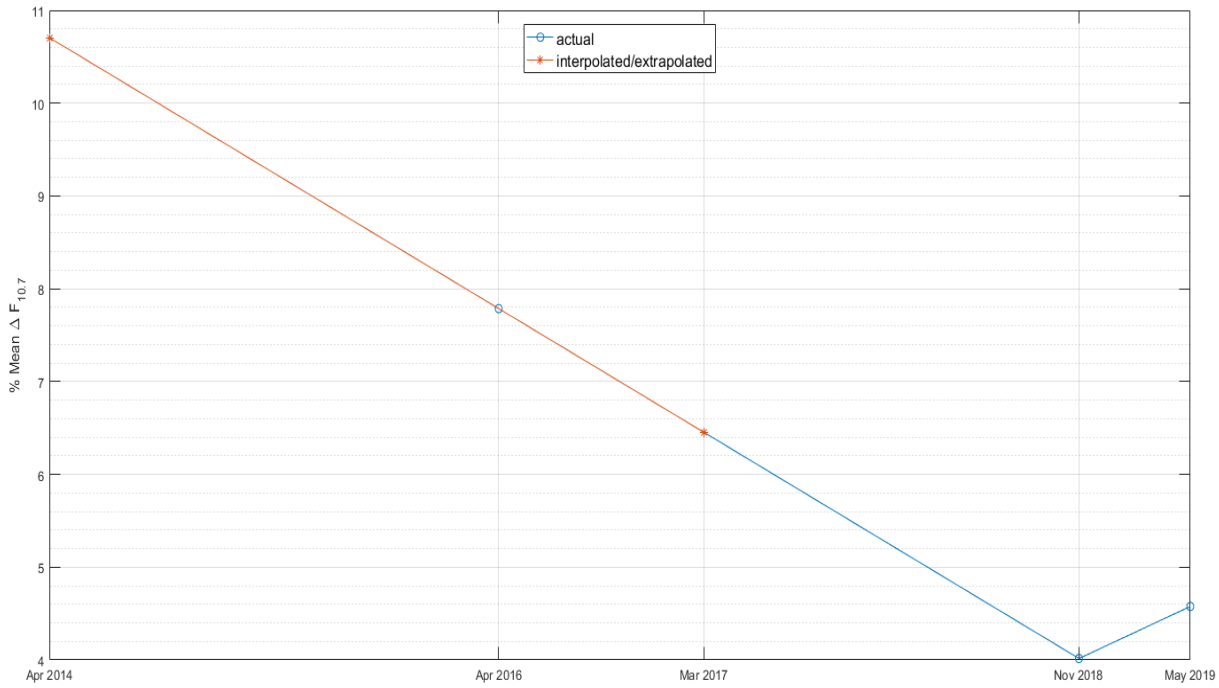

(b) Mean percentage error in solar radio flux forecast during April, 2014 (extrapolated) and March, 2017 (interpolated).

Figure 5.1

Case	Satellite name	Mean of maximum along-track error(m)	3D RMS of predicted orbit (m)
Nominal	GRACE-A	243.47	148.80
	PROBA-V	13.30	6.09
Positive 10% error in $F_{10.7}$	GRACE-A	356.00	203.86
	PROBA-V	13.87	6.26
Negative 10% error in $F_{10.7}$	GRACE-A	392.28	226.22
	PROBA-V	15.75	7.45

Table 5.2: Change in orbit prediction errors in response to change in $F_{10.7}$ during April - June, 2014.

the output of 4 C_d per day estimation and the last estimated C_d of previous day is taken as the drag scale factor for predicted orbit. For PROBA-V, the initial state is obtained from the output of 1 C_d per day estimation and the estimated C_d of previous day is taken as the drag scale factor for prediction. Both positive and negative mean percentage error in $F_{10.7}$ index are included in the density model as follows,

$$F_{10.7} = F_{10.7}(obs) + 0.10 * F_{10.7}(obs) \tag{5.1}$$

$$F_{10.7} = F_{10.7}(obs) - 0.10 * F_{10.7}(obs) \tag{5.2}$$

where $F_{10.7}(obs)$ is the observed value of $F_{10.7}$ for the corresponding prediction arc. Figure 5.2 shows the orbit prediction position errors for both satellites for both cases. From the figure, it can be seen that for a +10 % error in $F_{10.7}$, the overall along-track error in the predicted orbit of GRACE-A is positive, indicating that the satellite would lag behind in its orbit due to higher drag. For a -10 % error in $F_{10.7}$, the overall along-track error in the predicted orbit of GRACE-A is negative, indicating less drag force. Similar results are observed for PROBA-V, but with much smaller along-track error.

The results of both prediction cases are listed in Table 5.2. Statistics of radial and cross-track error components are not shown as they don't exhibit significant variation. PROBA-V shows a maximum of 2.5 m increase in the along-track error corresponding to -10 % error in $F_{10.7}$ whereas the along-track error of GRACE-A increases by 61 % corresponding to -10 % error in $F_{10.7}$. It is interesting to note that both satellites show a larger prediction error for the negative percentage error in $F_{10.7}$ than for the positive percentage error. Further investigation of this aspect is beyond the scope of this thesis. Since the forecast error in $F_{10.7}$ during March 2017 is 6.4 % (Table 5.1) which is less than 10 %, it can be concluded that the position error of predicted orbit during March to May, 2017 will be within the limits specified by the values given in Table 5.2 for PROBA-V as there is not much change in its altitude. For GRACE-A, the position error of the predicted orbit is expected to increase during P2. This occurs in spite of the lower forecast error in $F_{10.7}$ (6.4 %) as the altitude of GRACE-A is lower (333 km) than its altitude during P1 (415 km). For applying the orbit prediction method to any arbitrary period, the corresponding forecast error in solar radio flux should be taken into account for realistic position errors of predicted orbits.

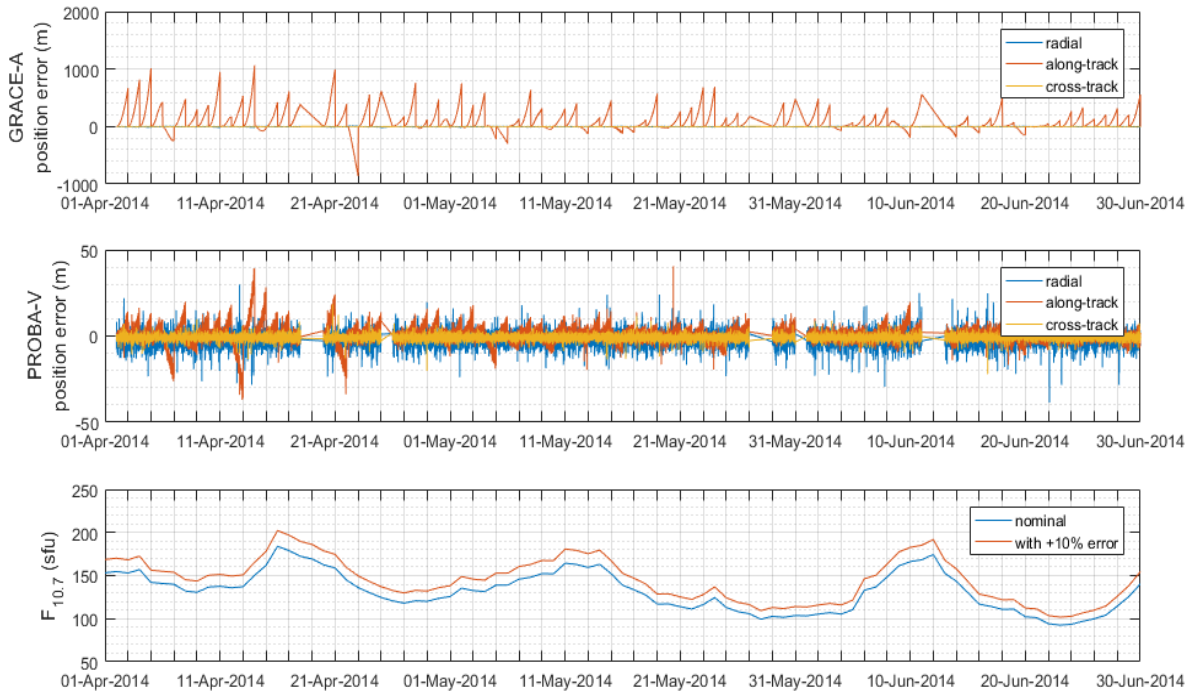

(a) Orbit prediction position errors of GRACE-A (top) and PROBA-V (middle) for +10 % error in the forecast of $F_{10.7}$ (bottom).

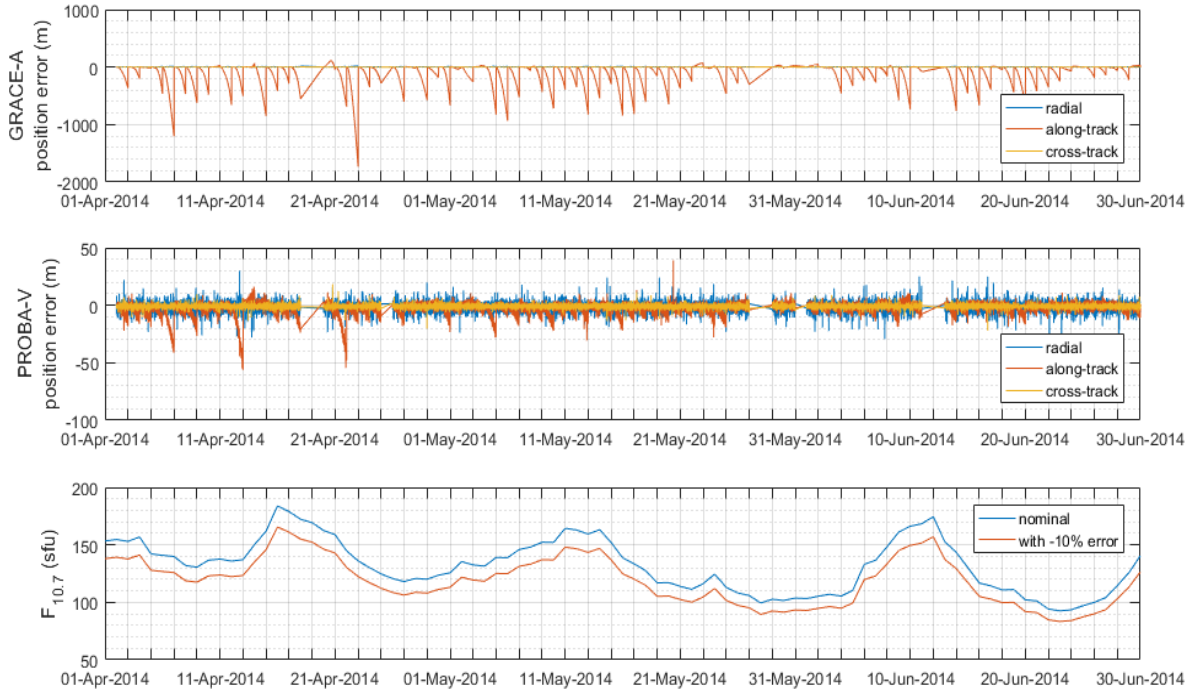

(b) Orbit prediction position errors of GRACE-A (top) and PROBA-V (middle) for -10 % error in the forecast of $F_{10.7}$ (bottom).

Figure 5.2: Orbit prediction position errors of GRACE-A and PROBA-V due to error in the forecast of $F_{10.7}$

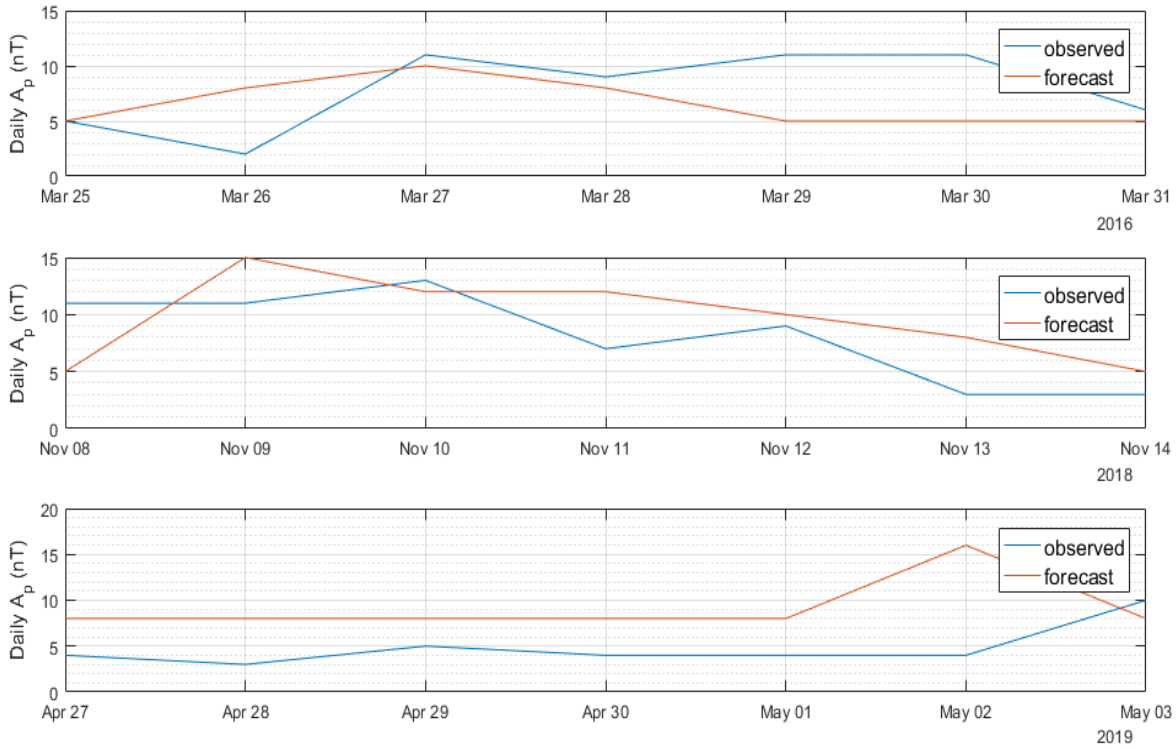

Figure 5.3: Observed and forecast values of the daily A_p index for first 7 forecast days in 2016, 2018 and 2019.

5.2 Effects of error in geomagnetic activity forecast

The method of interpolation and extrapolation described in Section 5.1 can't be used to arrive at predetermined error values for the A_p forecast index. Attempts to do so resulted in unrealistic forecast errors. This is because the A_p index is harder to predict than the $F_{10.7}$ index due to the complexity of the geomagnetic process. Figure 5.3 shows the observed and forecast values of geomagnetic activity in terms of A_p index. The effect of error in A_p forecast on orbit prediction is ascertained by introducing random variations in A_p in the density model throughout the testing period. Both P1 (April - June, 2014) and P2 (March - May, 2017) are considered for testing. Additionally, three successive days during P2 with low levels of geomagnetic activity are chosen for which 4 categories of geomagnetic storms are introduced in the density model to study the effect on orbit prediction.

Effect of random variations in A_p:

For each day of the testing period, a simple random number generator is used to create 600 samples of A_p. During P1 these samples are created based on the mean and standard deviation of 8.8 nT and 6.16 nT, respectively and during P2 these samples are created based the mean and standard deviation of 13.3 nT and 9.31 nT, respectively. The mean and standard deviation of the simulated A_p are chosen based on trial and error to get a distribution of A_p as shown in Figure 5.4. Out of these 600 samples, one value is chosen based on the day of the year corresponding to the prediction arc. This modified A_p is input to the density model which is used for prediction. Figure 5.4 shows the orbit prediction position errors of both satellites due to random variations in A_p forecast during P1 and P2. For both satellites, during P2 the along-track error is the dominant error component. During P1, there are two noticeable peaks in the along-track error of both satellites on April 13 & 22, 2014 which might suggest geomagnetic activity not captured in the A_p properly (Figure 5.4a). Both satellites show peaks in their along-track error on May 28, 2017 for which there is no appreciable change in A_p, suggesting the peaks might be due short term disturbances in the atmosphere, not modelled by A_p index.

Statistics of these predictions are provided in Table 5.3. From the table, it can be observed that the random variations in A_p index don't create much changes to the prediction of PROBA-V. However, for GRACE-A, the random variations in A_p increase the along-track error by a factor of 0.82 during P1 and by a factor of 1.26 during P2.

Effect of geomagnetic storms:

Three days (May 19 - 21, 2017) with low levels of geomagnetic activity are chosen during the period P2. For each of these three days, the value of observed A_p is altered to simulate 4 categories of geomagnetic storms: minor storm ($35 < A_p \leq 59$), moderate storm ($60 < A_p \leq 99$), strong storm ($100 < A_p \leq 159$) and severe storm ($160 < A_p \leq 309$). These values are used in the density model to simulate corresponding density spikes. Figure 5.5 shows orbit prediction along-track errors of both satellites during the different categories of storms. As expected, for GRACE-A the error is maximum for the severe storm and minimum for minor storm on all three days. However, some peculiarities

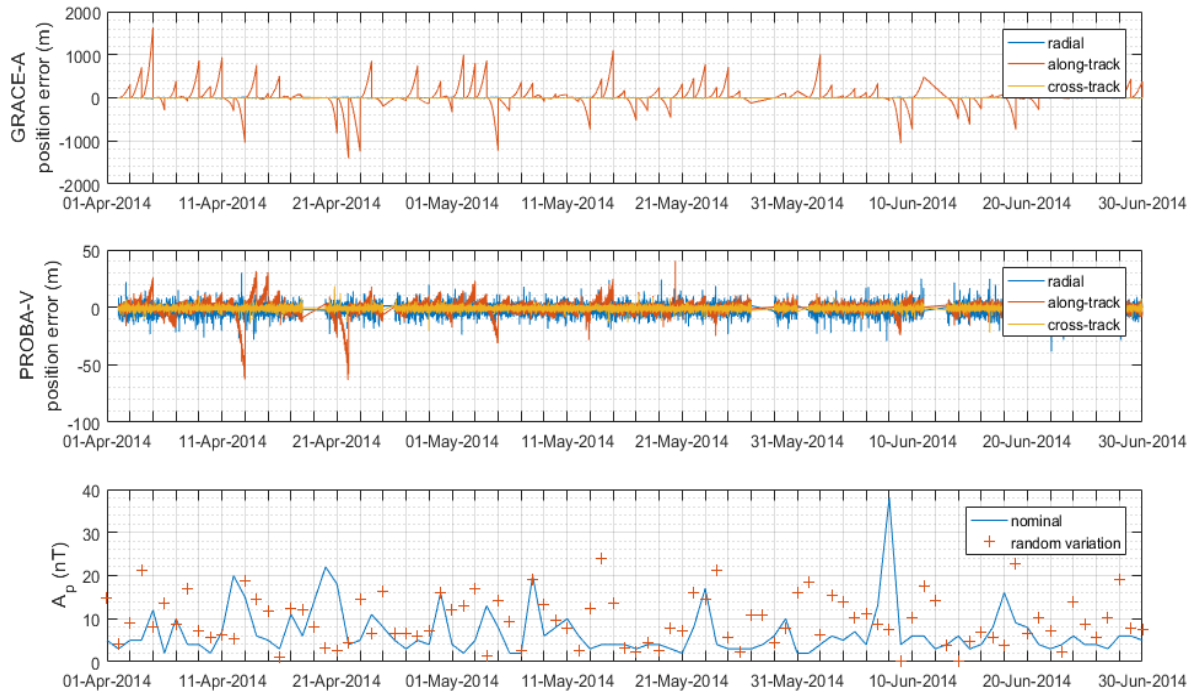

(a) Orbit prediction position errors of GRACE-A (top) and PROBA-V (middle) for random error in the forecast of A_p (bottom) during April - June, 2014.

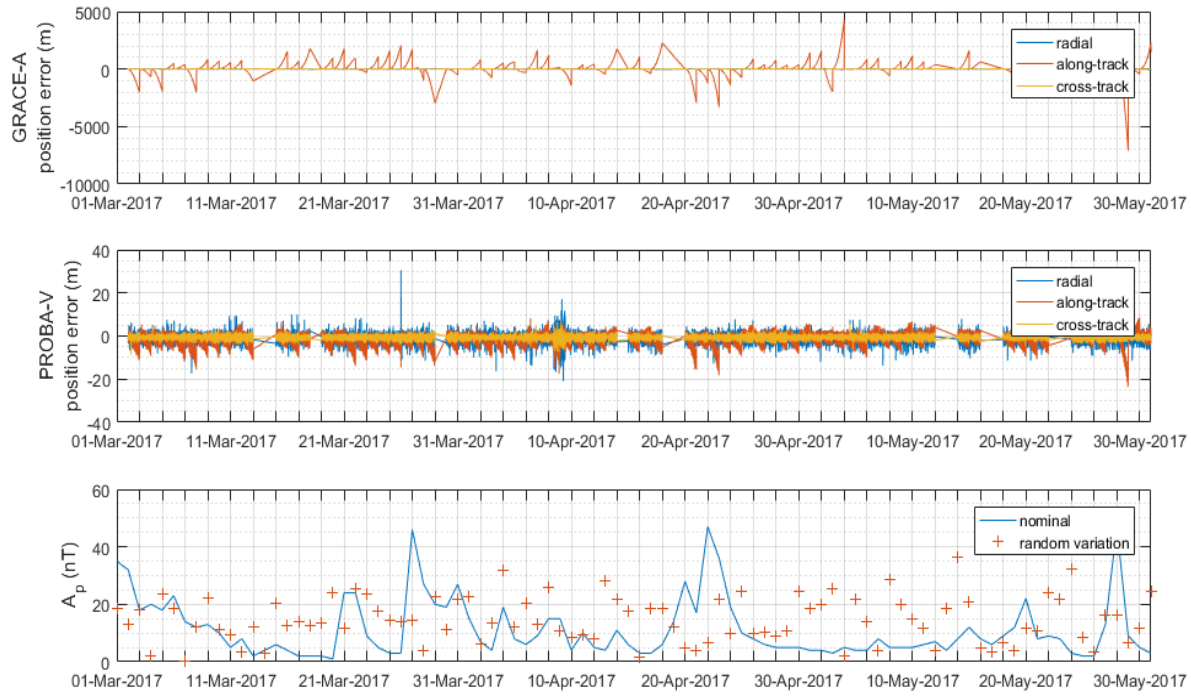

(b) Orbit prediction position errors of GRACE-A (top) and PROBA-V (middle) for random error in the forecast of A_p (bottom) during March - May, 2017.

Figure 5.4: Orbit prediction position errors of GRACE-A and PROBA-V due to random error in the forecast of A_p

Period	Case	Satellite name	Mean of maximum along-track error (m)	3D RMS of predicted orbit (m)
April to June, 2014	Nominal	GRACE-A	243.47	148.80
		PROBA-V	13.30	6.09
	Random variation in A_p	GRACE-A	443.10	255.39
		PROBA-V	14.85	7.30
March to May, 2017	Nominal	GRACE-A	525.71	444.79
		PROBA-V	8.64	4.26
	Random variation in A_p	GRACE-A	1191.40	708.97
		PROBA-V	8.56	4.28

Table 5.3: Change in orbit prediction errors in response to random variation in A_p.

Case	Satellite name	Mean of maximum along-track error (m)	3D RMS of predicted orbit (m)
No storm	GRACE-A	291.04	156.18
	PROBA-V	8.90	4.14
Minor storm ($35 < A_p \leq 59$)	GRACE-A	1328.20	643.53
	PROBA-V	6.52	3.56
Moderate storm ($60 < A_p \leq 99$)	GRACE-A	2081.40	964.58
	PROBA-V	5.43	3.35
Strong storm ($100 < A_p \leq 159$)	GRACE-A	3607.20	1634.40
	PROBA-V	7.70	3.40
Severe storm ($160 < A_p \leq 309$)	GRACE-A	6226.10	2815.10
	PROBA-V	14.85	5.60

Table 5.4: Change in orbit prediction errors in response to geomagnetic storms during May 19 to 21, 2017.

can be observed in the results of PROBA-V. For the case of moderate storm, the along-track error is even smaller than the nominal case. The short period variations seen in the error plot of PROBA-V correspond to the 1 cycle-per-revolution (CPR) nature of drag force. Such variations are difficult to observe in the plot of GRACE-A because of the larger scale of along-track errors. Statistics of these predictions are summarized in Table 5.4. For the case of severe storm, the along-track error of GRACE-A increases by a factor of 20.4 whereas the along-track error of PROBA-V increases by not more than 67 %. The along-track error of PROBA-V during the moderate storm decreases by 39 % compared to the no storm case. This trend is also observed during the minor and the strong storm cases. This peculiarity might indicate that the density model at 800 km altitude does not adequately represent the storm conditions. Investigation in this direction is reserved for future work.

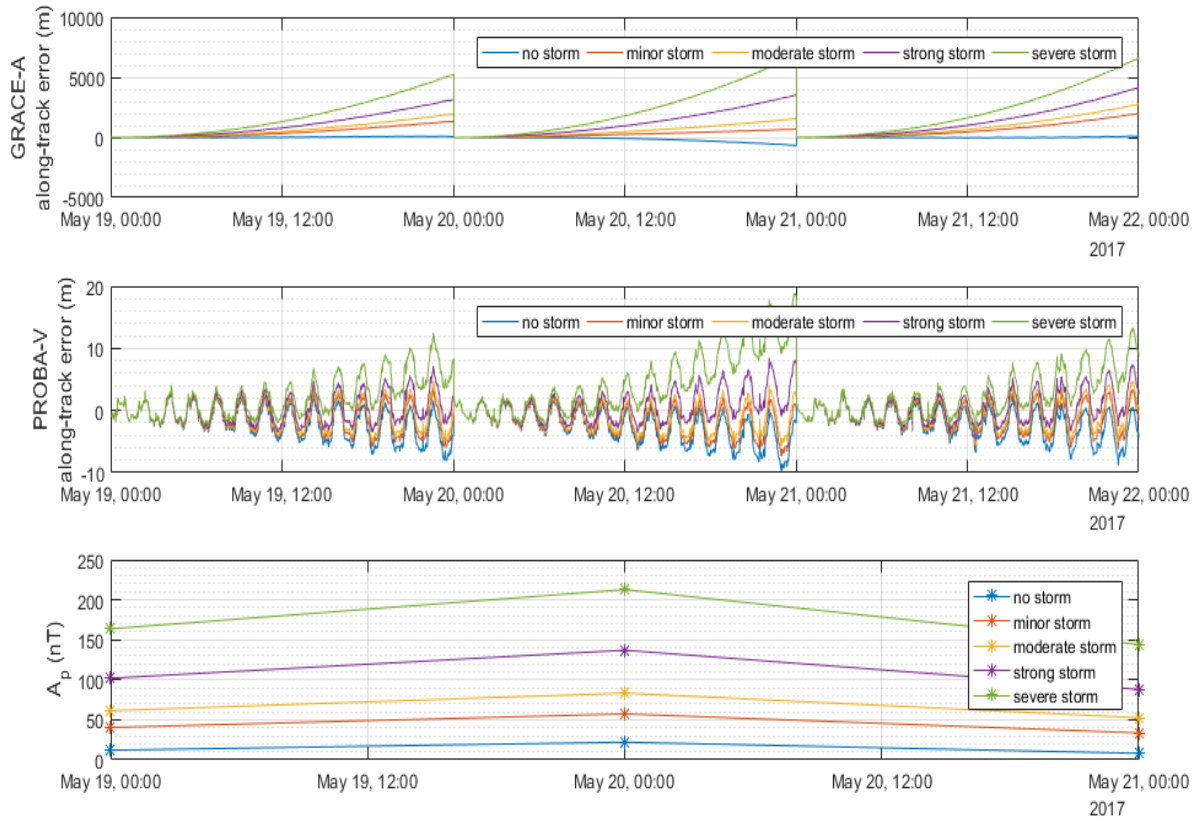

Figure 5.5: Along-track error during orbit prediction of GRACE-A (top) and PROBA-V (middle) during geomagnetic storm conditions in May, 2017 (bottom).

Chapter 6

Optimizing estimation and prediction for computational efficiency of PROBA-V

Computational efficiency in orbit determination is required to produce low latency satellite orbits to meet the science mission objectives of Earth observation satellites such as those used in weather forecasting applications. In case of orbit prediction, computational efficiency is required for autonomous satellite operations which have limited on-board processing power. These include autonomous maintenance of satellite formations for Earth observations missions in LEO [D'Amico et al., 2012].

Jäggi et al. [2007] presents the details and limitations of an efficient reduced dynamic orbit determination technique using piece-wise constant accelerations for CHAMP satellite. Bae et al. [2007] provides an account of processing time and orbit errors with respect to Rapid Science Orbits (RSO) when using different degree and order of the gravity model EIGEN2 for the orbit determination of CHAMP satellite. Montenbruck et al. [2005] used a truncated version (100 x 100) of the GGM01S gravity model to achieve a 20 % reduction in the overall processing time without degrading the accuracy of the orbit determination of GRACE satellite. The Jacchia 71 density model was used to reduce the computational effort compared to the Jacchia 77 model, with a slight reduction in modelling accuracy. Simplifications such as neglection of luni-solar and tidal perturbations were applied for variational equations to further reduce computational effort. The paper also provides an adequate interval length for the estimation of empirical accelerations of GRACE based on a compromise between computational effort, observability and resolution of time varying phenomena. Subject to the conditions given in the paper, the use of least-squares orbit determination software resulted in storage requirements and total operations count up to the second and third power of the estimation arc length, respectively. Levit and Marshall [2011] describes a procedure for obtaining optimum estimation arc length using TLEs for satellites above 800 km altitude to provide improved orbit prediction for 30 days.

This chapter presents methods to improve the computational efficiency of the orbit estimation and prediction of PROBA-V in the interests of Qinetiq Space to cut operating costs. This is achieved by altering the force models and arc lengths used for estimation and prediction with respect to a nominal case of estimation and prediction.

The nominal case for estimation is defined as the estimation carried out using the force models defined in Table 2.2 with the resolution of 1 C_d per day for an arc length of one day. The nominal case for prediction is defined as the prediction carried out using the force models defined in Table 2.2 with the estimated C_d of previous day for an arc length of one day. Throughout this chapter, the chosen solar maximum (April - June, 2014) has been used as it represents the worst case of prediction due to relatively high solar activity. The results from altered the estimations and predictions are compared with the nominal cases using the following metrics: mean maximum position error (3D) of the predicted orbit (computed using Equation (3.1)) and the mean total computation time which is an average of the sum of the time taken for a 24 hour estimation arc and a 24 hour prediction arc throughout the period P1. The computations are carried out on a Linux machine with 62 GB RAM, 3 GHz clock speed and 56 processors. Section 6.1 gives the sensitivity of the force models involved, to the mean total computation time and the prediction error. Section 6.2 presents the results of varying the estimation arc length for various levels of force model complexity and Section 6.3 provides the results of varying the prediction arc length and gives recommendations to achieve computational efficiency while maintaining a reasonable degree of accuracy.

6.1 Force model sensitivity analysis

Sensitivity analysis is carried out by removing or simplifying one force model at a time from the nominal force model while maintaining other force models. Other conditions for estimation and prediction such as the arc length, integrator and stepsize are kept constant. The following alterations of force models were done one at a time for sensitivity analysis: truncating the Earth gravity model (ITU_GRACE 16) from degree and order 50 to degree and order 30, removing luni-solar (third body) perturbation, fixing the value of C_d to 1.85 (mean estimated C_d during P1 as mentioned in Table 3.1) and 1.30 (mean estimated C_d during P2 as mentioned in Table 3.1) separately, instead of estimating the C_d, removing the drag force altogether, removing solid Earth tides and removing solar radiation pressure. With these one at a time alterations, both estimation and prediction were carried out during the period P1.

The results of the sensitivity analysis are shown in Table 6.1. From the table, it can be seen that excluding the solar radiation pressure model has the least effect on the mean total computation time and truncating to the Earth gravity 30 x 30 model has the most effect on the mean total computation time. Excluding the solid Earth tide model and the drag force model has the least and the most effect on the mean maximum position error (3D) of predicted orbit, respectively. However, when inspecting a combination of both the metrics, the following can be observed: excluding the third body acceleration model has the least effect on the computation time and the most effect on the maximum prediction error. This is an undesirable effect and is indicated in red colour in the Table 6.1. Truncating to the Earth gravity 30 x 30 model has the most effect on the computation time and the least effect on the maximum prediction error. This is a desirable effect and is indicated in green colour in the Table 6.1. This suggests that the Earth gravity model can be truncated to degree and order 30 to gain a 50 % reduction in computation time for a 66 % increase in the maximum prediction error and the third body acceleration model should be included for all further analysis concerning the computational efficiency.

Force model scenario	Mean total computation time (min)	Mean maximum position error (3D) of predicted orbit (m)	3D RMS of position error (m)	
			Predicted orbit	Estimated orbit
Nominal	7.05	24.10	6.27	3.63
No solid Earth tides	6.65	25.14	7.10	3.74
No solar radiation pressure	6.78	26.36	7.61	3.81
Fixed C_d (1.85)	6.46	29.58	12.12	3.70
Fixed C_d (1.30)	6.47	46.11	24.73	3.91
Earth gravity 30 x 30	3.51	40.21	17.17	3.95
No third body acceleration	6.50	55.30	26.79	8.25
No drag	5.05	113.44	63.77	5.38

Table 6.1: Sensitivity of mean total computation time and prediction error of PROBA-V to force models during April - June, 2014.

6.2 Effect of varying estimation arc length

In this section, the effect of varying the estimation arc length on the computation time and maximum prediction error is studied. In these investigations, the prediction arc length is kept fixed to one day. Based on the results shown in the Table 6.1, the complexity of the force model is gradually reduced so as to achieve a larger decrease in the computation time at the cost of a slower increase in the mean maximum position error (3D) of predicted orbit. Initially the strategy of using reduced navigation data density (i.e. one observation data point for every 2 or more minutes instead of 1 minute (Table 2.1)) for estimation was considered to test the computational efficiency. However, from Qinetiq Space point of view, this is not interesting as the company prefers not to use reduced navigation data density for its satellite operations. The company is more interested on the effects of using the same navigation data density but with reduced arc length such as 6 hours instead of 24 hours. Hence, the following combinations of force models are considered for estimation arc lengths of 24 hours, 18 hours, 12 hours, 6 hours and 1.75 hours (one orbit of PROBA-V):

- Nominal force model.
- Nominal force model + (No solid Earth tides + no solar radiation pressure (SRP)) + fixed C_d. This means that the solid Earth tides and solar radiation pressure are removed from the nominal force model while the drag model uses a fixed value of C_d.
- Nominal force model + (No solid Earth tides + no solar radiation pressure (SRP))

+ fixed C_d + Earth gravity field of order and degree 30 (g30by30). This means that the solid Earth tides and solar radiation pressure are removed from the nominal force model. The value of C_d is fixed and the Earth gravity model is reduced to degree and order 30.

- Nominal force model + (No solid Earth tides + no solar radiation pressure (SRP) + no drag) + Earth gravity field of order and degree 30 (g30by30). This means that the solid Earth tides, solar radiation pressure and drag force are removed from the nominal force model while the Earth gravity model is reduced to degree and order 30.

All the force model combinations are applied for the estimation and prediction process with varying estimation arc lengths as mentioned and the results are tabulated in Tables 6.2, 6.3 and 6.4. The value of C_d in fixed C_d force model is set to 1.57 which is the mean of the mean C_d value estimated during the solar maximum and minimum conditions. This enables the results to be applicable for varying solar flux conditions. From these tables, it can be concluded that the results pertaining to the 6 & 1.75 hour estimation arc lengths for the nominal force model should be taken with caution as they produce negative and unrealistic values of C_d during the estimation process.

From the Table 6.2, it can be seen that for a given force model combination, the estimation error (3D RMS of estimated orbit) decreases with the estimation arc length. This decrease is most significant for the least complex model (i.e. Nominal + (no tides + no SRP + no drag) + g30by30). This is because, once the initial state and force model parameters are estimated using the least-squares technique, the state vector for the following epochs is obtained through propagation using the force models of the estimation process. Hence, shorter arcs give better estimation results for the same force model complexity [Bae et al., 2007]. This is illustrated in Figure 6.1 which gives a plot of the error norm for a single day (April 10, 2014). Similar result is expected in a plot of the along-track error for varying estimation arc lengths. This is because the along-track error is dominating component of the position error. The results from Tables 6.3 and 6.4 are plotted in Figure 6.2. From the Figure 6.2a, it can be concluded that the least complex model (i.e. Nominal + (no tides + no SRP + no drag) + g30by30) has the least mean total computation time corresponding to the estimation arc length of 1.75 hours. However, for the same estimation arc length, Figure 6.2b shows a change in the trend of the mean maximum position error (3D) of the predicted orbit. The prediction error increases when the estimation arc length is shorter than 6 hours in spite of the corresponding reduction in the estimation error (Table 6.2). This might be due to the differences in the last state vector between the results of the 6 hour and 1.75 hour estimation, that is used as input to the prediction. For estimation arc lengths shorter than 6 hours, the geometric density of the tracking information is not sufficient to give good estimation and subsequently good prediction results. Hence, it can be concluded that, for a fixed prediction arc length of one day, the least complex force model with an estimation arc length of 6 hours is the most efficient with a mean total computation time of 0.7031 minutes and a mean maximum position error (3D) of 74.3453 m for the predicted orbit, which is still less than the 125 m requirement.

Force model combinations	**3D RMS of estimated orbit (m)**				
	24 hour arc	18 hour arc	12 hour arc	6 hour arc	1.75 hour arc
Nominal force model.	3.63	3.58	3.57	3.58 (negative and erratic C_d)	3.38 (negative and erratic C_d)
Nominal +(no tides + no SRP) + fixed C_d	4.08	3.89	3.76	3.72	3.54
Nominal +(no tides + no SRP) + fixed C_d + g30by30	4.59	4.30	3.94	3.75	3.55
Nominal + (no tides + no SRP + no drag) + g30by30	6.00	4.78	3.97	3.66	3.44

Table 6.2: 3D RMS of estimated orbit of PROBA-V for reduced force model complexity and various estimation arc lengths during April to June, 2014.

Force model combinations	**Mean total computation time for 1 day (min)**				
	24 hour arc	18 hour arc	12 hour arc	6 hour arc	1.75 hour arc
Nominal force model.	7.05	4.87	3.49	2.07 (negative and erratic C_d)	1.04 (negative and erratic C_d)
Nominal +(no tides + no SRP) + fixed C_d	6.10	4.74	3.38	2.00	1.00
Nominal +(no tides + no SRP) + fixed C_d + g30by30	3.30	2.59	1.86	1.10	0.57
Nominal +(no tides + no SRP + no drag) + g30by30	1.95	1.54	1.14	0.70	0.40

Table 6.3: Mean total computation time of PROBA-V for reduced force model complexity and various estimation arc lengths during April to June, 2014.

Force model combinations	**Mean maximum position error (3D) of predicted orbit (m)**				
	24 hour arc	18 hour arc	12 hour arc	6 hour arc	1.75 hour arc
Nominal force model.	24.10	24.60	25.54	42.11 (negative and erratic C_d)	2088.00 (negative and erratic C_d)
Nominal +(no tides + no SRP) + fixed C_d	41.58	39.29	36.95	35.52	54.21
Nominal +(no tides + no SRP) + fixed C_d + g30by30	43.24	40.49	39.93	40.70	60.89
Nominal +(no tides + no SRP + no drag) + g30by30	117.10	101.18	86.24	74.34	97.44

Table 6.4: Mean maximum position error (3D) of the predicted orbit of PROBA-V for reduced force model complexity and various estimation arc lengths during April to June, 2014.

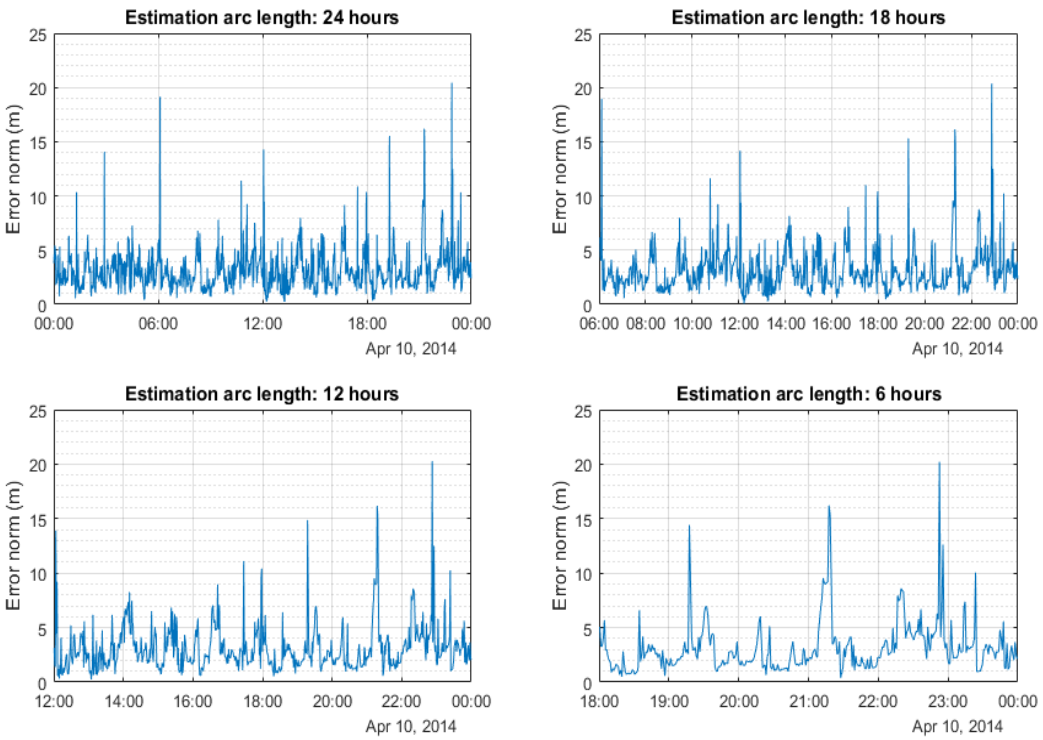

(a) Norm of the position error of the estimated orbit of PROBA-V (vs) estimation arc lengths on April 10, 2014 for nominal force model.

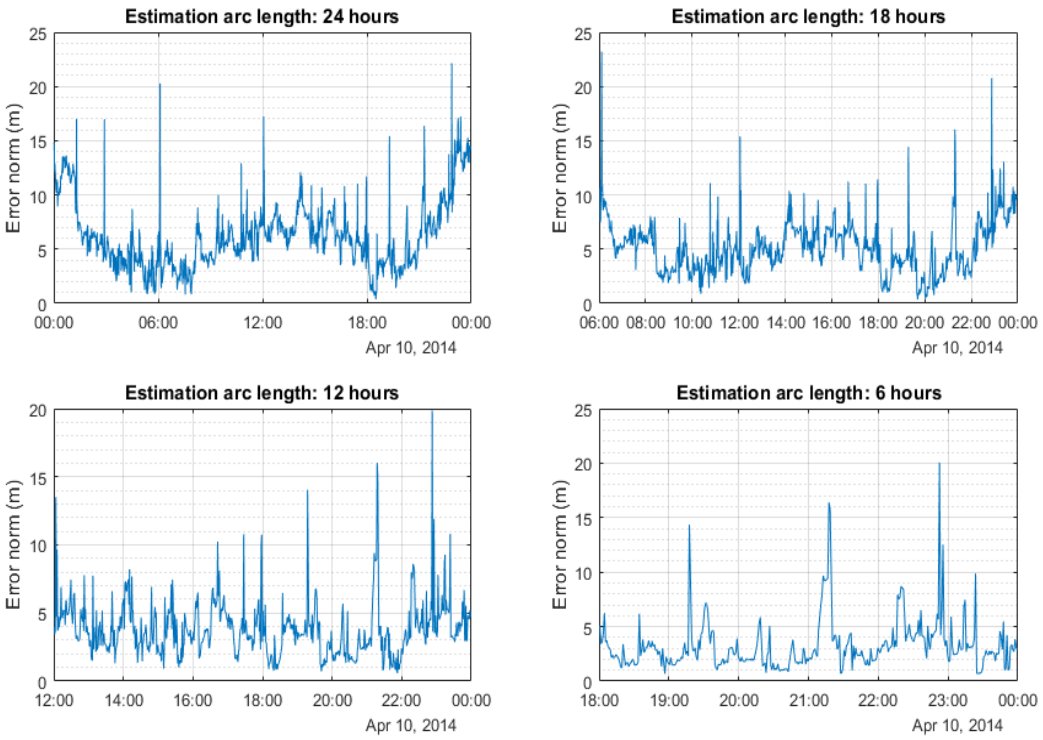

(b) Norm of the position error of the estimated orbit of PROBA-V (vs) estimation arc lengths on April 10, 2014 for nominal + (no tides + no SRP + no drag) + g30by30 force model.

Figure 6.1

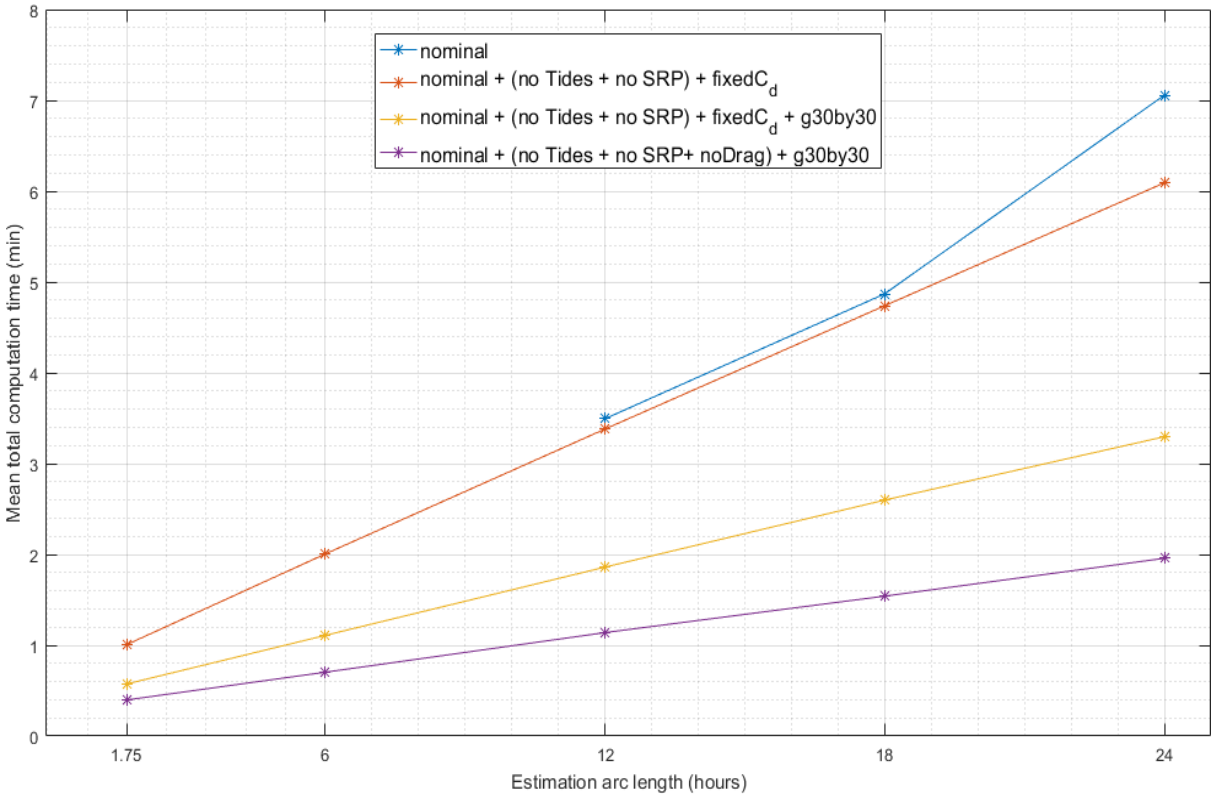

(a) Variation of mean total computation time of PROBA-V with estimation arc length during April - June, 2014 for prediction arc length of one day .

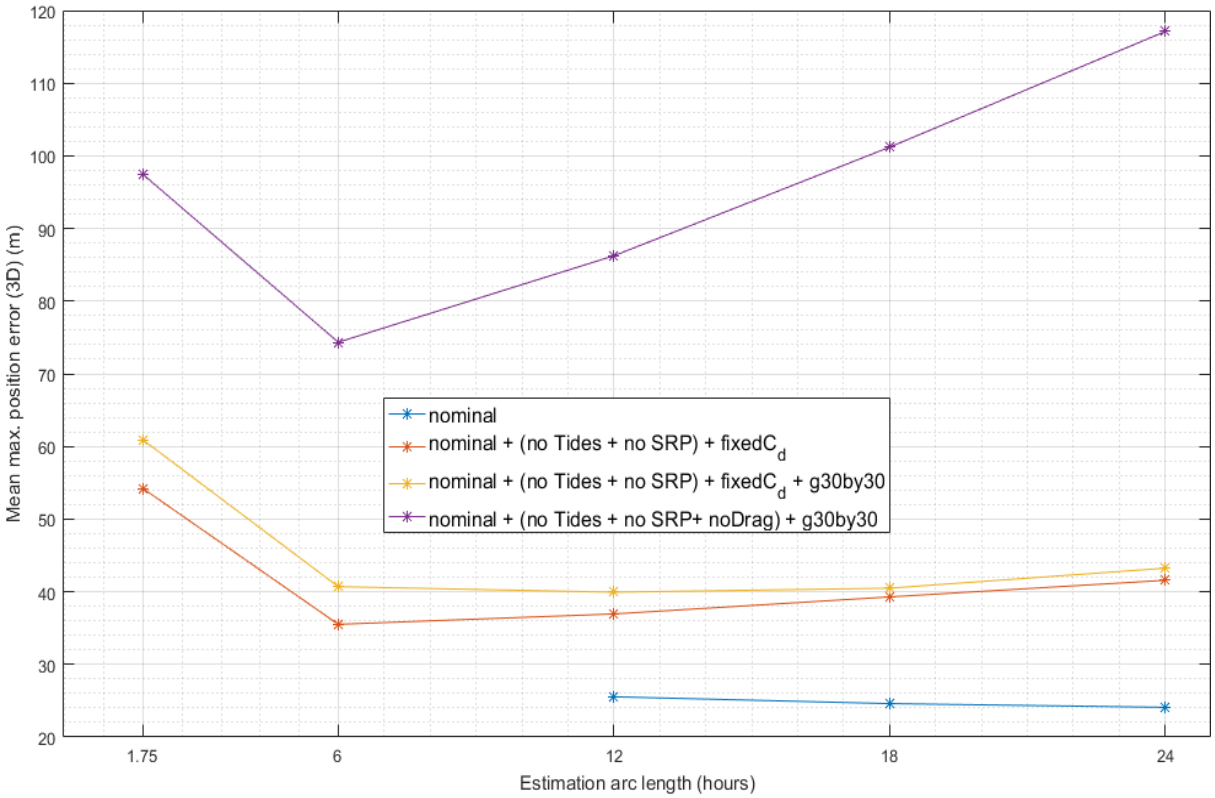

(b) Variation of mean maximum position error (3D) of predicted orbit of PROBA-V with estimation arc length during April - June, 2014 for prediction arc length of one day.

Figure 6.2

Estimation arc length	**Force model combinations**	**Mean total computation time (min)**		
		1 day	2 days	3 days
12 hours	Nominal force model.	3.49	4.06	4.63
6 hours	Nominal +(no tides + no SRP) + fixed C_d (1.57) + g30by30	1.10	1.38	1.65
6 hours	Nominal +(no tides + no SRP + no drag) + g30by30	0.70	0.92	1.13

Table 6.5: Mean total computation time of PROBA-V with various force model complexity and different prediction arc lengths during April to June, 2014.

Estimation arc length	**Force model combinations**	**Mean maximum position error (3D) of predicted orbit (m)**		
		1 day	2 days	3 days
12 hours	Nominal force model.	25.54	43.76	84.63
6 hours	Nominal +(no tides + no SRP) + fixed C_d (1.57)+ g30by30	40.70	76.04	132.39
6 hours	Nominal +(no tides + no SRP + no drag) + g30by30	74.34	240.64	506.36

Table 6.6: Mean maximum position error (3D) of the predicted orbit of PROBA-V with various force model complexity and different prediction arc lengths during April to June, 2014.

6.3 Effect of prediction arc length variation

This section presents the results of the study on varying prediction arc length and its effect on the mean total computation time and mean maximum position error (3D) of the predicted orbit. The estimation output, including the computation time, from the following three force model combinations mentioned in Section 6.2 were used as input to the prediction: nominal force model with estimation arc length of 12 hours, least complex force model with estimation arc length of 6 hours and the second least complex force model (i.e. nominal + (no tides + no SRP) + fixed C_d (1.57) + g30by30) with estimation arc length of 6 hours. For each of these combinations, three prediction arc lengths were tested: one day, two days and three days. The results of these predictions are summarized in Tables 6.5 and 6.6 and plotted in Figure 6.3.

From Figure 6.3a, it can be observed that the mean total computation time increases linearly with the prediction arc length. Among the three force model combinations, as expected, the nominal force model with 12 hour estimation arc has the steepest rise of computation time with a maximum of 4.63 minutes and the least complex force model has the most gradual rise of computation time with a maximum of 1.13 minutes at the end of 3 days. From the Figure 6.2b, it can be observed that the mean maximum

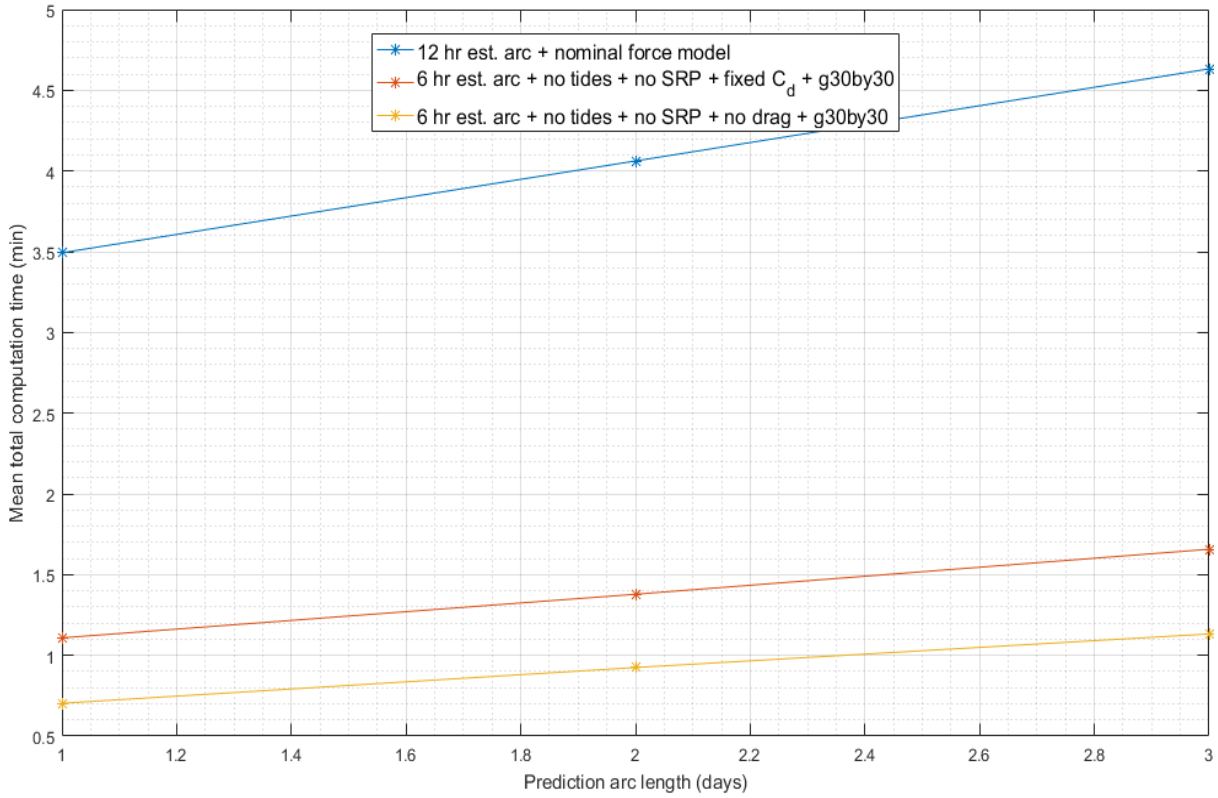

(a) Variation of mean total computation time of PROBA-V with prediction arc length during April - June, 2014.

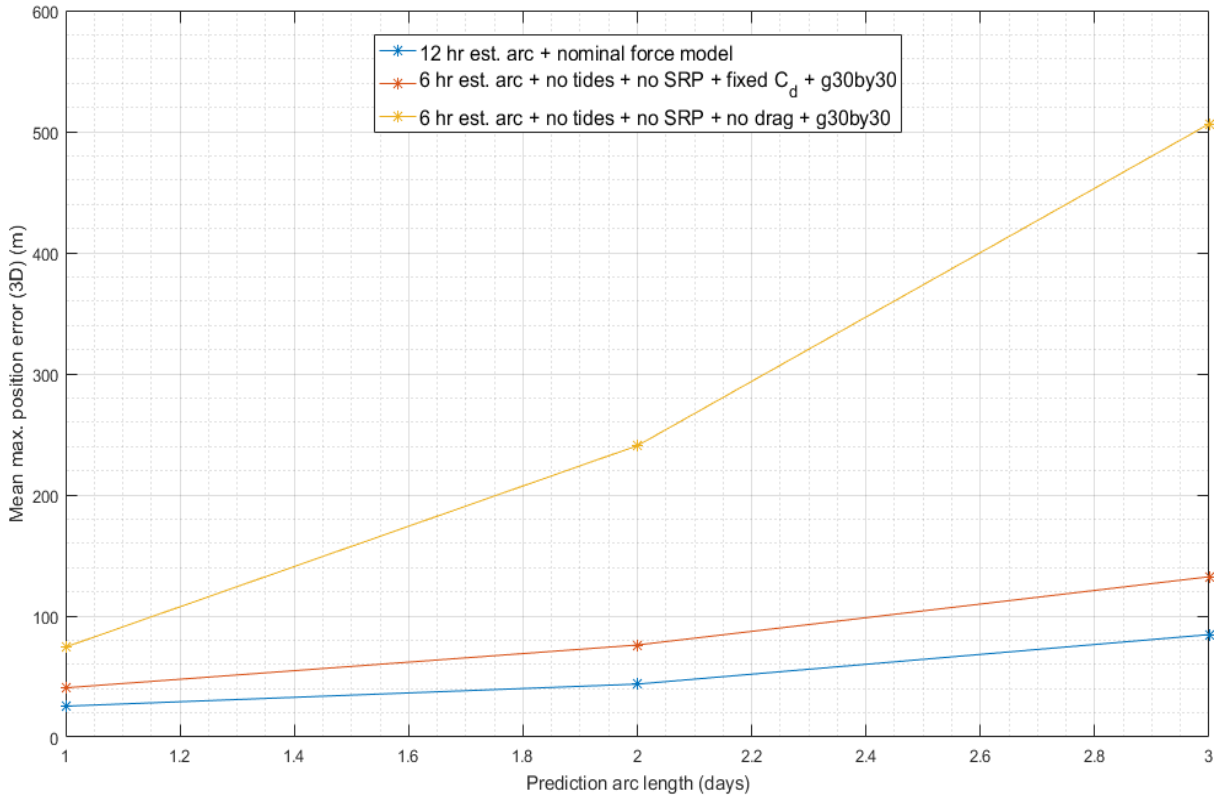

(b) Variation of mean maximum position error (3D) of predicted orbit of PROBA-V with prediction arc length during April - June, 2014.

Figure 6.3

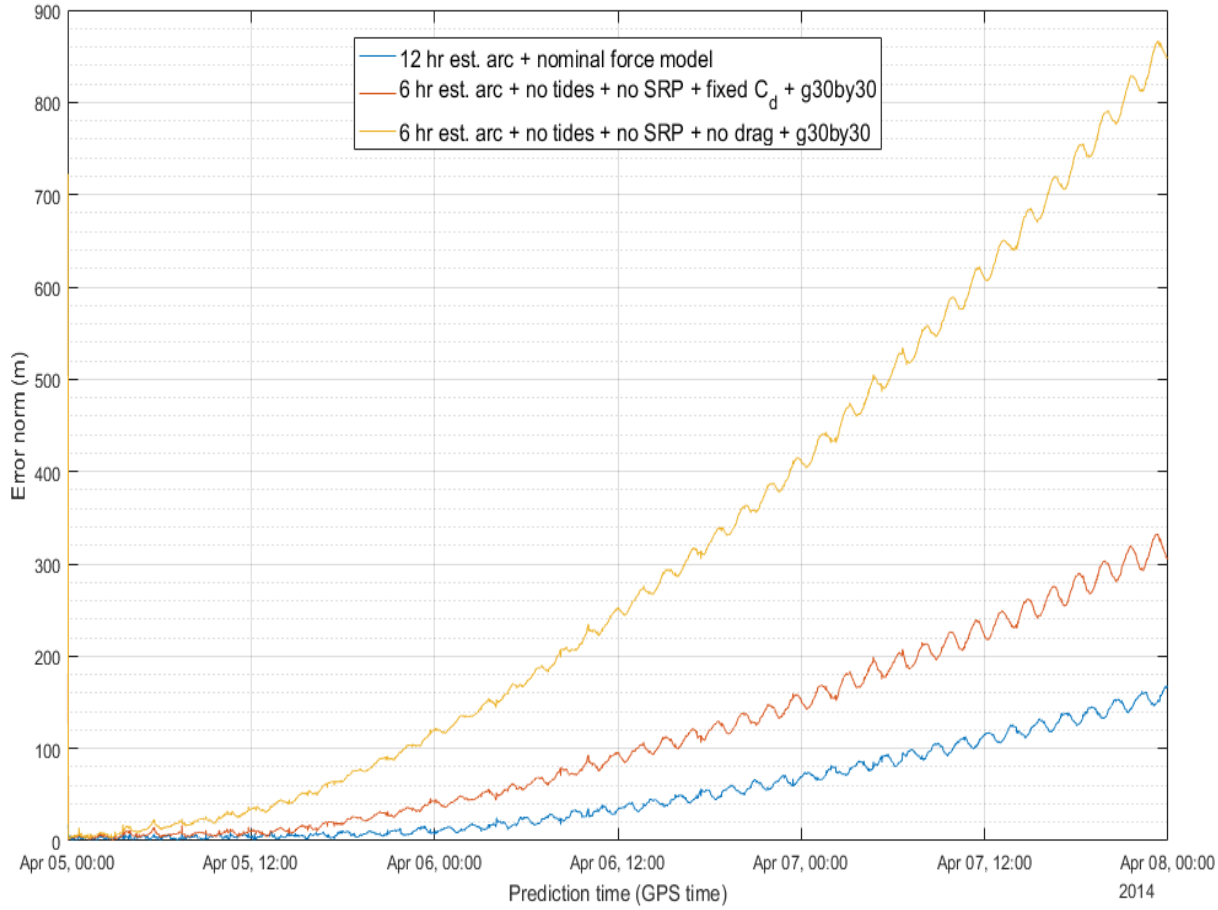

Figure 6.4: Norm of the position error of the predicted orbit of PROBA-V (vs) prediction time during April 5 - 7, 2014.

position error (3D) of predicted orbit varies non-linearly with the prediction arc length. The variation can be approximated by a second order polynomial. As expected, the least complex force model results in the largest maximum prediction error of 506.36 m after 3 days and the nominal force model results in the smallest maximum prediction error of 84.63 m after 3 days. Figure 6.4 shows the variation of the norm of the position error of the predicted orbit with the prediction arc length during the period April 5 - 7, 2014 as a representative prediction. The short period variations observed in the norm of prediction error correspond to the fluctuations caused by the 1 CPR nature of the drag force.

In conclusion, the least complex force model (i.e. nominal + (no tides + no SRP + no drag) + g30by30) with 6 hour estimation arc length is the most computationally efficient force model combination for the prediction arc length of one day. For prediction arc lengths exceeding one day and up to 3 days, it is recommended to use the second least complex force model (i.e. nominal + (no tides + no SRP) + fixed C_d (1.57) + g30by30) with 6 hour estimation arc length to stay within the limits of acceptable prediction error considering a margin of 6 %. It is to be noted that the computational strategies discussed so far must be considered along with the error in space weather forecast (Chapter 5) for reliable orbit prediction.

Chapter 7

Conclusions and Outlook

Emphasis of accurate satellite orbit prediction for collision avoidance between space assets and debris as well as for autonomous maintenance of formation flying missions in LEO has been provided. Methods such as using the TLE and the associated SGP4 propagator for the orbit prediction assessment of the LEO objects and in-track & cross-track stationkeeping to compensate for orbital decay of the very low LEO satellites due to the drag force are briefly discussed. In the context of accurate orbit prediction, a need for improved drag force modelling of SAOCOM-CS satellite is described in the along-track maintenance scheme proposed by Qinetiq Space. To carry out its mission objectives, the SAOCOM-CS & SAOCOM-1B, the master satellite, configuration should have a maximum along-track separation of 7 km and a minimum along-track separation of 5 km, thus making the along-track deadband as 2 km. This led to the following requirement for this thesis: **the norm of the maximum position error in orbit propagation of SAOCOM-CS should be less than** 125 **m after one day of propagation**. Based on this requirement, an orbit prediction strategy was developed and tested with the GRACE and PROBA-V satellites under various conditions of solar activity.

Inputs to the satellite orbit prediction, such as the initial state and the drag scale factor (C_d) are obtained by the precise orbit determination of GRACE-A and PROBA-V satellites using the GPS state vector data as measurement and force models in the batch least-squares estimator. A cannonball model represents the satellite shape and NRLMSISE-00 has been used for density modelling for orbit determination and prediction which are carried out with the TUDAT software. Both single and multiple C_d per day estimation schemes have been used and for each of these schemes different methods are used to determine the predicted drag scale factor. Two different periods of solar activity are used for orbit determination and prediction: P1 (April - June, 2014 with high solar activity) and P2 (March - May, 2017 with low solar activity). The optimum method of determining the predicted drag scale factor depends on the satellite, the solar activity period and the prediction metric which is defined as the RMS of the differences between the predicted and the estimated drag scale factor of each day throughout the period considered.

Orbit determination with the estimation of one drag scale factor per day and prediction using the estimated C_d of the previous day proves to be sufficient for PROBA-V. The orbit determination of PROBA-V results in 3D RMS error of 3.63 m and 2.34 m during P1 and P2, respectively for an estimation arc length of one day. Orbit prediction

of PROBA-V results in mean maximum position errors of 24.10 m and 13.30 m during P1 and P2, respectively for a prediction arc length of one day. Though prediction using the mean estimated C_d of the previous week gives slightly better results during P2, it is not recommended due to a higher computational load involved in performing orbit determination for 7 days. Orbit determination of GRACE-A with the estimation of 4 drag scale factors per day results in 3D RMS error of 2.05 m and 5.81 m during P1 and P2, respectively for an estimation arc length of one day. The increased error during P2 can be attributed to the lower altitude of GRACE-A which was nearing its end of life-time. Best results for orbit prediction of GRACE-A are obtained when the results of 4 C_d per day estimation are used in prediction along with the last estimated C_d of the previous day. This results in a mean maximum position error of 243.50 m and 526.00 m during P1 and P2, respectively for a prediction arc length of one day. Though estimation of 8 C_d per day improves the 3D RMS during P1 and P2, it does not give better results for orbit prediction due to the unrealistic C_d output compared to 4 C_d per day estimation. A rule of thumb analysis using the linear and exponential interpolation with the prediction results of GRACE-A and PROBA-V shows the maximum position error in the orbit of SAOCOM-CS to be between 40 and 75 m for a prediction arc length of one day, which satisfies the requirement of this thesis.

It is recommended to focus the future efforts towards improving the prediction accuracy of GRACE-A on employing a more accurate geometry model of the satellite with the use of accurate satellite orientation through attitude modelling or star sensor data and a more realistic gas-surface interaction model. This is because the satellite specific drag coefficient is also sensitive to the satellite length-to diameter ratio. For very long satellites the sides of the spacecraft are subject to random thermal motions of the thermosphere as well as the on-coming particles [Marcos et al., 2010]. Regarding the satellite geometry, March et al. [2019] provides the differences between using a panel model [Bettadpur, 2012] and a 3D model obtained using SPARTA simulator, for the density retrieval using GRACE. Density estimates using the high fidelity 3D model turned out to be 5 % higher than the estimates using the panel model. Since this thesis uses a cannonball model, upgrading the geometry to either of the models mentioned above should improve the prediction accuracy. Statistics of the orbit estimation with 4 C_d per day for GRACE-A and 1 C_d per day for PROBA-V show a change of 17.75 % and 29.7 %, respectively in the mean estimated C_d between P1 and P2. Since the satellite specific parameters don't change between P1 and P2, this change in the mean estimated C_d shows the inadequacy of the NRLMSISE-00 model in characterizing the density variations due to solar activity. Hence, an analysis of the estimated drag scale factors of these two satellites can be used in the future towards the calibration of the density model. Including the ocean tides model is also expected to improve the accuracy of the orbit prediction process.

The impact of the error in the forecast of space weather indices on the orbit prediction has been investigated. Both positive and negative forecast errors in $F_{10.7}$ are used to test the prediction error variation. For a -10 % error in $F_{10.7}$, PROBA-V shows a maximum of 2.5 m increase in the along-track error and GRACE-A shows a 61 % increase in the along-track error during high solar activity. Both satellites show a larger prediction error for the negative forecast error in $F_{10.7}$ than for the same magnitude of positive forecast error. This aspect requires further investigation. For random variations in A_p, the orbit prediction of PROBA-V is not affected and for GRACE-A, the along-track error increases by a factor of 0.82 during P1 and 1.26 during P2. For a severe geomagnetic

storm in P2, the along-track error of GRACE-A increases by a factor of 20.4 and that of PROBA-V increases by not more than 67 %. Interestingly, the error in the orbit prediction of PROBA-V decreases by 39 % during a moderate storm. This peculiarity is also open for future investigation. Combinations of reduced force model complexity, reduced estimation arc length and increased prediction arc length are used to optimize the estimation and prediction for the computational efficiency of PROBA-V. For a prediction arc length of one day, the force model comprising Earth gravity field of degree and order 30 of the model ITU_GRACE 16 with luni-solar perturbations and devoid of atmospheric drag, solar radiation pressure and tidal forces along with a 6 hour estimation arc length is the most computationally efficient combination. For prediction arc lengths between one and 3 days, it is recommended to include the atmospheric force with a constant drag scale factor of 1.57 to the force model and the estimation arc length combination mentioned above to stay within the limit (125 m) of acceptable prediction error.

Bibliography

Charles Acton, Nathaniel Bachman, William M Folkner, and James Hilton. SPICE as an IAU recommendation for planetary ephemerides. *IAU General Assembly*, 22, 2015.

Tae-Suk Bae, Dorota Grejner-Brzezinska, and Jay Hyoun Kwon. Efficient LEO dynamic orbit determination with triple differenced GPS carrier phases. *The Journal of Navigation*, 60(2):217–232, 2007.

Christiane Berger, Richard Biancale, M Ill, and F Barlier. Improvement of the empirical thermospheric model DTM: DTM94–a comparative review of various temporal variations and prospects in space geodesy applications. *Journal of Geodesy*, 72(3):161–178, 1998.

Nicolas Bernard, Luc Maisonobe, Lucian Barbulescu, Petre Bazavan, Sorin Scortan, Paul J Cefola, Massimo Casasco, and Klaus Merz. Validating Short Periodics Contributions in a Draper Semi-Analytical satellite theory implementation: The OREkit example. *ESA, January*, 2015.

Srinivas Bettadpur. Product specification document (CSR-GR-03-02). *Center for Space Research, The University of Texas at Austin*, 2012.

Gerald J Bierman. *Factorization methods for discrete sequential estimation*. Courier Corporation, 2006.

Bruce Bowman, W Tobiska, and Frank Marcos. A new empirical thermospheric density model JB2006 using new solar indices. In *AIAA/AAS Astrodynamics Specialist Conference and Exhibit*, pages 6166–6187, 2006.

Bruce Bowman, W Kent Tobiska, Frank Marcos, Cheryl Huang, Chin Lin, and William Burke. A new empirical thermospheric density model JB2008 using new solar and geomagnetic indices. In *AIAA/AAS Astrodynamics specialist conference and exhibit*, pages 6438–6457, 2008.

S Bruinsma, G Thuillier, and F Barlier. The DTM-2000 empirical thermosphere model with new data assimilation and constraints at lower boundary: accuracy and properties. *Journal of atmospheric and solar-terrestrial physics*, 65(9):1053–1070, 2003.

Kelley Case, Gerhard Kruizinga, and Sienchong Wu. GRACE level 1B data product user handbook. *JPL Publication D-22027*, 2002.

GE Cook. The effect of aerodynamic lift on satellite orbits. *Planetary and Space Science*, 12(11):1009–1020, 1964.

Simone D'Amico, J-S Ardaens, and Robin Larsson. Spaceborne autonomous formation-flying experiment on the PRISMA mission. *Journal of Guidance, Control, and Dynamics*, 35(3):834–850, 2012.

Malcolm Davidson, Nicolas Gebert, B Carnicero Dominguez, Franco Fois, and Pierluigi Silvestrin. SAOCOM-CS: a passive companion mission to SAOCOM for single-pass L-band SAR bistatic interferometry and tomography. In *Proceedings of IGARSS*, 2014.

E Doornbos and H Klinkrad. Modelling of space weather effects on satellite drag. *Advances in Space Research*, 37(6):1229–1239, 2006.

Eelco Doornbos. *Thermospheric density and wind determination from satellite dynamics*. Springer Science & Business Media, 2012.

Eelco Doornbos, Heiner Klinkrad, Remko Scharroo, and Pieter Visser. Thermosphere density calibration in the orbit determination of ERS-2 and Envisat. In *Proceedings of ENVISAT symposium, Montreux, ESA SP-636*, 2007.

JT Emmert. Thermospheric mass density: A review. *Advances in Space Research*, 56(5): 773–824, 2015.

Tim Flohrer, Holger Krag, and Heiner Klinkrad. Assessment and categorization of TLE orbit errors for the US SSN catalogue. *Risk*, 8(9):10–11, 2008.

Michael Francois, Stefano Santandrea, Karim Mellab, Davy Vrancken, and Jorg Versluys. The PROBA-V mission: the space segment. *International Journal of Remote Sensing*, 35(7):2548–2564, 2014.

K Gantois, F Teston, O Montenbruck, P Vuilleumier, PVD Braembussche, and M Markgraf. PROBA-2 mission and new technologies overview. In *Small Satellite Systems and Services-The 4S Symposium*, pages 25–29. European Space Agency, 2006.

IK Harrison and GG Swinerd. A free molecule aerodynamic investigation using multiple satellite analysis. *Planetary and space science*, 44(2):171–180, 1996.

Alan E Hedin. MSIS-86 thermospheric model. *Journal of Geophysical Research: Space Physics*, 92(A5):4649–4662, 1987.

Jaap Herman. Balancing, turning, saving special AOCS operations to extend the GRACE mission. In *SpaceOps 2012*, page 1275114. 2012.

LG Jacchia. Atmospheric models in the region from 110 to 2000 km. *Caspar International Reference Atmosphere (CIRA) 1972*, pages 227–340, 1972.

Luigi G Jacchia and Jack Slowey. Accurate drag determinations for eight artificial satellites: atmospheric densities and temperatures. *Smithsonian Contributions to Astrophysics*, 1963.

Luigi Giuseppe Jacchia. New static models of the thermosphere and exosphere with empirical temperature profiles. *SAO Special Report*, 313, 1970.

Adrian Jäggi, Gerhard Beutler, Heike Bock, and Urs Hugentobler. Kinematic and highly reduced-dynamic LEO orbit determination for gravity field estimation. In *Dynamic Planet*, pages 354–361. Springer, 2007.

Adrian Jäggi, Heike Bock, and Rune Floberghagen. GOCE orbit predictions for SLR tracking. *GPS solutions*, 15(2):129–137, 2011.

Michael Kirschner, Oliver Montenbruck, and Srinivas Bettadpur. Flight dynamics aspects of the GRACE formation flying. In *2nd International Workshop on Satellite Constellations and Formation Flying*, pages 19–20, 2001.

Philip Knocke, J Ries, and B Tapley. Earth radiation pressure effects on satellites. In *Astrodynamics Conference*, page 4292, 1988.

K Kumar, Y Abdulkadir, PWL van Barneveld, F Belien, S Billemont, E Brandon, M Dijkstra, D Dirkx, F Engelen, D Gondelach, et al. Tudat: a modular and robust astrodynamics toolbox. In *5th International Conference on Astrodynamics Tools and Techniques (ICATT 2012)*, 2012.

Kurt Lambeck. *Geophysical geodesy*. Clarendon Oxford, 1988.

Richard B Langley. Dilution of precision. *GPS world*, 10(5):52–59, 1999.

Kristine M Larson, Neil Ashby, Christine Hackman, and Willy Bertiger. An assessment of relativistic effects for low Earth orbiters: the GRACE satellites. *Metrologia*, 44(6): 484, 2007.

Wiley J Larson and James Richard Wertz. *Space mission analysis and design*. Microcosm: Kluwer Academic Publishers, 1992.

Creon Levit and William Marshall. Improved orbit predictions using two-line elements. *Advances in Space Research*, 47(7):1107–1115, 2011.

David M Lucchesi. Reassessment of the error modelling of non-gravitational perturbations on LAGEOS II and their impact in the Lense–Thirring derivationPart II. *Planetary and Space Science*, 50(10-11):1067–1100, 2002.

G March, EN Doornbos, and PNAM Visser. High-fidelity geometry models for improving the consistency of CHAMP, GRACE, GOCE and Swarm thermospheric density data sets. *Advances in Space Research*, 63(1):213–238, 2019.

Frank Marcos, Shu Lai, Cheryl Huang, Chin Lin, John Retterer, Susan Delay, and Eric Sutton. Towards next level satellite drag modeling. In *AIAA Atmospheric and Space Environments Conference*, page 7840, 2010.

M Menvielle and A Berthelier. The K-derived planetary indices: Description and availability. *Reviews of Geophysics*, 29(3):415–432, 1991.

Oliver Montenbruck and Eberhard Gill. *Satellite orbits: models, methods and applications*. Springer Science & Business Media, 2000. [Figure 3.1].

Oliver Montenbruck and Remco Kroes. In-flight performance analysis of the CHAMP BlackJack GPS receiver. *GPS solutions*, 7(2):74–86, 2003.

Oliver Montenbruck, Ben Nortier, and Sias Mostert. A miniature GPS receiver for precise orbit determination of the Sunsat 2004 micro-satellite. In *Proceedings of the 2004 National Technical Meeting*. Institute of Navigation, 2004.

Oliver Montenbruck, Tom Van Helleputte, Remco Kroes, and Eberhard Gill. Reduced dynamic orbit determination using GPS code and carrier measurements. *Aerospace Science and Technology*, 9(3):261–271, 2005.

Oliver Montenbruck, Gerardo Allende-Alba, Josep Rosello, Michel Tossaint, and Franz Zangerl. Precise Orbit and Baseline Determination for the SAOCOM-CS bistatic radar mission. *Navigation: Journal of The Institute of Navigation*, 65(1):15–24, 2018.

Francesca Panzetta, Mathis Bloßfeld, Eren Erdogan, Sergei Rudenko, Michael Schmidt, and Horst Müller. Towards thermospheric density estimation from SLR observations of LEO satellites: a case study with ANDE-Pollux satellite. *Journal of Geodesy*, 93(3): 353–368, 2019.

Rudy Pastel. Estimating satellite versus debris collision probabilities via the adaptive splitting technique. In *Proceedings of the 3rd International Conference on Computer modeling and simulation, Mumbai, India*, 2011.

DE Pavlis, S Luo, P Dahiroc, JJ McCarthy, and SB Luthcke. GEODYN II system description. *Hughes STX Contractor Report, Greenbelt, Maryland*, 1998.

DE Pavlis, S Poulouse, and JJ McCarthy. GEODYN operations manuals. *Contractor report, SGT Inc., Greenbelt, MD*, 2006.

Gérard Petit and Brian Luzum. IERS conventions (2010). Technical report, BUREAU INTERNATIONAL DES POIDS ET MESURES SEVRES (FRANCE), 2010.

JM Picone, AE Hedin, D Pj Drob, and AC Aikin. NRLMSISE-00 empirical model of the atmosphere: Statistical comparisons and scientific issues. *Journal of Geophysical Research: Space Physics*, 107(A12):SIA–15, 2002.

Marcin D Pilinski, Brian M Argrow, and Scott E Palo. Semiempirical model for satellite energy-accommodation coefficients. *Journal of Spacecraft and Rockets*, 47(6):951, 2010.

Remko Scharroo and Pieter Visser. Precise orbit determination and gravity field improvement for the ERS satellites. *Journal of Geophysical Research: Oceans*, 103(C4): 8113–8127, 1998.

Fabian Schiemenz, Jens Utzmann, and Hakan Kayal. Propagating EUV solar flux uncertainty to atmospheric density uncertainty. *Advances in Space Research*, 63(12): 3936–3952, 2019.

F Seitz, S Kirschner, and D Neubersch. Determination of the Earth's pole tide Love number k2 from observations of polar motion using an adaptive Kalman filter approach. *Journal of Geophysical Research: Solid Earth*, 117(B9), 2012.

A Sengoku, MK Cheng, and BE Schutz. Anisotropic reflection effect on satellite, ajisai. *Journal of Geodesy*, 70(3):140–145, 1995.

Kun Shang, Junyi Guo, CK Shum, Chunli Dai, and Jia Luo. GRACE time-variable gravity field recovery using an improved energy balance approach. *Geophysical Supplements to the Monthly Notices of the Royal Astronomical Society*, 203(3):1773–1786, 2015.

James A Slater and Stephen Malys. WGS 84Past, Present and Future. In *Advances in Positioning and Reference Frames*, pages 1–7. Springer, 1998.

Byron Tapley, Bob Schutz, and George H Born. *Statistical orbit determination*. Elsevier Academic Press, 2004a.

Byron D Tapley, S Bettadpur, M Watkins, and Ch Reigber. The gravity recovery and climate experiment: Mission overview and early results. *Geophysical Research Letters*, 31(9), 2004b.

David A Vallado. *Fundamentals of astrodynamics and applications*, volume 12. Springer Science & Business Media, 2001.

David A Vallado and Paul Crawford. SGP4 orbit determination. In *Proceedings of AIAA/AAS Astrodynamics Specialist Conference and Exhibit*, pages 18–21. AIAA Reston, VA, 2008.

D Vrancken, D Gerrits, K Mellab, and S Santandrea. PROBA-V: A Multi-Spectral Earth observation mission based on a PROBA platform–status update. In *Small Satellite Systems and Services–The 4S Symposium, Portorož, Slovenia, June*, pages 4–8, 2012.

Karel F Wakker. Fundamentals of astrodynamics. *Institutional Repository Library, Delft University of Technology, Delft, The Netherlands*, 2015.

James Richard Wertz. *Mission geometry: orbit and constellation design and management: spacecraft orbit and attitude systems*. Microcosm: Kluwer Academic Publishers, 2001.